# Site U1348[1]

Expedition 324 Scientists[2]

## Chapter contents

Background and objectives . . . . . 1
Operations . . . . . 3
Sedimentology . . . . . 3
Paleontology . . . . . 9
Igneous petrology . . . . . 11
Alteration and metamorphic petrology . . . . . 16
Structural geology . . . . . 17
Geochemistry . . . . . 18
Physical properties . . . . . 19
Paleomagnetism . . . . . 21
Downhole logging . . . . . 21
References . . . . . 25
Figures . . . . . 29
Tables . . . . . 88

# Background and objectives

## Background

Integrated Ocean Drilling Program Site U1348 (proposed Site SRSH-6) was the third site completed during Expedition 324. It was planned as the northernmost of three sites to be drilled on Tamu Massif (Fig. F1). Like other holes planned for Expedition 324, the main goal for the site was to core lava flows, so the fact that Site U1348 produced mainly sedimentary and volcaniclastic rocks came as a surprise.

As outlined in other chapters (see the "Expedition 324 summary" and "Site U1347" chapters), Tamu Massif is the largest volcanic edifice within Shatsky Rise, and it is thought to represent the initial eruptions, perhaps caused by a plume head (Sager et al., 1999). The location for Site U1348, on the north flank of Tamu Massif, was chosen with hopes of establishing a transect of ages across this large edifice and documenting geochemical variations within this feature. The site is located near an anomaly between M18 and M19 (Nakanishi et al., 1999), implying a basement age of 144–145 Ma (Ogg et al., 2008). Even though Site U1348 is located ~400 km farther north than Ocean Drilling Program (ODP) Leg 198 Site 1213 (Fig. F1 in the "Expedition 324 summary" chapter), the age estimate for Site U1348 is nearly the same as the radiometric date measured for Site 1213 igneous rock (144.6 ± 0.8 Ma) (Mahoney et al., 2005; Shipboard Scientific Party, 2002b). Thus, results from Site U1348 were to help determine the magnitude of the age difference between the north and south flanks of Tamu Massif as well as whether its formation was as rapid as proposed (e.g., Sager and Han, 1993; Sager, 2005).

In addition, the tectonic setting of Site U1348 was recognized as very different from other Tamu Massif sites. Whereas Sites 1213 and U1347 are located on the eastern and southern flanks of the massif, where the igneous basement appears to be normal volcanic slope, Site U1348 is located on the north flank, where magnetic lineations and bathymetry imply that spreading ridge–related rifting occurred (Sager et al., 1999; Nakanishi et al., 1999). Moreover, Site U1348 is located south of "Helios Basin," a rectangular basin between Tamu and Ori massifs (see Sager et al., 1999; Fig. F2 in the "Expedition 324 summary" chapter) that is thought to have formed by a short period of rifting and was preserved as a failed rift by a jump of the Pacific-Izanagi ridge farther northeast (Nakanishi et al., 1999). The magnetic lineations that traverse the

[1] Expedition 324 Scientists, 2010. Site U1348. *In* Sager, W.W., Sano, T., Geldmacher, J., and the Expedition 324 Scientists, *Proc. IODP,* 324: Tokyo (Integrated Ocean Drilling Program Management International, Inc.). doi:10.2204/iodp.proc.324.105.2010
[2] Expedition 324 Scientists' addresses.


doi:10.2204/iodp.proc.324.105.2010

northern flank of Tamu Massif bend into Helios Basin. Furthermore, the bathymetry of northern Tamu Massif consists of chevron-shaped ridges and troughs, interpreted to be related to seafloor spreading and associated rifting (Sager et al., 1999; Nakanishi et al., 1999). Thus, the igneous rock cored at Site U1348 was predicted to be significantly different from that of the rest of Tamu Massif.

Site U1348 is located near the peak of a basement high on site survey seismic Line 13 from Cruise TN037 (Fig. F2). The top of this high was picked for drilling because sediments are thick in the surrounding area and the top of the buried hill is the only shallow basement in the area. Furthermore, there is only one site survey seismic line on northern Tamu Massif, providing few other choices. Although there was concern that drilling on a basement high might recover volcaniclastics rather than lava flows, the basement high at Site U1348 is large (>30 km wide). Therefore, this structure was assumed to be too large for a volcaniclastic cone. At the site, acoustic basement is a relatively strong reflecting horizon beneath which there is little or no coherent return of seismic energy. This is, in part, a result of the small single air gun source used for this seismic line, which gave little penetration into the top of the volcano under the sediments, and the relatively fast survey speed, which also helped to limit the signal to noise ratio (see Klaus and Sager, 2002). As can be seen upon closer examination (Fig. F3), sediments from the north onlap against the buried hill's northern flank and only Cenozoic ooze, Late Cretaceous chalk, and chert were expected in the sediment column at the site. Although that portion of the seismic interpretation was correct, acoustic basement turned out to be the top of volcaniclastic material at Site U1348, not lava flows as encountered at Sites U1346 and U1347.

## Scientific objectives

Sampling the Tamu Massif was an important objective because this volcano is the main edifice within Shatsky Rise and Site U1348 was part of a transect along the axis of the massif. As with most Expedition 324 sites, the operational goal for the site was to drill through the sediment overburden, core the oldest sediment overlying igneous basement, and core as deeply into the igneous formation as possible during the time allowed. Although initial objectives focused mainly on understanding the volcanic succession, geochemistry, and radiometric dating, those objectives are now in a state of flux because of the nature of the recovered material. It is presumed that the original objectives remain valid, in as much as they can be satisfied by the recovered cores, but the objectives will change as the science party studies the complex cored section. It appears that the cores may contain considerable information about sedimentation, paleodepth, and paleoenvironment, so those objectives may rise to greater importance.

The initial scientific objectives of coring at Site U1348 are similar to those at other sites (see the "Expedition 324 summary" chapter). Coring of igneous rock was planned to determine the age of igneous basement so that the age progression and duration of volcanism at Tamu Massif can be constrained. A critical objective at Site U1348, and indeed all Expedition 324 sites, was to core enough igneous rock of suitable freshness and composition to establish at least one reliable radiometric date. Igneous rocks were also critical to geochemical and isotopic studies with the goals of establishing the elemental compositions of the rocks, variations in compositions, and isotopic characteristics. Such data are crucial for determining the source of magma, inferring its temperature and depth of melting and crystallization, and deducing the degree of partial melting, as well as tracking its evolution with time. Because the Site U1348 cores appear to contain volcaniclastic material that is highly altered, an important objective will be to examine the metamorphosis of the cored material to help understand not only the initial composition but the processes that have changed the rock over time.

Expedition 324 also sought to constrain the evolution of Shatsky Rise by collecting samples for several nongeochemical studies focusing on varied aspects of rise geology. For Site U1348, it appears that sedimentary and paleontological studies will be particularly important because the cores recovered sedimentary material with apparent paleoenvironmental and paleodepth implications. Thus, deciphering the ages of the sediments and their paleoenvironment through studies of biostratigraphy, fossil content, and sedimentary structures will be an important task. In addition, physical volcanologists, structural geologists, and logging geophysicists will use cores and logs to infer the eruption style, igneous products, and physical structure of the cored section.

Paleomagnetic study of the samples recovered at Site U1348 will seek to determine the magnetic polarity of basement for comparison with surrounding magnetic lineations and the geomagnetic polarity timescale as well as the paleolatitude of the rise and its plate tectonic drift. Physical properties of Shatsky Rise core samples will be measured to better understand the nature of the rocks that make up the sedimentary section and to constrain fundamental physical properties that affect geophysical imaging and remote sensing. Such data will be useful for constraining seismic and gravity studies in particular.

# Operations

Times in this chapter are given in local ship time. During transit to Site U1346, shipboard clocks were advanced 1 h, resetting local ship time to Sydney Standard Time (Universal Time Coordinated + 10). No further adjustments to the clock were made during the expedition.

Seafloor at Site U1348 was tagged at 3275.0 m drilling depth below rig floor (DRF) (Table **T1;** 2.7 m shallower than the corrected precision depth recorder depth of 3277.7 m DRF), and Hole U1348A was spudded at 1245 h on 3 October 2009. The hole was washed ahead with a wash barrel in place to 84.2 m drilling depth below seafloor (DSF) where rotary coring was initiated. Coring proceeded from 84.2 to 189.9 m DSF (105.7 m) with a poor average recovery of 3.5%, due mostly to the prevalence of soft pelagic ooze and chert. Once past this depth and starting with Core 324-U1348A-13R, recovery improved markedly as the sediment transitioned to more solid sandstone and then to volcaniclastics. The bottom 134.2 m of the hole was cored at an average rate of penetration (ROP) of 8.9 m/h with an average recovery of 57.5%. The average recovery for the 239.9 m cored interval was 33.7%. The washed interval was 84.2 m. This hole was terminated at 324.1 m DSF subsequent to a science meeting during which it was collectively decided to stop further drilling at this site because igneous basement was apparently not within reach (see Fig. **F4** for overview).

The hole was prepared for logging operations with a wiper trip and displacement with 86 bbl of heavy mud (10.5 ppg). Following the release of the bit at the bottom of the hole, the drill string was pulled back and the end of pipe placed at 97.6 m DSF. At 2030 h on 5 October, the Schlumberger equipment was rigged up and the first tool string (triple combination [triple combo]) was successfully deployed to ~322 m DSF. Once the triple combo was recovered, the second logging suite (Formation MicroScanner [FMS]-sonic) was made up and deployed at 0700 h on 6 October. This tool was also able to reach within 2 m of the bottom of the hole. As the tool was being drawn back into the drill string, it became firmly stuck in the bottom-hole assembly (BHA) with the calipers at the level of the top connector of the mechanical bit release. For 1.5 h, the logging winch operator attempted to advance the tool with no success (see **"Downhole logging"**).

The only option remaining was to use the Kinley crimper and cutter system to recover the recalcitrant instrument. The Kinley crimper was deployed on the logging line, followed 45 min later by the hammer which triggered the crimper charge. A positive indication of the firing of the crimper was indicated by the expected loss of signal voltage from the logging tool. The next step was the deployment of the cutter tool and hammer, which went as planned and neatly severed the logging line just above the cable head of the tool suite. The severed end of the logging line was recovered at 2030 h, after which the drill string was retrieved. When the BHA was at the surface, the FMS-sonic tool was still firmly pinned by the caliper arms inside the top connector of the mechanical bit release.

Once the FMS-sonic was rigged down, the drilling equipment was secured and the beacon recovered. The vessel departed for the next site at 0845 h on 7 October.

# Sedimentology

One hole was drilled at Site U1348 on the northern flank of Tamu Massif, Shatsky Rise, in a water depth of 3264 meters below sea level (mbsl). A thick sequence (~120 m stratigraphically) of volcaniclastic sediments topped with shallow-water calcareous sandstones, greenish clays, nannofossil ooze, and chert was recovered. Despite drilling to nearly 325 meters below seafloor (mbsf), basaltic basement was not reached at Site U1348, and a unique sequence of marine volcaniclastic rocks was recovered in Cores 324-U1348A-14R through 26R. The uppermost cores contained red chert interbedded with a remarkably well preserved section of Cenozoic/Late Cretaceous nannofossil ooze >1 m long. Yellow brecciated cherts were also recovered stratigraphically below the red cherts and above highly silicified altered sandstones. Below this, a sequence of shallow-water bioclastic sandstones with volcanic clasts was found. This sequence includes an interval of bright green zeolitic clays. Highly altered volcaniclastic sequences comprise most of the lowermost 120 m of the hole. Based on the marine fossil content and bedding structures, these sequences are interpreted to represent a mixture of in situ and redeposited volcanic materials erupted in a submarine environment.

## Unit descriptions

The lithostratigraphy of Site U1348 is shown in Figure **F5.**

- Unit I: cherts, chalks, and nannofossil ooze (84.2–161.1 mbsf).
- Unit II: sandstones and clays (161.1–199.5 mbsf). This unit is predominantly bioclastic sandstones with volcaniclastics cemented by calcite, quartz, or silica. The sequence is altered and becomes more zeolitic downhole, including a ~60 cm interval composed almost entirely of zeolites.

- Unit III: layered granular hyaloclastite (199.5–242.0 mbsf). This unit is divided into three subunits based on degree and style of bedding and the relative proportion of bioclastic components present.
- Subunit IIIa: altered granular hyaloclastite (199.5–203.5 mbsf).
- Subunit IIIb: calcite-cemented volcaniclastic sandstone (203.5–209.0 mbsf).
- Subunit IIIc: altered granular hyaloclastite to fine hyaloclastite (209.0–242.0 mbsf).
- Unit IV: volcaniclastic sandstone with fossils (242.0–262.8 mbsf).
- Unit V: layered granular hyaloclastite (262.8–287.0 mbsf).
- Unit VI: structureless vesicular hyaloclastite breccia (below 287 mbsf).

## Unit I

Interval: 324-U1348A-1W through 10R-1, 21.5 cm
Depth: 84.2–161.1 mbsf

Cores 324-U1348A-1W through 9R contain a mixture of red cherts, calcareous nannofossil ooze, and yellow brecciated chert beds. The recovered material from this unit is predominantly composed of small red chert pieces with patches of porcellanite and thin foraminifer-bearing chalk coatings. The chert samples vary from dark brownish red to pinkish red with pale patches and streaks of pinkish cream porcellanite. Dendritic, opaque mineral growths (possibly manganese oxide) are associated with these cherts. The growths are concentrated along siliceous veins but can also be found within the reddish siliceous matrix (Fig. F6). A well-preserved, partially laminated section of light-colored nannofossil ooze was recovered in Section 324-U1348A-2R-1 (Fig. F7). The ooze is pale yellow in color, soupy, and composed almost entirely of calcareous nannofossils with the exception of a 6 cm section of pale gray ooze at the top of Section 324-U1348A-2R-1. Although still soft, the gray ooze is slightly more consolidated and contains up to 5% radiolarians, diatoms, and silicoflagellates. The gray ooze and cherts in Core 324-U1348A-1W, stratigraphically above, are mid-Cenozoic in age, whereas the pale yellow ooze below is Late Cretaceous (Santonian–Campanian) in age (see "Paleontology"). The gray ooze and contents of the wash core could simply reflect drilling-related "fall-in" or may represent a genuine hiatus in deposition between the Late Cretaceous and mid-Cenozoic. In Core 324-U1348A-9R, the cherts become bright yellow. Some pieces can be termed "jasper," as they are opaque and display complex vein networks and silica-cemented brecciation (Fig. F8). Another interval of white to pale yellow nannofossil ooze is present in Section 324-U1348A-10R-1 between 0 and 21.5 cm. Both planktonic and benthic foraminifers are present in this ooze (see "Paleontology"). A few pieces of red chert are mixed in with the ooze at the top of this interval, and most of the sediment is intensely disturbed by drilling. A few cross-bedded horizons are visible in interval 324-U1348A-10R-1, 14–17 cm, and consist of thin lenses of coarse brownish green sand within the nannofossil ooze matrix.

## Unit II

Interval: 324-U1348A-10R-1, 21.5 cm, through 13R
Depth: 161.1–199.5 mbsf

Below the chert-ooze sequence is a thick succession of sandstones with a few beds of zeolite or clays extending ~40 m stratigraphically. Unit II extends from interval 324-U1348A-10R-1, 21.5 cm, to the base of Core 13R. Core 10R is predominantly altered, quartz-cemented, dark yellow sandstone with light gray streaks of chert and a few altered volcanic clasts. Across interval 324-U1348A-10R-1, 48–50 cm, the original sandstone has been broken into ~1 cm sized pieces and recemented with white/clear chert, creating a silica-sandstone breccia, which was recovered as one biscuited piece (Fig. F9). Fractures are common in Core 10R, as are small cavities (vugs) filled with quartz crystals ~1 mm in size. Recovery in Core 11R was especially poor. Only 9 cm of coarse, loosely calcite-cemented bioclastic sandstone, preserved as four small nuggets (biscuited by drilling), was recovered. These sandstones are bright yellow in color and moderately to well sorted with subrounded grains. The majority of the grains are tubular coral fragments <2 mm long, with additional bioclastic material including bryozoan and shell fragments (Fig. F10). Small pyrite clusters also make up a minor component of the sandstone. Beneath the yellow sandstone biscuits, a sequence of poorly lithified brownish orange sandstone is interbedded with two soft layers of greenish yellow and olive-green clays (Fig. F11). The sandstone is calcite cemented, crumbly, and contains subrounded quartz crystals and biogenic fragments as well as a few opaque mineral grains. The first clay layer is pale greenish yellow and spans ~20 cm of Section 324-U1348A-12R-1 (13.5–33 cm). Within the clay layer is a thin (~1 cm) hard, white, silty band composed of small needlelike grains. The second soft clay layer, in interval 324-U1348A-12R-CC, 4–12 cm, is greener in color and of similar texture but grades into yellow siltier material toward its base (11–12 cm). X-ray diffraction (XRD) analysis reveals the clay layers are composed of different minerals. The lighter yellow-green layer is

mainly composed of zeolite, whereas the greener clay is predominantly composed of celadonite (see "Alteration and metamorphic petrology"). This interval also corresponds to a spike in potassium, as seen in the natural gamma ray (NGR) data (see "Downhole logging"). The high potassium content is also confirmed by inductively coupled plasma–atomic emission spectroscopy (ICP-AES) analysis of the green clays (see "Geochemistry"). The base of Core 324-U1348A-12R is soft pale yellow silt and clay. Stratigraphically below, in Core 13R, is a light yellow-brown carbonate-cemented coarse to very coarse sandstone with abundant bioclasts and altered volcaniclastics. The bioclastic materials include bivalve shells (some as large as ~2–3 cm), crinoid ossicles, and fragments of echinoderm plates (Fig. F12). The altered volcanic clasts are larger, granule or pebble sized, and most are pale green in color and vesicular, although a few darker, less altered basaltic clasts are present. Interval 324-U1348A-13R-1, 0–135 cm, is structureless and unbedded. Two small lenses of darker red-brown material are present at 125–126.5 cm, indicating erosive scouring. A 2 cm interval of brownish orange clay is present beneath the coarse sandstone. This layer is soft, containing tiny brownish shards of altered vitric glass, iron oxides, and calcite, and sits atop finely laminated fine- to medium-grained sandstone. The sandy grains are angular with a volcanic ash and clay component. Within this sandstone, orange-red, strong brown, and grayish green color banding seems to track slight lithologic changes in grain size. The greener layers appear to be more clay rich. Smear slides reveal that the volcanic component is primarily fibrous isotropic zeolite and altered glass with iron oxides and occasional feldspar laths.

## Unit III

Interval: 324-U1348A-14R through 18R
Depth: 199.5–242.0 mbsf

### *Subunit IIIa*

This subunit is mainly composed of granular hyaloclastites. The hyaloclasts are dark colored, subangular to very angular in shape, and scattered within a finer grained matrix (Fig. F13). Most of the hyaloclasts are coarse sand to lapilli sized and can be divided into two types: dark angular clasts and dark to light gray vesicle-rich grains. The angular clasts are probably highly altered aphyric basalts. One large angular clast, 3 cm long, spans interval 324-U1348A-14R-3, 57–60 cm (Fig. F13A). The vesicle-rich clasts could be spherules of altered hyaloclastics (see "Petrology and igneous petrology"). The matrix materials are finer hyaloclasts cemented by calcite. This unit is mainly structureless and poorly sorted, but interval 324-U1348A-14R-1, 24–57 cm, is slightly laminated in places.

### *Subunit IIIb*

The top of Subunit IIIb spans interval 324-U1348A-14R-CC, 4 cm, to 15R-1, 7 cm, and comprises cream to light gray calcite-cemented sandstone (Fig. F13B). Weak calcite-rich horizontal bands are found within the subunit. Coarse, rounded volcaniclastics are scattered throughout but are concentrated into horizontal bands. One large bivalve shell is present in Section 324-U1348A-14R-CC. Although a dark reddish brown chert pebble is present at the top of Section 15R-1, it is interpreted as fall-in from the upper part of the hole and is unlikely to be in situ.

### *Subunit IIIc*

This subunit is mostly dark greenish gray poorly sorted granular hyaloclastite, hyaloclastite sandstone, and fine hyaloclastite (Figs. F14, F15). Grading is found in some parts of the subunit. Some beds are normally graded, but reverse grading is more common (Fig. F15). Beds are horizontally laminated in the upper section of this subunit (Sections 324-U1348A-15R-1 through 15R-4, 16R-1, and 17R-3 through 17R-5) and slightly inclined in the lower part of the subunit (Sections 18R-1 through 18R-2). The dominant sedimentary facies of Subunit IIIc is structureless, but in places successions of fine- to medium-bedded granular hyaloclastites, hyaloclastite sandstones, and fine hyaloclasts are present (Fig. F16). The structureless and bedded parts generally show a layered repetitive structure. Large, dark clasts (>0.5 cm) with subangular to very angular shape are concentrated into some intervals (e.g., interval 324-U1348A-17R-5, 30–33 cm; Fig. F15B). At these intervals, sediments often show clast-supported structure. Among the clasts, large (>1 cm), dark gray vesicular basalts are present.

## Unit IV

Interval: 324-U1348A-18R-CC through 20R-4
Depth: 242.0–262.8 mbsf

Unit IV is composed of bioclastic sandstone and volcaniclastic sediments cemented by gray to light gray calcite and zeolite. The upper sections of the unit (interval 324-U1348A-18R-CC, 0 cm, to 19R-2, 39 cm) are structureless and dominated by volcaniclastics. Gray to dark gray volcanic clasts are scattered throughout the unit. Most clasts are subangular to subrounded, but some are rounded. Some bedding is present in places, although clasts within these beds are generally poorly sorted. Unit IV is characterized by a concentration of biogenic materials such as

shell fragments, crinoid ossicles, gastropods, and a large ammonite (Fig. F17). In addition, glauconite and small, dark biogenic clasts are found throughout Sections 324-U1348A-18R-CC and 19R-1. Bioturbation structures, such as infilled burrows, are common throughout this unit. The lower part of the unit (interval 324-U1348A-19R-2, 39 cm, through 20R-4, 150 cm) is mainly composed of a succession of thin- to medium-bedded volcaniclastic silt to coarse sands and coarse volcaniclastic sandstones. Reddish scoria clasts are present throughout the unit (Fig. F18). The base of the unit is placed at the bottom of an interbedded silty sand and medium sandstone section.

### Unit V

Interval: 324-U1348A-20R-5 through 23R-1, 108 cm
Depth: 262.8–287.0 mbsf

Unit V consists of fine to granular hyaloclastites. The upper half of the unit (interval 324-U1348A-20R-5, 0 cm, through 22R-1, 36 cm) is generally structureless but does show weak normal and reverse grading in places. Within the graded beds sediments are clast supported but are matrix supported in the structureless intervals. Large volcanic clasts (>5 mm) are present throughout Unit V. The clasts are classified into three types:

1. Dark to light gray vesicular hyaloclasts generally larger than 1 cm,
2. Dark gray basaltic fragments generally smaller than 1 cm, and
3. Light gray to light greenish gray altered basaltic fragments generally <1 cm in size.

The matrix, mainly composed of altered sand-sized hyaloclasts and fine hyaloclastite, is dark greenish gray in the top part of the unit (Sections 324-1348A-20R-5 through 20R-6) and dark gray in the remainder of the upper portion of the unit.

The lower half of Unit V (interval 324-U1348A-22R-1, 35 cm, through 23R-1, 108 cm) is characterized by well-defined bedding, where inclined layers are common (Fig. F19). Dips of the inclined layers are generally ~20° (Fig. F19). The dip angle gradually increases with increasing depth, especially when compared to the subhorizontal laminations seen in Unit III (see **"Structural geology"**). Downhole logging data (FMS) suggest that the dip of the inclined layers is predominantly toward the southeast throughout the lower half of Unit V (see **"Downhole logging"**). The interval includes hyaloclastite breccia and granular hyaloclastite containing vesicular hyaloclasts. The inclined layers exhibit normal grading within strata containing predominantly dense hyaloclasts and reverse grading within strata composed principally of vesicular hyaloclasts. Another noteworthy feature of the lower half of Unit V is the presence of bioturbation in some intervals.

### Unit VI

Interval: 324-U1348A-23R through 26R
Depth: 287.0–324.1 mbsf

Unit VI is predominantly composed of dark gray hyaloclasts, many of which are heavily altered. This unit is almost exclusively clast supported and generally structureless (Fig. F20), though a few intervals contain interbedded finer materials (e.g., interval 324-U1348A-26R-1, 55–78 cm). The finer materials are composed of siltstones, sandstones, and altered vesicular hyaloclasts and are often faintly laminated. The upper portion of Unit VI shows slightly chaotic and churned features probably associated with bioturbation, but the degree of bioturbation decreases toward the middle and lower portions of the unit and is entirely absent in some sections. A small amount of fresh volcanic glass is preserved within this unit (see **"Igneous petrology"**).

## Interpretation

A strong volcanogenic influence at Site U1348 is evidenced by Units II–VI. In addition, many of the beds show evidence of alteration, which changed both the composition and textures seen in the cores at this site. In contrast, Unit I, which is composed of cherts, chalks, and oozes, appears devoid of volcanogenic components and was probably deposited in a pelagic environment. The calcareous sandstones in Unit II contain abundant remains of epifaunal and reef-building fauna, indicative of a shallow-water marine environment. The persistent volcaniclastic component (including palagonite and vesicular hyaloclasts) in Unit II indicates a volcanic source proximal to the area of carbonate deposition. The green clays in Core 324-U1348A-12R may represent a sequence of volcanic ashes, subsequently altered to zeolites and celadonite in the marine environment. The rocks in Units III–VI are almost entirely volcanogenic and are predominantly composed of various sized altered glass fragments. The depositional setting for these units is probably submarine, but modes of deposition may range from compacted primary hyaloclastite to redeposition of the volcanic material by turbidites.

### Unit I

Some of the cherts in Unit I contain remnant bedding features preserved as porcellanite patches and streaks within the secondary silica matrix. High concentrations of foraminifers within some chert and

porcellanite pieces indicate these rocks represent calcareous oozes subsequently silicified by remobilized silica. The silica was likely sourced from dissolved radiolarian tests. Reddish brown cherts dominate here and differ from the black cherts recovered from Sites U1346 and U1347. Cherts can be a variety of colors, including black/gray, brown, red, blue, green, and yellow. The specific color, however, is often related to factors such as

1. The redox conditions at the time of deposition,
2. The percentage of silica relative to contaminants in the chert,
3. The chemical composition of the contaminants, and
4. Any subsequent alteration processes.

Red cherts are usually enriched in oxidized iron–bearing minerals such as hematite and thus are indicative of oxic bottom water conditions. The color of cherts at Shatsky Rise has previously been related to changes in sedimentation rate (Fontilea et al., 2006), where redder cherts are associated with lower sedimentation rates. This relationship may also be applicable to the Unit I cherts at Site U1348.

The yellow color of the chert recovered in Core 324-U1348A-9R, its opacity, and the evidence for brecciation and recementation are consistent with low-temperature hydrothermal alteration. The pervasive yellow color is likely to be derived from the presence of goethite (iron oxyhydroxide), which is often associated with hydrothermal systems. The alteration seen in the underlying units also suggests circulation of warm fluids through the sediments after deposition. As the cherts and chalks were likely deposited long after the main active phase of volcanism on Tamu Massif, the source and mechanism of this hydrothermal alteration remain enigmatic.

Although very few soft sediments were recovered in Unit I, the cherts are presumably interbedded with calcareous nannofossil ooze in the upper part of the sequence, as suggested by the material recovered in Core 324-U1348A-2R, and with more lithified chalk and porcellanite in the lower part, as suggested by material recovered in Cores 3R through 9R. The recovered oozes are almost exclusively composed of pelagic constituents, mostly calcareous nannofossils and occasional siliceous components. This suggests a relatively deep water setting far removed from a terrestrial source. In this sense, Unit I at Site U1348 is similar to Unit I at both Sites U1346 and U1347 and probably represents deposition after Tamu Massif had subsided out of the photic zone.

### Unit II

Unit II sandstones are primarily composed of biogenic components such as echinoderm, coral, bivalve, and bryozoan fragments, with varying proportions of volcaniclastics. The percentage of volcanic constituents and the amount of zeolite in the cores increase toward the bottom of this unit. The uppermost sandstones in Core 324-U1348A-10R are bright yellow and composed of quartz-cemented, iron oxide–stained grains. The cementation, degree of oxidation, and proximity of the yellow cherts in Core 9R stratigraphically above suggest this part of the sequence may have been subjected to low-temperature alteration after deposition.

Interestingly, the coarse biogenic sandstones in Core 324-U1348A-11R are primarily composed of rounded coral fragments and bryozoans, suggestive of a stable, warm, very shallow marine environment. The degree of sorting seen in the rocks from this core and the rounded nature of the grains further supports a very shallow environment where wave action could move and rework the sediment. This unit also contains greenish rounded vesicular volcaniclastic grains, providing evidence for a proximal source of weathered volcanic material if not direct evidence for contemporaneous volcanic activity nearby. These rocks do not seem to have been altered to the same degree as the overlying strata in Core 10R, although this may be due to the different primary constituents in the two cores responding differently to the alteration.

The greenish yellow clays in Core 324-U1348A-12R most likely represent altered ash deposits. The angular nature of the grains suggests volcanic glass was the primary constituent, which has subsequently been altered to a mixture of zeolites or celadonite. The presence of remaining detrital feldspars and the high potassium content of these rocks support this interpretation. However, the geochemistry of these clays, as deduced from ICP-AES analysis, is not consistent with basaltic source material and more closely resembles the alteration products of continental or arc volcanism (see **"Geochemistry"**), thus suggesting the source of this ash may have been from a relatively proximal, hitherto undescribed, island arc source.

Biogenic sandstones in Core 324-U1348A-13R are dominated by echinoderm fragments, with a strong volcanogenic component. The amount of palagonite (an alteration product of volcanic glass) throughout the core is consistent with a prolonged input of volcaniclastic material coeval with shallow-water carbonate deposition. The reddish orange to yellow or

greenish laminated sand and siltstones at the base of Core 13R are carbonate cemented, highly altered, and contain many compacted angular clasts. The dominance of zeolites with occasional altered plagioclase laths suggests the primary sediment was fine-grained volcaniclastics. The depositional environment was likely to have been a fairly shallow marine environment with a large detrital or primary source of volcanic glass. However, the sediments are undisturbed (unbioturbated), indicating fairly rapid sedimentation.

### Units III–VI

The Cretaceous volcaniclastic beds (Units III–VI) at Site U1348 preserve a record of nearby submarine volcanism. Microscopic characteristics of the clasts in Units III–VI that support a dominantly hydroclastic source are presented in **"Igneous petrology."** Unit VI in particular is almost completely composed of altered hyaloclasts. Hyaloclastite was defined for rocks composed of glass produced by nonexplosive spalling and granulation of pillow rinds by Rittman (1962). However, the term has been expanded to all vitroclastic (i.e., glassy) tephra produced by the interaction of water and hot magma or lava (Fisher and Schmincke, 1984). Dominant hyaloclastites suggest primary hydroclastic deposition.

Units III and V are mainly composed of poorly sorted granular hyaloclastite and alternating layers of granular hyaloclastite to fine hyaloclastite. The alternating layers are often laminated and graded. These are considered to represent deposition by low-density turbidites (Bouma, 1962). Units III–VI are interpreted to have been deposited in submarine environments.

Unit III probably represents two mass flows (Subunits IIIa and IIIc) divided by sediments deposited during a quiescent period (Subunit IIIb). The sedimentary features are divided into two characteristic facies: thick clast-rich sequences and cyclic fine to coarse tuff sequences (interbedded in the thick clast-rich sequence).

The thick clast-rich sequences are mostly poorly sorted and can be structureless or exhibit graded bedding (both normal and reverse) (Figs. **F13, F14**). Their thickness attains a maximum of ~10 m. Clasts are mainly composed of angular vesicular hyaloclasts (often altered and white) and angular to subangular basaltic lithic clasts. The matrix is mainly altered vitric clasts and vesicular fragments. The lower part is often reverse graded, whereas the upper part often displays normal grading. We consider this interval to represent mass flow deposits, which are divided in terms of their position in the Lowe sequence (Lowe, 1982). The reverse graded part is considered to represent the R2 division (traction carpet) of the Lowe sequence, whereas the normally graded part is considered to represent the R3 division (Lowe, 1982) (Fig. **F21**). Such evidence suggests that these thick clast-rich sequences were deposited by high-density turbidity currents (Fig. **F22**). The grains are mostly primary volcaniclastics, and some thick clast-rich sequences can be interpreted as subaqueous pyroclastic flow deposits (e.g., Fiske, 1963; Fiske and Matsuda, 1964; Gibson et al., 2000) and/or hyalotuff (e.g., Honnorez and Kirst, 1975; Heiken and Wohletz, 1985; Yamagishi, 1987; Busby, et al. 2006).

Unit IV represents a quiescent period of volcanism. The concentration of biogenic materials and glauconite suggest deposition in neritic environments. The lower part of Unit IV is characterized by fine-grained sediments and abundant bioturbation, which suggest a lower rate of volcaniclastic deposition (Fig. **F22**). The red color of some scoria within this unit indicates oxidation in subaerial environments.

The sedimentary features of Unit V are inclined layers and foreset beds (Fig. **F19**), mainly composed of parallel stratified volcanic sandstone with lapilli (altered vitric and lithic clasts). Graded bedding (normal and reverse) and laminations are present throughout. Clast-supported basaltic and/or low-vesicular clasts are concentrated in layers. These deposits are considered to represent turbidites and grain flows (Bouma, 1962; Lowe 1979, 1982; Stow, 1986). The inclined layers may have been deposited as part of the "slope apron" of a volcano. The gradual increase of dip with increasing depth in the core implies decreasing slope angle through time, possibly related to the progradation of the slope apron (Fig. **F22**).

Unit VI is composed of structureless altered hyaloclasts, mainly clast supported, and generally does not contain fine-grained sediments. Some armored clasts are found in this unit. This facies association indicates rapid primary deposition. Most of the sedimentary features in Unit VI are consistent with a model in which materials were derived from primary deposits near the vent and then deposited on the flanks of the volcano. However, there is little evidence of gravity flow deposits (e.g., subaqueous pyroclastic flows, turbidites, subaqueous grain flows, and debris flows). The materials are not stratified (laminated), graded, or matrix supported. Therefore, it is likely that the materials represent in situ hyaloclastite and/or autobreccia. The presence of one interbedded fine-grained interval (interpreted as turbiditic) and the absence of shallow marine sedimentary structures (e.g., wave ripples) indicate deposition in submarine environments at depths below wave base (Fig. **F22**).

# Paleontology

Sediments from Site U1348 (Cores 324-U1348A-1W through 10R) are pelagic in origin and dominated by chert-rich lithologies (stratigraphic Unit I; see **"Sedimentology"**). Their uniqueness is highlighted by two intervals of undisrupted nannofossil oozes recovered in Cores 2R and 10R (140 and 22 cm thick, respectively) that yielded well-preserved, abundant foraminifers. Cherts from Cores 3R through 9R are characterized by loosely attached pinkish oozes or chalks, which are also generally suited for separation of foraminifers with the absence of radiolarians. Sandy to clayey sediments underneath Core 10R (Unit II) are barren of calcareous microfossils.

The initially high abundance, diversity, and preservation state of calcareous nannofossils in Unit I (upper part) progressively decrease with increasing burial depth. Foraminifer abundance and diversity are high in the two narrow ooze intervals (see above) with good preservation. The other examined levels also show relatively high foraminifer abundance throughout, despite limitation of the available material. Both calcareous microfossil groups give ages of mid- to Late Cretaceous for Unit I (except for Cores 324-U1348A-1W and 2R [topmost <8 cm]; see below). In particular, a series of short-lived bioevents that are correlative with standard biochronology are recorded by planktonic foraminifers, ranging in age from the early Aptian to early Campanian (120–80 Ma). Taking account of generally poor preservation of calcareous nannofossils, the age model for this site depends solely on planktonic foraminifers (Fig. **F23**). Benthic foraminifers show changes in abundance and diversity upsection that can be interpreted in terms of the subsidence history of Tamu Massif from the upper to lower bathyal depth.

In light of planktonic foraminifer biochronology as well as calcareous nannofossil ages (Subzone NC7a–Zone CC16), the numerical age of Unit I is determined as ~120–80 Ma. The underlying Unit II and the basement section further below at Site U1348 are dated at older than 120 Ma.

It is noteworthy that the gray ooze loosely inserted in the topmost part of Core 324-U1348A-2R is rich in Cenozoic calcareous and siliceous microfossils. In addition to several species of the calcareous nannofossil genus *Discoaster* (Zones NN6–NN10; Miocene) (Shipboard Scientific Party, 2002a) and a poorly preserved globorotalid species of planktonic foraminifer (Zones N21–N22; Pliocene–Pleistocene) (Shipboard Scientific Party, 2002a), Cenozoic representatives of radiolarians, diatoms, and silicoflagelates are found, including the age-diagnostic silicoflagellate taxon *Dictyocha pulchella* (base of the *Naviculopsis ponticula* Zone to the middle of the *Dictyocha fibula* Zone; middle–late Miocene) (Bukry, 1981). Because the gray Cenozoic ooze is disrupted and shows an irregular and mixed contact with the pale yellow Campanian ooze, it is uncertain if the Cenozoic portion unconformably overlies the Cretaceous or is an artifact induced by the rotary core barrel (RCB) drilling disturbance. In any case, it is likely that Cenozoic sediments are present in the proximity of Core 324-U1348A-2R, and the estimated range of hiatus(?) is ~60 m.y. (Campanian to Miocene).

## Calcareous nannofossils

Calcareous nannofossils in the sediments of Site U1348 are good to moderately preserved and occur in frequent abundance in Cores 324-U1348A-1W and 2R (ooze at the top of stratigraphic Unit I). Downhole, their preservation declines to moderate to poor, and the abundance decreases to rare. The sediments recovered below Core 10R are barren of calcareous nannofossils.

Cenozoic (Miocene) calcareous nannofossil assemblages occur in the uppermost part of Unit I (Section 324-U1348A-1W-1 through interval 2R-1, 6 cm). The presence of *Discoaster challengeri, Discoaster druggii, Discoaster deflandrei,* and *Discoaster brouweri* together with *Reticulofenestra pseudoumbilicus* in Sample 324-U1348A-1W-1, 0–6 cm, indicates Zones NN6–NN8 (lower to middle Miocene) (Table **T2**); co-occurrence of a few Upper Cretaceous specimens (e.g., *Uniplanarius gothicus*) is most likely contamination. Sample 324-U1348A-2R-1, 1 cm, contains *Amaurolithus delicatus* next to *Calcidiscus macintyrei, D. challengeri,* and *D. brouweri* and is therefore correlated to Zones NN11–NN14 (middle Miocene). Sample 324-U1348A-2R-1, 2 cm, displays nearly the same assemblage (Zones NN6–NN16) (Table **T2**) as Sample 324-U1348A-1W-1, 0–6 cm, except for the additional occurrence of *C. macintyrei.*

The change in color from light gray to pale yellow around the top ~6 cm of Section 324-U1348A-2R-1 marks the difference between Cenozoic and Cretaceous oozes. The presence of *Arkhangelskiella cymbiformis* in Sample 324-U1348A-2R-1, 6 cm, and of the pale yellow ooze together with *Uniplanarius gothicus, Eiffellithus eximius,* and *Reinhardites levis* is assignable to Zones UC13–CC24 (Santonian to Maastrichtian) (Table **T2**). The five additional samples taken from the pale yellow ooze of Sections 324-U1348A-2R-1 through 2R-CC represent a moderately to poorly preserved assemblage and cover the stratigraphic range from the Coniacian to Maastrichtian, as indicated by the presence of such species as *E. eximius* and *U. gothicus.*

Samples taken from Cores 324-U1348A-3R through 6R display rare specimens of poorly preserved Watznaueriaceae. Exceptionally, Sample 324-U1348A-4R-1, 0–1 cm (chert-encrusting chalk), illustrates the Santonian Stage (Zones CC14–CC16) by the presence of *Eprolithus floralis* and *Micula decussata* (Table T2). This determination may be compromised by the co-occurrence of a few specimens of *U. gothicus* and *Micula staurophora* of Zones CC17–CC24 (Campanian to Maastrichtian), but they are regarded as contaminants from the upper levels primarily because of their rare abundance.

Between Cores 324-U1348A-7R and 10R, the preservation of calcareous nannofossils is poor and the abundance is rare. The presence of *E. floralis* is the sole indicator that allows assignment of this interval to Subzone NC7a–Zone CC16 (Aptian to Santonian). In Sample 324-U1348A-9R-1, 19–20 cm (Table T2), *Rhagodiscus robustus* is found together with *Cretarhabdus striatus,* which roughly points to the range between Aptian and Albian Stages.

## Foraminifers

### Planktonic foraminifers

The planktonic foraminifer record of Site U1348 (stratigraphic Unit I) is marked by the stratigraphically continuous occurrences of typical mid- to Upper Cretaceous (lower Aptian–lower Campanian) assemblages (Table T3; Fig. F23). Despite limited availability of sediments at most examined levels (with notable exceptions of Cores 324-U1348A-2R and 10R), foraminifer abundance and diversity are generally high. Two samples from Cores 8R and 9R show significantly limited occurrences of planktonic foraminifers, and instead, the benthic foraminifer abundance is relatively high. The preservation is generally good throughout the examined section, though occasionally is poor owing to replacement by silica (Table T3).

Two pale yellow ooze samples from Core 324-U1348A-2R are correlated to the Santonian–lower Campanian interval based on well-preserved diverse planktonic foraminifer assemblages. In particular, Sample 324-U1348A-2R-CC, 12–15 cm, falls within the *Dicarinella asymetrica* Zone based on the abundant occurrence of the nominal taxon, together with abundant *Contusotruncana fornicata, Marginotruncana sinuosa, Marginotruncana pseudolinneiana,* and *Sigalia deflaensis*. Sample 324-U1348A-2R-1, 9–10 cm, above, is marked by rare to few *C. fornicata, Globotruncana linneiana, Globotruncana arca,* and *Globotruncanita stuartiformis*. The absence of *D. asymetrica* implies that this level is above the top of the *D. asymetrica* Zone and therefore is the lower Campanian.

The Turonian Stage is recognized for two samples (324-U1348A-3R-1, 0–1 cm, and 4R-1, 0–1 cm). The latter sample is marked by good planktonic foraminifer preservation and yields rare *Helvetoglobotruncana helvetica* (nominal taxon of the *Hv. helvetica* Zone) together with abundant *Whiteinella aprica* as well as few *Whiteinella archaeocretacea* and *Whiteinella baltica*. Noteworthy is the high abundance of biserial heterohelicids, up to 36% in total planktonics ($N$ = 192; >150 µm), which is ascribed to the so-called "*Heterohelix* shift" (Ando et al., 2009b, and references therein). In contrast, Sample 324-U1348A-3R-1, 0–1 cm, represents poor preservation of planktonic foraminifers, as all retrieved specimens are replaced by silica and the sample does not include the primary zonal marker species. Yet, few to common occurrences of marginotruncanids (*M. sinuosa, M. pseudolinneiana,* and *Marginotruncana renzi*) together with the absence of *Hv. helvetica* or *Dicarinella concavata* are indicative of the upper Turonian.

Sample 324-U1348A-5R-1, 0–1 cm, despite limited recovery of planktonic foraminifers, represents the presence of zonal marker species *Ticinella primula,* which represents the middle–upper Albian interval. Further, the presence of rare *Hedbergella wondersi* points to the upper Albian, as this taxon occurs within the *Rotalipora ticinensis* Zone in the western North Atlantic (Petrizzo and Huber, 2006).

Two samples (324-U1348A-6R-1, 0–1 cm, and 7R-1, 6–7 cm) are correlated to the middle Albian, as they are marked by the dominance of zonal marker *T. primula*. Of these, Sample 324-U1348A-6R-1, 0–1 cm, is also marked by the common occurrences of *Ticinella madecassiana* and *Ticinella roberti,* and this observation allows this level to be placed in the upper part of the *T. primula* Zone. Sample 324-U1348A-7R-1, 6–7 cm, below, is dated as the lower part of the *T. primula* Zone, as judged from the somewhat smaller size and less pronounced supplementary apertures in *T. primula,* as well as the abundant occurrence of *Hedbergella rischi* (sensu Bellier and Moullade, 2002).

Downhole, the planktonic foraminifer records are interrupted by sparse occurrences in Cores 324-U1348A-8R and 9R but are again marked by the common occurrence with good preservation at the top of Core 10R (~22 cm thick white ooze), which can be designated as the lower Aptian. Representative taxa in the examined two levels (Samples 324-U1348A-10R-1, 1–2 cm, and 10R-1, 20–21 cm) are *Pseudoschackoina saundersi, Globigerinelloides aptiensis, Globigerinelloides maridalensis,* and *Praehedbergella gorbachikae* (Boudagher-Fadel et al., 1997; Verga and Premoli Silva, 2003a, 2003b, 2005). Taking account of the lack of large multichambered (>7 chambers)

middle to late Aptian representatives of the genus *Globigerinelloides* (i.e., *Globigerinelloides ferreolensis* and *Globigerinelloides algerianus*), which were reported from the same central Pacific domain (Deep Sea Drilling Project Site 463, Mid-Pacific Mountains; Ando et al., 2008), it is most reasonable to consider that the ooze sediments of Core 324-U1348A-10R fall within the *Leupoldina cabri* Zone.

### Benthic foraminifers

Two modes of benthic foraminifer occurrences are observed in stratigraphic Unit I in terms of abundance and diversity: (1) low-abundance assemblage through Cores 324-U1348A-2R through 8R and (2) high-abundance, high-diversity assemblage in Cores 9R through 10R (Table **T4**). The faunal elements are interpreted primarily as reflecting the subsidence history of Tamu Massif from the upper to lower bathyal depth.

In the low-abundance assemblage of Cores 324-U1348A-2R through 8R, benthic foraminifers constitute 2%–6% of total foraminifer counts with moderate diversity. With specific reference to two Santonian–Campanian samples from Core 2R, *Aragonia* and *Sliteria* are the dominant elements (cf. Widmark, 1997). These genera are the representatives of the middle to lower bathyal setting (Nyong and Olsson, 1984 [*Sliteria* reported as *Conorbina*]). Although the habitat of *Aragonia* may extend to the abyssal depth (Sliter, 1977), it is notable that agglutinated benthic foraminifers typical of the abyssal setting (e.g., Nyong and Olsson, 1984; Sikora and Olsson, 1991; Holbourn et al., 2001) are lacking, thereby allowing the estimation of middle–lower bathyal depth (<2500 mbsl) for these levels.

In another set of the low-abundance benthic assemblage in Cores 324-U1348A-4R through 8R (Albian–Turonian), calcareous trochospiral genera *Gyroidinoides* and *Osangularia* are the most common faunal elements, both of which are ubiquitous in the bathyal setting. Of these, *Gyroidinoides* has been revealed to dominate in the upper–middle bathyal depth (Sliter and Baker, 1972; Nyong and Olsson, 1984; Sikora and Olsson, 1991; Ando et al., 2009a). Additionally, the neritic to upper bathyal elements (e.g., nodosariids) are lacking. In summary, the reasonable bathymetric range for this assemblage would be the middle bathyal (500–1500 mbsl).

The Aptian benthic foraminifer assemblage in Cores 324-U1348A-9R and 10R represents a peculiar mode of occurrence, exhibiting significantly high abundance (49%–90% in total foraminifer counts) and high diversity. Calcareous trochospiral taxa are dominated by *Gyroidinoides* and *Osangularia,* together with small *Gavelinella*. Large-sized agglutinated forms of *Dorothia* and *Gaudryina* are also prevalent. Such faunal composition is reminiscent of the upper to middle bathyal setting (Sliter and Baker, 1972). Further, this assemblage is marked by the entries of some nodosariid taxa (*Laevidentalina, Lenticulina,* and *Saracenaria*) indicative of the upper bathyal setting. It is most reasonable that these observations are translated as indicating the upper to middle bathyal depth (200–1500 mbsl).

## Igneous petrology

### Stratigraphic unit description

Hole U1348A was drilled on the north flank of Tamu Massif of Shatsky Rise (Fig. **F1**). The top of the drilled succession (Figs. **F24, F25**) is a Cenozoic–Cretaceous chert-chalk series (stratigraphic Unit I) and poorly recovered bioclastic sandstones partially cemented with a mixture of calcite and silica (stratigraphic Unit II). The bioclastic sandstones contain a small proportion of volcaniclastic material (e.g., basaltic fragments and individual feldspar crystals) and are intercalated with two well-developed clay horizons, most likely representing two tuffaceous ash horizons (see **"Sedimentology"** for details).

The "seismic basement" was reached at the top of stratigraphic Unit III (~200 mbsf) in Section 324-U1348A-14R-1, after which drilling continued for ~120 m into a succession of highly altered hyaloclastic material (stratigraphic Units III–VI). The hyaloclastic sequence has been further divided into four units based on macroscopic core descriptions, including differences in the modal clast size, degree of matrix or clast support, occurrence or absence of bedding features, and proportions of constituent components. The primary features of the hyaloclastite sequence, however, have been profoundly altered. From a purely volcanological perspective, the description of Units III–VI presents a challenge; in many instances, a volcanological interpretation is only possible through detailed microscopic examination. The following sections provide a general description of the hyaloclastite Units III–VI and their volcanic constituents. This overview should be considered in close association with descriptions given in **"Sedimentology,"** which in addition contains comments regarding the sedimentology, primary origin, and reworking of the hyaloclastic material. Physical descriptions of the rocks and identification of the cementing minerals were assisted by XRD determinations.

### Layered granular hyaloclastite (Unit III)

In general, this is a granular hyaloclastite succession mostly containing moderately sorted clast-supported granules but ranging up to matrix-supported breccias (e.g., interval 324-U1348A-17R-1, 20–60 cm) containing ~40% vitrous basaltic fragments. The vitric fragments retain pseudomorphs of acicular plagioclase, a low abundance of small vesicles, and a spongy texture conferred by the development of alteration spheroids in the original glass (for examples see Thin Section 157; Sample 324-U1348A-14R-1, 18–20 cm, and intervals 17R-3, 52–54 cm, and 17R-3, 93–95 cm). Grain size variations reveal reverse grading, passing upward from poorly sorted hyaloclastite siltstone and sandstone into occasional thin layers of granular hyaloclastite (Fig. **F26**). This may represent direct deposition of volcanogenic material into water, with larger vesicular hyaloclasts (lapilli size) (Fig. **F26C, F26D**) remaining more buoyant and falling through the water column more slowly than the smaller, denser fragmental material. Finer layers consist of glass shards (cuspate vitric fragments) with a significant clay matrix produced by alteration (Fig. **F26E**). All these fragments are now entirely replaced by secondary palagonite and cemented together by zeolite and calcite. Some finer horizons preserve small-scale cross lamination and ripple structures, indicating wave or current reworking (e.g., in Subunit IIIc; Thin Section 161; Sample 324-U1348A-15R-1, 55–57 cm). Determination of the primary and replacement mineralogy of different clast types contained within the coarser layers of this unit proved extremely difficult, both from core observation and petrographically.

Angular clasts as long as 3–5 cm occur in Cores 324-U1348A-14R (Subunit IIIa) and 15R through 17R (Subunit IIIc), and a number of these clasts are clearly volcanogenic and basaltic, containing acicular plagioclase crystals, chilled margin zones, and vesicular textures. Examples of these glassy clasts were analyzed by ICP-AES and confirm an original basaltic composition similar to that determined for basalts from Hole U1347A on Tamu Massif. Also present are fragments of very fine grained, highly altered "honeycomb" spheroid-rich material, for which immobile trace element concentrations also confirm a parental basaltic composition (see **"Geochemistry"**).

### Fossil-bearing hyaloclastite sandstone (Unit IV)

In terms of grain size, this stratigraphic unit is a volcanogenic sandstone succession containing horizons of much larger (pebble size) clasts. Sedimentary laminations are preserved in some intervals, but elsewhere these are completely destroyed by bioturbation. Profoundly altered dark gray and brown weathered angular clasts of vesicular basalt are scattered throughout this lithology. Honeycomb spheroid-rich fragments are numerous and represent reworked and profoundly altered volcanogenic vitric material. In addition, partially replaced cuspate glass shards, together with fragments of broken feldspar, can still be recognized in matrix material (interval 324-U1348A-20R-4, 77–81 cm). Small shell fragments are common within this succession, including sparse examples of entire ammonites and fragments of large bivalves. These shell fragments likely represent part of an allochthonous component, possibly brought in by turbidity currents sourcing material from shallower water environments.

### Layered granular hyaloclastite (Unit V)

Unit V is a layered granular hyaloclastite. Individual grains are completely replaced by zeolite and calcite but originally were either vitric clasts or glass shards. Some sections consist of moderately sorted clast-supported granules, probably lapilli, and contain a few fine-grained intercalations. Grain size variations reveal fining-upward packages interpreted as turbiditic reworking of an original volcaniclastic source (see **"Sedimentology"**). The layering in Unit V is inclined, which may represent core sections through original cross-bedding structures or else could represent overall dipping of this sequence at 5°–25° (see **"Structural geology"** and **"Downhole logging"** for more details).

### Massive clast-supported hyaloclastite breccia (Unit VI)

Unit VI is a massive, granular-textured succession consisting predominantly of closely packed clasts, many larger than 2 cm. Individual smaller volcanogenic grains or glass shards are completely replaced by zeolite and calcite and occur in crushed layers of subspherical "shells" (<1 mm). These shells are unlikely to be primary because they are too regular in shape to represent altered vesicle fillings and, instead, most probably originated as alteration "spheroids" that developed from quench mineral spherulites in vitric shards during an earlier stage of alteration. Interestingly, in a ~26 cm interval in the top of Unit VI, these vitric clasts still contain ~50% of their original volcanic glass (Fig. **F27**), providing a unique record of the composition of these volcanic constituents before compaction and alteration (see **"Petrology and igneous petrology"** for a description of this interval). Postemplacement "ptygmatic veins" indicate differential compaction throughout the succession and are most accentuated in the coarser hyaloclastite layers.

### Relation of unit division to downhole logging data

Downhole logging measurements (Fig. F28) indicate low resistivity throughout Hole U1348A. The lowest resistivity occurs throughout the sediments of stratigraphic Units I and II. Typically, higher values were recorded in the "seismic basement," with the highest values of the succession in Subunits IIIa and IIIc and Unit V and lower, intermediate values throughout Units IV and VI. Accordingly, variation in resistivity confirms the primary stratigraphic divisions based upon the core observations outlined above. A notable resistivity peak occurs in the top of Unit VI and most likely corresponds to the ~26 cm thick, calcite-cemented layer that also contains a high proportion of fresh volcanic glass (see above). Total NGR counts (Fig. F28) are low throughout Unit I and highest in Units III–IV. Isolated, narrow gamma ray peaks for Th correspond to layers in Unit II, possibly the altered ash horizons (Fig. F29). Gamma ray peaks for U most likely correspond to the fossil-rich sandstone layer of Subunit IIIb and two unrecovered interbeds in the top of Unit IV (~246 mbsf) and the middle of Unit V (~271 mbsf). Oscillating total gamma ray counts in both Units IV and V may correlate with the observed bedding and grain/clast-size variation.

Magnetic susceptibility is an order of magnitude lower than in basaltic basements of Holes U1347A and U1350A. Also, the log density is relatively low throughout, reflecting the high degree of alteration. Another reason is that the Hole U1348A materials are not hard rock but volcaniclastics (Fig. F30). Porosity is as high as 27%–55% throughout the succession but decreases systematically downhole in Unit VI as a result of compaction (see also **"Physical properties"**).

## Petrology and igneous petrology

Given the profound degree of alteration within the volcanogenic succession and the difficulty in recognizing primary igneous features in what apparently formed as a hyaloclastite, it is important to outline the process of alteration and transformation. Basaltic clasts can be recognized in all of the volcanogenic units from thin section, but with increasing uncertainty in the lower part of the succession (see description summaries in 324TS.XLS in LOGS in **"Supplementary material"**). Unit VI is particularly enigmatic. In this unit, the presence and recognition of clast material has been a source of debate; however, partially altered glass shards that retain many of their primary characteristics have been identified in a ~26 cm interval (Fig. F27). Other than this one example, the bulk of the succession presents itself as a zeolite- and calcite-cemented altered hyaloclastite mass containing variable quantities of palagonitized vitric and lithic remnants, with palagonite spheroids imparting a honeycomb texture.

In thin section, spherulites were obviously a ubiquitous quench feature in the volcanogenic fragments; these have been subsequently converted to alteration spheroids, in particular throughout Units V and VI. The largest of the resulting spheroids are of the order of ~1–2 mm in diameter. Some spheroids are open and others are clay-lined, whereas some are partially to completely filled with white calcareous or siliceous minerals. In hand specimen, the spheroids impart a honeycomb-like texture to the fragments. Individual elements of this texture are discernible as numerous, rounded, evenly distributed, and consistently sized particles that can be mistaken for infilled vesicles, constituents of a biological origin (e.g., infilled and/or recrystallized radiolarian infusoria), or, because of their clay-rich composition, particles of detrital origin. However, recognition of volcanic attributes in thin sections (e.g., basaltic textures, clasts with angular/irregular shapes, and pseudomorph "outlines" of glass shards) leads us to dismiss these interpretations. Accordingly, the sediments of Units III–VI are interpreted as an unusual variety of palagonitized (altered) hyaloclastite consisting almost entirely of profoundly altered basaltic volcanic glass. Within these hyaloclastites, the original fragmental or shard structures have been broken down into fine angular fragments ranging in size from micrometers to a few centimeters and always containing a high abundance of spheroids.

### Examples of hyaloclastite formation

Hyaloclastites (Rittman, 1958) are glassy fragmental volcanic rocks. The presence of volcanic glass indicates extremely high cooling rates that are obtained only by contact with water, and, for significant quantities of glass to be formed, it requires that the lava either flowed into or erupted under water. Pillow lavas forming at spreading ridges experience extremely high cooling rates, yet never produce glassy margins thicker than 2–3 cm (Kirkpatrick, 1979). They therefore do not normally spall into thick piles of purely glassy material, which may be a function of eruption into deep water (>2500 mbsl) at pressures above the triple point of water. At shallower depths, the formation of water vapor facilitates rupture of the glassy chilled crust along fractures induced by contraction of the quenched pillow rim, and as a result hyaloclastites are generated more abundantly in water shallower than ~500 mbsl. It is thought that the great majority of hyaloclastites dredged from seamounts probably formed by this kind of spalling of pillow surfaces. Submarine "lava fountaining" is also

known to produce glass shards called "limu o Pele," which were first described in Hawaii around the propagating margins of submarine lava flows (Clague et al., 2009).

Fragmentation of the surfaces of pillow lavas in shallow water often forms breccia deposits that are mixtures of glass shards and pillow fragments, called "aquagene tuffs" (Carlisle, 1963). However, the finer glass fractions of such breccias can become entrained in the water column and separate to form a cloud of suspended material that eventually is deposited on top of the broken pillow mass. Carlisle (1963) termed these "laminated aquagene tuffs" and, in British Columbia where he observed them, they can be several meters thick and up to hundreds of meters wide in outcrop. However, possibly the most dramatic example of this type of deposit is two beds of altered and cemented hyaloclastites, each several meters thick, that were drilled at ODP Site 1223 on the crest of the Hawaiian Arch (Stephen, Kasahara, Acton, et al., 2003). These hyaloclastites were derived from the great Nu'uanu landslide, which carried away almost half of the Ko'olau Volcano of the island of Oahu, Hawaii, ~2 m.y. ago (Moore and Clague, 2002). Presumably, the glass was generated by submarine eruption(s) when the whole side of the volcano fell away and the Ko'olau magmatic rift system became exposed to seawater. The glass shards were then entrained in turbidity currents that reached as far as 200 km from their source and deposited hyaloclastites that now are moderately to extensively altered to palagonite and cemented by clays and zeolite in a similar fashion to the alteration observed in Hole U1348A.

## Background on palagonite formation in the sea

A classic work on the petrography of palagonite is that of Peacock (1926), who described altered Icelandic tuffs that formed in melted pools of water beneath glaciers. Palagonite is a combination of iron oxyhydroxides and clays replacing basaltic glass. Two types of palagonite were recognized by Peacock (1926): (1) gel-palagonite, which is orange in thin section, has no birefringence, and often forms rims around hyaloclastite glass shards; and (2) fibro-palagonite, similarly orange in color but in which the constituent clay minerals are clearly discernible and which shows birefringence under the microscope. Fibro-palagonite typically forms distinctive rims around glass or gel-palagonite. It also projects radially around tiny spheroidal objects that are lined or filled with clays and develop during palagonitization of glass. Peacock (1926) called these "spherulites," but in modern usage this term is now most commonly applied to fibrous radiating crystal masses of plagioclase and clinopyroxene produced at pillow margins during quenching of lava. In this volume, to avoid confusion, we use the term "spheroid" in place of Peacock's spherulite to denote these alteration products. Both gel- and fibro-palagonite are developed in the tuffs of Site 1223, which could well be considered the prototype for the altered rocks recovered at Site U1348.

Nevertheless, palagonitization in rocks of Hole U1348A is far more extensive than observed at Site 1223 because prolonged alteration has significantly modified even the palagonite itself. The possible origin of this transformation will be discussed later, but the transformation to clays and the formation of both open spheroids and zeolites involves both uptake of water and an increase in porosity of every glass shard so affected. The origin of the alteration spheroids is obscure, and they may readily be confused with clay-lined and zeolite-filled vesicles that originally may have been present in the shards. Quite often, however, the alteration spheroids are so densely packed in individual grains that they would imply an improbably high vesicularity in the original lava fragment. However, in thin section, alteration spheroids are more readily distinguished because they often touch, are almost always nearly circular in plan, and never overlap or coalesce. By contrast, vesicle textures often reveal flattened, distorted, or coalesced forms.

## Process of volcanic glass shard transformation

The proposed sequence of transformations that generates the spheroids from the volcanic glass shards (and basaltic clasts) is complex but may be summarized as shown in Figure **F31**. The original volcanic glass is first replaced through a process of palagonitization, which progresses from the outside inward, and along existing fractures, producing a rim of orange or brownish orange clay materials around the glass shard (or volcanic fragment). During this process, spheroids of clay materials begin to form in radial aggregates within the palagonitized regions of the shard, thus conferring a "cellular structure" within. As noted, these incipient spheroids can be easily confused with vesicles but are entirely secondary in origin. By this stage, the alteration has produced a series of clay boundaries both around the shard and around the spheroids inside. Further alteration entirely replaces all of the remaining primary glass as zeolite (and calcite). The material remaining consists of the pseudomorphed outlines of the original glass fragments, preserved as thin clay rinds set within a zeolite matrix. In addition, within these pseudomorphs, a honeycomb texture is produced from the continued development and formation of

spheroid margins that also are preserved in clay. By this stage, virtually all of the primary glass shard mineralogy and physical structure are obliterated. The next possible stage in this evolution is caused by compaction through increasing overburden and/or through mechanical weakening caused by the mineral replacement processes described above. Compaction crushes the rims and distorts the shape of the spheroids. Continuation of this process results in a fine-grained material consisting almost entirely of curved fragments with clay rims and spheroids set in a zeolite/calcite matrix. At this stage most characteristics that might identify the original volcanic parentage of the rock have been entirely erased.

A series of photomicrographs reveals this transformation process in detail, beginning with the example of unaltered glass cemented by calcite in the top of Unit VI (Figs. **F27, F32**). The well-preserved glass fragments range in size from ash- to lapilli-size angular particles and contain crystallites of primary igneous silicate minerals (i.e., plagioclase needles) and occasionally vesicles. Spheroids are well developed in only one fragment, at the lower left of Figure **F32A,** which is a region nearly entirely replaced by matrix cement. These spheroids are defined by rims of clay, some touching but never merging. The once contiguous glass shards in the upper part of Figure **F32A,** form a fragmented arrangement separated by alteration products. The cementing matrix of calcite forms about half of the view in Figure **F32A,** and about a third in Figure **F32B.** Many fragments are defined by curving outlines clearly related to the tendency of glass to break along conchoidal fractures and are independent of the original placement of vesicles. The contiguous nature of adjacent fragments indicates that glass fragmentation in this sample occurred in situ, after deposition, with little or no subsequent movement of the depositional material. Moreover, cementation with calcite must have occurred soon afterward and acted to seal the freshness into this unique portion of the rock.

Figure **F33** is a composite of photomicrographs covering the entirety of the large fragment at the top of Figure **F32B.** Here, the upper edge of the fragment and a roundish patch toward its middle are partially transformed to a darker brown palagonite, and fibropalagonite rims surround two oblate vesicles on the left. The glass is broken into segments ~0.5–1 mm long by cracks, some of which were avenues for alteration fluids to penetrate the interior. Incipient round spheroids containing clays but retaining the pale brown color of the glass occur at the lower right. Details of the cracking pattern in the vitric clast are shown in Figure **F34A.** Alteration to fibrous clays is enhanced along some cracks but not along others; the development of fibropalagonite spheroids is clearly controlled by the crack porosity structure. Although the glass contains primary plagioclase and clinopyroxene (crystals clustered on the right in Fig. **F34B**) and even fresh olivine (on the left), there is no spherulitic crystallinity of the type that forms near the margins of rapidly cooled pillow lava. Plagioclase-clinopyroxene intergrowths also occur (Fig. **F34C**). The spheroids in Figure **F34D** and **F34E** have almost the same color as the basaltic glass; their rims are composed of radiating aggregates of tiny clay minerals, tiny acicular plagioclase, and feathery dendritic clinopyroxene.

Figure **F34D** and **F34E** show how spheroids form during incipient alteration of basaltic glass along microscopic fractures in the glass and that they are not vesicles filled with clays. In all the rest of the palagonitized glass of Hole U1348A, this process proceeded to an advanced degree so that very little fresh glass remains.

Most of the rocks, whether cross-bedded or clast-supported, originally must have consisted of abundant angular fragments of altered glass that now contain, or are overprinted by, abundant alteration spheroids (Fig. **F35A**), and later by zeolite and calcite. Many samples contain pseudomorphs of very irregular fragments that originally may have been fragments of glassy bubble walls. These are now rimmed with fibropalagonite and have interiors replaced by brownish palagonite (most probably gel-palagonite) and are completely transformed to dark brown clays (Fig. **F35B**). In the case shown, the shard is partially encased by secondary rhombic calcite. Other fragments have stretched or riblike internal structures (Fig. **F35C**), evidently a consequence of stretching while still plastic during their original formation; these also retain their well-defined rims of fibropalagonite and have interiors completely replaced by dark brown clays. In some fragments, the density of alteration spheroids approaches 100% (Fig. **F35D**). However, original angularity and interior vesicle structures of fragments are often clearly retained by the former fibro-palagonite rims (Fig. **F35E**), even though the interiors are almost completely replaced by cementing calcite. In this case, all fragments are cemented by zeolite. If this arrangement reflects an original packing condition, then the original bed form was clearly both very porous and loosely packed.

Figure **F36** shows details of the cementation of the vitric clasts. Figure **F36A** depicts an example of an angular, originally vesicular, fragment retaining its fibrous rim but with an interior completely replaced by cement. Figure **F36B** reveals calcite replacement of the interior of a fragment surrounded by almost

nonbirefringent zeolite. Figure F36C shows a fibrous calcite infilling surrounded by clays. Figure F36D and F36E shows palagonite fragments now altered to green clay, and the whole appearing to be matrix-supported by cementing zeolite. In the cement, two or more zeolite types may be present; the most abundant one forms needlelike radiating arrays around fragments with preserved rims of fibro-palagonite (Fig. F36F). The other zeolite morphology is blocky and irregular even within spheroids and filled-in vesicles (Fig. F36G).

### Preliminary assessment

Interpretation of the ~120 m of volcaniclastic rocks in Hole U1348A on Tamu Massif presents an array of scientific challenges. Even though the volcanogenic origin of Units III–VI is not in dispute, initial interpretation as the cores arrived on deck was difficult. The main issues were whether the deposits were derived from proximal or distal sources, whether they were wholly or only partly produced by submarine volcanic action or whether any of the material was pyroclastic (that is, traveled through air after explosive eruption), and, finally, whether they contain one or more varieties of lava. Based on the shipboard mineralogy of fresh glass discovered in the ~26 cm interval in Core 324-U1348A-23R at the top of Unit VI (Fig. F27), we conclude that the protolith for the altered hyaloclastites was submarine volcanic glass saturated in olivine, plagioclase, and clinopyroxene. ICP-AES analyses on some rare basaltic clasts (see "Geochemistry") confirm that compositionally the protolith was no different from basalts drilled at other sites on Tamu Massif, especially the fresh glassy basalts of Hole U1347A.

Accepting this origin, then all igneous material in the cores was once rapidly quenched basaltic volcanic glass. The origin of this basaltic glass is a matter for debate; no evidence was found that unequivocally attributes the formation of Hole U1348A volcaniclastic rocks to the process of disaggregation of basaltic lava resulting from lava entering the sea from land, or to derivation from other types of subaerial explosive eruptions. However, the observation that the overwhelming percentage of volcanic material in the cores was originally clear, brown, sharply angular, and relatively nonvesicular basaltic volcanic glass might indicate a submarine volcanic source. The fragmentation mechanism must have been spallation assisted by expansion of heated seawater in the form of vapor that expanded in cracks in the congealing magma (and not in the sparse vesicles), as the glass fracturing was mainly conchoidal. Also, the few fragmental pieces of originally holocrystalline basalt that are present could be sourced from the chilled margins of lava pillows (Fig. F37).

The great majority of these vitric clasts and glass shards have now been completely altered by a prolonged process of palagonization to spheroid-bearing hyaloclastite. The finer grained portions are well bedded, preserving attributes of particle sorting, grading, and scouring consistent with turbiditic deposition (Units III and IV). Given that their constituents were originally mainly vitric clasts, they can be termed laminated hyaloclastites (Carlisle, 1963) and may, therefore, indicate transport in suspensions that moved rapidly across the seafloor near the base of the local water column. Other, more coarsely bedded material was found toward the base of the hole (Units V and VI) and was almost certainly deposited closer to the putative submarine volcanic source(s).

## Alteration and metamorphic petrology

Volcaniclastic rocks recovered from Hole U1348A (Cores 324-U1348A-14R through 26R) have been extensively altered, resulting in a near-complete replacement of primary glass in the vitric clasts and almost complete replacement of primary phases present in the rare lithic fragments. Fresh glass was observed only in one 6 cm thick layer in interval 324-U1348A-23R-1, 116–122 cm. Clay minerals, together with calcite and zeolites, are the predominant secondary minerals in Hole U1348A cores, replacing glass and primary minerals, filling voids, and cementing volcanic clasts.

### Alteration mineralogy

Alteration degree and mineralogy of Hole U1348A cores is based on thin section description and X-ray diffraction (XRD) analysis on bulk rock powder (Table T5). The fine-grained nature of the volcanic clasts causes difficulties in identifying the alteration mineralogy in hand specimen.

#### Secondary mineralogy

Vitric and lithic clasts forming the volcaniclastic rocks in Hole U1348A are all extensively altered, except in one interval (324-U1348A-23R-1, 116–122 cm; see "Igneous petrology" for further description). Rims of the vitric clasts are mainly altered to green-brown palagonite (Fig. F38), preserving the outline of the clasts. Based on XRD spectra, minerals forming the palagonite are mainly nontronite and montmorillonite (Fig. F39). The inner part of the vitric clasts shows two different textures: (1) alteration

of glass to palagonite and clays and (2) complete dissolution of glass and replacement by calcite and/or zeolites (Fig. F40), with zeolites showing a fibrous and/or blocky morphology. Lithic clasts also show a high degree of alteration with almost complete replacement of glassy mesostasis to palagonite and brown clays (e.g., nontronite and montmorillonite, based on XRD spectra), whereas plagioclase microliths remain relatively unaltered (Fig. F41). Lithic fragments in Thin Section 158 (Sample 324-U1348A-14R-3, 54–56 cm) show a similar texture and alteration degree to basaltic rocks recovered from the top of Hole U1347A (Fig. F41).

The vitric and/or lithic clasts are cemented by calcite and/or zeolites (Figs. F40, F42) with variations in their proportions and occurrences downhole (Fig. F43). Zeolites form a corona alteration around the palagonite rims of the vitric and lithic clasts (Fig. F44). Two types of zeolites were observed in the corona alteration: (1) a fibrous zeolite and (2) a tabular blueish zeolite identified as phillipsite. This is consistent with XRD spectra, which indicate the presence of phillipsite in bulk rock samples (Fig. F39). Calcite cement occurred at a late stage, filling the empty space between the highly altered clasts.

### Variations in mineralogy downhole

Based on identification of secondary minerals on XRD spectra and observations of thin sections, alteration mineral assemblages appear to vary downhole (Fig. F43; Table T5). Phillipsite and calcite are the most abundant secondary minerals and are associated with montmorillonite, nontronite, and sepiolite, with variations in their occurrences with depth in Hole U1348A. Celadonite and palygorskite were observed in the sedimentary cores in the upper part of the hole (stratigraphic Unit II; Section 324-U1348A-12R-CC at 180.77 mbsf and interval 324-U1348A-12R-1, 17–18 cm, at 180.5 mbsf), and further details and interpretations are given in "Sedimentology" Palygorskite has also been identified in the volcaniclastic rocks at the bottom of Hole U1348A, from Section 324-U1348A-20R-2 (258.8 mbsf) to 22R-4 (Fig. F43).

### Interpretations

The volcaniclastic rocks recovered from Hole U1348A are all highly altered to various smectites and zeolites, which are the most common minerals to form during alteration and palagonitization of volcanic glass. The smectites identified to form the palagonite in Hole U1348A are predominantly montmorillonite (Ca smectite) and nontronite (Ca and Fe smectite). Occurrences of these two minerals indicate palagonitization in open marine systems (see Fisher and Schmincke, 1984, for a review). Phillipsite is present in the entire volcaniclastic section in Hole U1348A and is usually one the most common and first zeolite to form during palagonitization.

Palygorskite has been identified in the sediments at the top of the hole as well as in some sections at the bottom (e.g., interval 324-U1348A-20R-2, 36–39 cm; Figs. F39, F43). Palygorskite is often observed in deep marine sediments and commonly forms at the interface between sediments and seawater, where Al and Si may be derived from volcanic ashes and Mg is released during basalt weathering. Palygorskite has also been observed in fractures of basaltic rocks from the Mariana forearc region (Natland and Mahoney, 1982) in association with Fe hydroxides. This secondary mineral assemblage suggests relative oxidizing conditions and moderately elevated temperatures. Occurrences of palygorskite at the bottom of Hole U1348A may similarly suggest interactions of the volcaniclastic rocks with relatively warm hydrothermal fluids. Further shore-based studies will be conducted to better constrain the alteration of these volcaniclastic rocks and the formation of palygorskite.

## Structural geology

Cores recovered from Hole U1348A between 199.5 mbsf in Core 324-U1348A-14R and 324.1 mbsf in Core 26R can be structurally divided into two parts, an upper part consisting of volcaniclastic sediment with well-developed bedding (Cores 14R through 22R) and a lower part made up of coarse brecciated basalt characterized by massive structure (Cores 23R through 26R). The boundary between the parts is at interval 324-U1348A-23R-1, 0 cm. Primary structures and veins described here are solely within the volcaniclastic rocks. Some alteration veins, however, are developed in both sections.

In the following sections, the characteristics of the two major types of structures are described, followed by a discussion of their distribution and orientations, relationships between structures, and a short summary. Important observations and interpretations include (1) preferred orientations of primary structures such as bedding in sedimentary rocks and (2) variation in structural morphology and orientation of veins in both laminated and more massive volcaniclastic rocks.

### Primary structures

Bedding, a major primary structure, can be divided into three types in Hole U1348A. Bedding ranges from massive layering in the lower part to delicate

lamination in the upper part. The latter is especially clearly observed in fine-grained rocks such as granular hyaloclastite and fine hyaloclastite interbedded with thick layers of hyaloclastic breccias (Fig. F45). Most bedding dips are gentle, with slopes of ~0°–5°. Occasionally, steeper bedding is observed but never exceeding 30° dip (Fig. F46). These intercalated gentle and steeper bedding in the hole comprise mesoscale cross-bedding, which is characterized by bedding or lamination oriented at an angle to the true bedding surface. Observed true bedding surfaces include the sharply truncated top surface, the middle cross-bedding, and the bottom horizon that is tangential to the middle cross-bedding. Graded bedding in Hole U1348A is dominated by inverse grading sequences, which can coarsen upward through fine hyaloclastite and/or coarse granular hyaloclastite to hyaloclastic breccia. The clasts in the sedimentary rocks are vitric basalts and poorly sorted, semirounded volcaniclastic rocks. At interval 324-U1348A-26R-1, 12–15 cm, some laminated clasts are offset 1 cm by a microfault with a dip of 50°. However, this microfault cannot be traced beyond the drill core, so it is considered to be an intraformational fault (Fig. F47), which could indicate minor submarine slumping after diagenesis.

The third kind of bedding is chaotic bedding and weak bedding with many volcanic clasts. This structure is often developed between well-stratified hyaloclastic sedimentary rocks and massive volcaniclastics, for example, at interval 324-U1348A-26R-1, 10–20 cm (Fig. F47).

The massive volcaniclastics in the lower part of Cores 324-U1348A-23R through 26R consist of hyaloclastite breccias cemented by calcites and zeolites. The vesicularity of individual hyaloclasts is varied, and some observed high vesicularity could be a result of alteration (see **"Igneous petrology"**).

### Microfaults and veins

Microfaults can be found in intervals 324-U1348A-24R-2, 99–102 cm (297.87–297.90 mbsf), and 117–121 cm (298.04–298.08 mbsf). Some striations are displayed in the fault surfaces of these microfaults. Most microfaults with steeply dipping striations are normal faults based on smoothening downward–directed striations of the fault plane. However, some microfaults are indentified as strike-slipping faults because of horizontal striations in the fault plane.

Veins in Hole U1348A are few, but vein types are complex. Most veins dip at steep angles of 70°–80° and can be divided into three types by color: white, gray, and yellow, which correspond to calcite-filling veins, gray clay–filling veins, and brown clay–filling veins, respectively (Fig. F48). Figure F48A shows a yellowish vein that is curved, ~1 cm wide, and filled with yellow clay and oriented dark green slivers or laths at interval 324-U1348A-18R-2, 70–118 cm. The yellowish vein cuts a white vein and the primary bedding; therefore, it formed later than the white vein. A grayish vein can be observed at interval 324-U1348A-26R-2, 33–43 cm, where the volcaniclastics are characterized by banding with a symmetrical display of different textures or colors on both sidewalls of the vein (lower inset diagram, Fig. F47). Most white veins have an en echelon geometry and are related to postdepositional deformation because they cut the primary bedding, for example, at intervals 324-U1348A-21R-5, 27–60 cm (Fig. F48B), and 15R-1, 58–62 cm (Fig. F48C). We also observe one quartz vein cutting through a piece of chert with obvious bedding at interval 324-U1348A-5R-1, 8–13 cm (Fig. F48D). This shows that many veins developed late relative to volcanism and sedimentation at this site. No direct intercrossing relationship between the gray vein and the other two types of veins are observed in the hole.

## Geochemistry

### Major and trace element analyses

Thirteen samples from Hole U1348A were analyzed for concentrations of major element oxides and several trace elements (Table T6) by ICP-AES (see **"Geochemistry"** in the "Methods" chapter for information on analytical procedures, instrumentation, and data quality). Two samples were bulk specimens from clay-rich intervals in stratigraphic Unit II; one of these samples was from a light green interval (Sample 324-U1348A-12R-1, 17–18 cm), and the other was from a yellow-green interval (Sample 324-U1348A-12R-CC, 6–8 cm) (see **"Sedimentology"**). The remaining eleven samples were from totally altered material within stratigraphic Units III, V, and VI (see **"Alteration and metamorphic petrology"**); six were bulk samples of volcaniclastic rock and five were volcanic clasts that we separated from their matrix. Each of the clasts was crushed to roughly millimeter-size chips, and the chips were hand-picked under a binocular microscope to obtain the least-altered material.

As with the Site U1346 and U1347 data, total weight percentages for the major element oxides vary significantly, from 98.57 to 104.22 wt%. We again normalized the raw major element values to 100 wt% totals in order to facilitate comparison of our results with one another and with data from the literature. The normalized values are presented below the raw data in Table T6 and are used in the figures and in the discussion below.

The two samples from Unit II have moderate (for sedimentary rocks) weight loss on ignition (LOI) values (11.68 and 9.12 wt% in Samples 324-U1348A-12R-1, 17–18 cm, and 12R-CC, 6–8 cm, respectively) and very low CaO concentrations (below the ~0.08 wt% detection limit), indicating that very little, if any, carbonate is present. An absence of phosphate minerals is indicated by $P_2O_5$ contents below the ~0.06 wt% detection limit. The chemical effects of diagenesis are difficult to disentangle from original (i.e., syndepositional) composition in these samples. However, the samples have high $SiO_2$ (62.87 and 58.75 wt%; Fig. **F49**) for their $Al_2O_3$ contents (19.45 and 14.16 wt%), relatively low MgO (3.80 and 4.95 wt%), high $K_2O$ (3.34 and 2.81 wt%), very low $TiO_2$ (0.19 and 0.12 wt%), and high Zr (210 and 281 ppm). No radiolarian microfossils or other biogenic materials were observed in the layers from which the samples were taken (see **"Paleontology"**). Therefore, the two clay-rich layers may contain a significant proportion of wind- and/or water-borne magmatic arc– or continental crust–derived material. However, the presence of silica cement elsewhere in Unit II and of chert in Unit I (see **"Sedimentology"**) suggests that some of the $SiO_2$ in these two layers may have a postdepositional origin through circulating silica-rich solutions derived from dissolution of siliceous microfossils in overlying or underlying beds.

Despite our efforts to avoid alteration in the volcanic material of Units III, V, and VI, alteration remained substantial in all of the samples selected for analysis. Very high LOI values of 25.09 and 27.08 wt% were obtained for bulk Samples 324-U1348-14R-1, 18–20 cm, and 18R-3, 49–50 cm, respectively, as well as very high CaO contents of 38.97 and 29.93 wt%. In contrast, $SiO_2$ concentrations are low (33.63 and 36.81 wt%). Together, these results indicate that a large amount of carbonate was present in the analyzed splits of these two samples, and we do not discuss them further. For the other nine samples, LOI values are lower but still very high (Fig. **F50A**), between 6.22 and 12.86 wt%, except for one sample with 3.69 wt% (cf. LOI values of 0.07 to 3.57 wt% for the Site U1347 basalts or <1 wt% for unaltered tholeiitic basalts). Total alkali contents are as high as 7.87 wt% (Fig. **F49**), even higher than for the Site U1346 samples; the highest values were obtained from clasts. Concentrations of $K_2O$, in particular, appear to have been elevated substantially, though variably, by alteration. Concentrations of $SiO_2$ range between 45.06 and 52.51 wt%. Allowing for alteration-related modification of $SiO_2$, this range suggests the samples are probably all basaltic, or at least were originally. In comparison, $SiO_2$ values in the basaltic volcaniclastic rocks of Ontong Java Plateau ODP Leg 192 Site 1184 lie outside the range of basalt compositions only for the most altered samples, which also have the highest total alkali contents (Mahoney, Fitton, Wallace, et al., 2001; Shafer et al., 2004). Variation diagrams reveal significant alteration-related disturbance of many other elements, including CaO, MgO, MnO, and $Fe_2O_3^T$ (e.g., Fig. **F50B**). Phosphate contents are highly variable, ranging from below the detection limit in Section 324-U1348-26R-2 to 5.98 wt% in Section 17R-3 (Fig. **F50C**). A positive correlation between $P_2O_5$ and CaO is present, and five samples have $P_2O_5$ concentrations >1 wt%, indicative of phosphatization during alteration. In addition, phosphatization has disturbed Y and Sr contents significantly, as evidenced by positive correlations of these elements with $P_2O_5$ (Fig. **F51**). Concentrations of Ba, Ni, Cr, and Zn, and to a lesser extent Sc, Cu, and V, are also likely to at least partly reflect the influence of the pervasive alteration, as these elements define rather scattered distributions in variation diagrams.

Thus, we are left with few elements with which to infer original composition. Two of the most generally alteration-resistant elements during low-temperature and hydrothermal alteration are Zr and Ti (e.g., Cann, 1970; Humphris and Thompson, 1978; Patino et al., 2003). In a diagram of $TiO_2$ versus Zr (Fig. **F50D**), the Site U1348 data define an array very similar to that of the vastly less altered Site U1347 basalts (even including an off-array high-Zr sample resembling the evolved segregation of Site U1347). On this basis, the Site U1348 volcaniclastic rocks appear to have been derived from basalts broadly similar in composition to those of Site U1347.

## Physical properties

Volcaniclastic rocks and sediments in Hole U1348A were characterized for physical properties as described in **"Physical properties"** in the "Methods" chapter. Core sections with continuous intervals longer than 8 cm were run through the Whole-Round Multisensor Logger for measurement of gamma ray attenuation (GRA) density and magnetic susceptibility. Data from whole-round measurements were filtered by a MATLAB code to remove data associated with gaps and small pieces as described in **"Physical properties"** in the "Methods" chapter. The filtered data were then visually double-checked against images of the core section halves. Sections longer than 50 cm were measured with the Natural Gamma Radiation Logger. Thirteen discrete oriented cubic samples were cut from the working half of the cores for

measurement of moisture and density (MAD) properties as well as compressional (*P*-wave) velocities in three directions.

## Whole-Round Multisensor Logger measurements

### Magnetic susceptibility

Results for whole-round magnetic susceptibility in Hole U1348A are summarized in Figure **F52.** The volcaniclastic sedimentary material recovered at Site U1348 has magnetic susceptibilities of $<110 \times 10^{-5}$ SI. These magnetic susceptibility values are an order of magnitude less than those observed in igneous material at Sites U1347 and U1350. Magnetic susceptibility shows an overall decrease downhole roughly correlating with interpreted stratigraphic units (see **"Sedimentology"**). The upper interval from 210 to 242 mbsf (stratigraphic Subunits IIIa and IIIc; Cores 324-U1348A-15R through 18R) is characterized by magnetic susceptibilities of $20 \times 10^{-5}$ to $50 \times 10^{-5}$ SI. The lower interval, from 263 to 320 mbsf (stratigraphic Units V and VI; Cores 324-U1348A-20R through 26R) is characterized by magnetic susceptibilities of $15 \times 10^{-5}$ to $30 \times 10^{-5}$ SI. Moderate oscillations around these averages (e.g., highs up to $100 \times 10^{-5}$ SI in intervals 324-U1348A-17R-1, 0–10 cm, and 58–60 cm; 19R-1, 106–108 cm; 20R-1, 18–118 cm; and 20R-4, 73–92 cm) and smaller variations around $\pm 15 \times 10^{-5}$ SI throughout the entire hole are likely due to sedimentary layering, possibly concentrating magnetically susceptible material in specific horizons (see **"Sedimentology"**).

### Gamma ray attenuation bulk density

The results for GRA bulk density measurements are summarized in Figure **F52.** At Site U1348, volcaniclastic sediment filled most of the liner diameter and GRA bulk density measurements match well with discrete sample bulk density measurements (see **"Moisture and density"** below).

The hole can be divided into four broad intervals based on GRA density. The transitions between these intervals are well correlated with changes in designated stratigraphic units (Fig. **F52**). From 190 to 203 mbsf (Sections 324-U1348A-13R-1 through 14R-3), which corresponds to stratigraphic Unit II–Subunit IIIa, described as altered granular hyaloclastite (see **"Sedimentology"**), the GRA density is generally >2.0 g/cm$^3$, with values as high as 2.4 g/cm$^3$. GRA density is markedly lower between 209 and 242 mbsf in Subunit IIIc, made up of altered granular hyaloclastite to fine hyaloclastite (Sections 15R-1 through 18R-3), with values between 1.8 and 1.9 g/cm$^3$. From 257 to 287 mbsf (Sections 20R-1 through 23R-1), broadly corresponding to the layered granular hyaloclastite of stratigraphic Unit V (see **"Sedimentology"**), the density exhibits a smooth, gradual increase from 2.1 to 2.4 g/cm$^3$. Finally, in stratigraphic Unit VI (hyaloclastite breccia; see **"Sedimentology"**) between 295 and 315 mbsf (Sections 24R-1 through 26R-1), the density drops at the top of the unit and then again shows a gradual increase from 1.8 to 2.1 g/cm$^3$ downhole (Fig. **F52**).

## Natural Gamma Ray Logger

Measurements of NGR are summarized in Figure **F52.** Counts per second at Site U1348 are higher (5–30 cps) than seen in the relatively fresh igneous material recovered at Site U1347 (2–4 cps) but are generally not as high as the counts per second measured in altered igneous material at Site U1346 (consistently 20–30 cps). From 190 to 191.4 mbsf (Section 324-U1348A-13R-1), corresponding to stratigraphic Unit II, described as altered granular hyaloclastite (see **"Sedimentology"**), counts per second are between 10 and 20 cps. Subunit IIIa, composed of alternating layers of granular and fine hyaloclastite and lying between 199.5 and 203.61 mbsf (Sections 14R-1 through 14R-3), has a decreased NGR signal, generally <10 cps. Subunit IIIc is also described as layered granular and fine hyaloclastite but shows an increase to 10–15 cps compared with Subunit IIIa. For a 2 m interval between 240 and 242 mbsf (bottom of Section 18R-3 to top of 18R-4), which marks the transition from Unit III to the volcaniclastic sandstone with fossils of Unit IV, the count rate increases to >30 cps. Between 257 and 287.1 mbsf (Sections 20R-1 through 23R-1), in the layered volcaniclastics of Unit V, the signal is lower and oscillates between 4 and 28.1 cps (average = 10.9 cps). Finally, in the remainder of the hole between 285 and 320 mbsf (Sections 23R-1 through 26R-3) and representing Unit VI (hyaloclastite breccia), NGR drops to an average of 4.9 cps.

## Moisture and density

A summary of results for bulk density, dry density, grain density, void ratio, water content, and porosity on discrete samples is shown in Table **T7.** Density and porosity data are shown in Figure **F53.** The samples cut from the material recovered at this site were prone to crumbling and cracking. Material could be lost during the measurement process (e.g., edges and corners crumbling away); therefore, the reported densities should be considered minima and porosities considered maxima. The high content of hydrous phases (e.g., clays and zeolites; see **"Sedimentology"**) also resulted in the samples cracking after dehydration in the oven at 105°C. Despite cracking,

the samples exhibit the expected inverse relationship between *P*-wave velocity and porosity and positive correlation between bulk density and *P*-wave velocity (Fig. **F54**). The discrete sample from Section 324-U1348A-23R-3 in the hyaloclastite breccia Unit VI is a clear outlier in Figure **F54,** displaying anomalously low *P*-wave velocity for its measured bulk density. However, this sample cracked during a subsequent *P*-wave measurement. Despite the tendency of cracking and crumbling in the samples from Site U1348, the bulk density and *P*-wave velocity data correspond well with downhole logging data (see **"Downhole logging"**).

### Compressional (*P*-wave) velocity

Downhole variation of compressional wave velocity is summarized in Figure **F54** and listed in Table **T8.** As with MAD measurements, these should be treated with caution because of sample cracking and crumbling. The measured *P*-wave velocities do not show a coherent relationship with stratigraphic units, in contrast to whole-round magnetic susceptibility, GRA density, and NGR. This could be due to sample material that was prone to crumbling upon *P*-wave measurement and/or the heterogeneous nature of the sampled cores. However, it is clear that the recovered volcaniclastic sedimentary material is consistently slower than igneous material recovered from Sites U1346, U1347, U1349, and U1350. The measured *P*-wave velocities correspond closely to downhole logs (see **"Downhole logging"**). All measured discrete samples yielded values <3.5 km/s, ranging from 2.09 to 3.32 km/s (average = 2.78 ± 0.79 km/s; $N = 13$).

## Paleomagnetism

Because no basalt was recovered, we only analyzed eight discrete samples from volcaniclastic sediments recovered from Hole U1348A. The samples likely carry a depositional remanent magnetization instead of a thermoremanent magnetization. Therefore, any directional result will be more complicated to interpret.

We used the 2G cryomagnetometer for the measurements because the natural remanent magnetization (NRM) of these samples was too weak to be measured on the Molspin Minispin magnetometer (a few tens of mA/m). Only alternating-field demagnetizations were carried out, using the DTech degausser. Three other discrete samples cut for physical property measurements were too weak even for measurement with the 2G cryomagnetometer; therefore, we could not use them for paleomagnetic measurements. NRM bulk magnetic susceptibilities were also measured. The NRM bulk magnetic susceptibilities are on the order of $10^{-4}$ SI, which is 2 orders of magnitude smaller than the values of basalts recovered from Holes U1346A and U1347A.

The low magnetic susceptibilities (between $4 \times 10^{-4}$ and $8 \times 10^{-4}$ SI) indicate that magnetic minerals are not abundant in these samples. Compared to the basalt samples from Holes U1346A and U1347A, these samples have a higher median destructive field (between 10 and 25 mT), which suggests that the magnetization carriers are single-domain grains (Fig. **F55**). Principal component analysis (PCA) (Kirschvink, 1980) was used to isolate a stable component pointing toward the origin. In five cases, once the low-coercivity overprint is removed, PCA gives fairly good results, with maximum angular deviation values between 3° and 7° (Table **T9**). Inclinations are mostly shallow and positive, between 4° and 23°, although one sample gives a negative inclination (–9°).

## Downhole logging

Downhole logging data obtained from Hole U1348A included natural and spectral gamma ray, density, photoelectric factor (PEF), and electrical resistivity measurements from three depths of investigation. Interpretations of gamma ray and electrical resistivity downhole logs were used to identify 15 logging units in Hole U1348A, with one in the section covered by the bottom-hole assembly (BHA), five in the sedimentary sequences in the open hole interval, and nine in the volcaniclastic section.

### Operations

A wiper trip was completed throughout the open hole, and the RCB bit was released at the bottom of the hole using the mechanical bit release (MBR) before the start of wireline logging operations. The hole was displaced using 86 bbl of barite mud, and the drill pipe was set at 101 m wireline matched depth below seafloor (WMSF). Logging operations in Hole U1348A consisted of two tool string deployments and wireline heave compensator testing that took place in good sea conditions with ship heave fluctuating between 0.5 and 1 m. Downhole logging operations began at 1700 h on 6 October 2009 and were concluded at 0645 h on 7 October after the tools from the second tool string were rigged down.

#### Tool string deployment

##### *HNGS-HLDS-GPIT-DITE*

The wireline tool string deployment consisted of a 22 m long modified triple combo tool string that included a logging equipment cable head (LEH-QT),

digital telemetry cartridge (DTC-H), Hostile Environment Natural Gamma Ray Sonde (HNGS), Hostile Environment Natural Gamma Ray Cartridge (HNGC), Hostile Environment Litho-Density Sonde Cartridge (LDSC), Hostile Environment Litho-Density Sonde (HLDS), digital telemetry adapter (DTA-A), General Purpose Inclinometry Tool (GPIT), and the Dual Induction Tool model E (DITE). During the initial rig up, problems powering up the DITE were encountered. The tool string was taken apart on the rig floor to test the DTC-H, DTA-A, GPIT, and DITE combination. The tests revealed that the previously modified GPIT was not working properly in this tool combination. The GPIT was removed from the tool string, and after the remaining tools passed the surface check, the tool string was lowered at ~1160 m/h. During the descent, one of the two depth encoders failed, and the logging operations continued with only one operational depth encoder. A cable-stretch correction of 3.4 m was applied to the wireline depth to account for the water depth and the weight of the tool string.

Downhole logs were recorded in a downlog pass from seafloor to 322 m WMSF at 550 m/h. Uplog Pass 1, from 326 to 101 m WMSF, was recorded at 275 m/h, and repeat uplog Pass 2, from 326 m WMSF to seafloor, was recorded at 550 m/h.

#### *HNGS-DSI-GPIT-FMS*

The second wireline tool string deployment consisted of a 34.39 m long FMS-sonic tool string that included an LEH-QT, DTC-H, HNGS, HNGC, Dipole Sonic Imager (DSI), DTA-A, GPIT, and FMS. Downhole logs were recorded in a downlog pass, from seafloor to 326 m WMSF at 550 m/h, and in uplog Pass 1, from 329 to 66 m WMSF.

After completion of the Pass 1 uplog and as the FMS caliper arms were entering the pipe, a tension increase of ~800 lb was recorded. The uplog continued until 65 m WMSF while the tool string was checked and FMS caliper arm closure was confirmed. The tool string checks did not reveal any problems, and the prevailing thought at the time was that the bottom of the tool string contained some mud or sediment that produced the recorded tension. The tool string was lowered back into the hole to begin the repeat uplog Pass 2.

After the tool string had been lowered completely outside the pipe, head and surface tension measurements revealed that the tool string was not moving. The tool string was raised and lowered once more to get past what was perceived as a hole obstruction. After encountering the same results, the deployment was terminated and the tool string was raised into the pipe. At this point, the bottom of the tool string became stuck inside the pipe. The FMS caliper arms were reading a fully closed position, and several attempts were made to enter the pipe with ~5 m of play going in and out of pipe. The caliper arms were opened and closed again, and a final attempt did not solve the problems.

At this point, pumping operations began to clear any potential debris that could have been keeping the FMS caliper arms from closing. After steadily pumping for 30 min, increasing the pump rates to a maximum of 50 strokes/min, and trying to reenter the pipe while pumping, the results were the same: an inability to move up or down. The last resort for recovering the tool string consisted of pulling up in increments of 1250 lbf above normal logging surface tension readings of 5500 lbf. Unsuccessful pulling attempts were made at 6750, 8000, and 9300 lbf surface tension readings. A maximum of 9650 lbf (5500 lb head tension), which is the Schlumberger maximum safety limit for pulling with this type of wireline, was also unsuccessful.

After the unsuccessful retrieval operations described above, the Kinley crimper and cutter were deployed to sever the wireline and recover the tool string while tripping pipe (see **"Operations"**). The wireline was spooled after it was severed, and pipe tripping operations took place for ~7 h. The tool string was recovered and retrieved from the bottommost sub of the BHA. Results showed that three FMS arms were significantly damaged, and the tool string was held inside the pipe by the mangled arms and springs protruding through the BHA holes for the MBR.

Interpretation of downhole acceleration, tool speed, tension, downhole force, FMS button responses, and caliper measurements suggest that the tool string experienced downward motion during Pass 1 and that the C1 FMS caliper arms suddenly closed partially before fully opening once again. A closer examination of the lowermost part of the damaged FMS tool showed that the inner and outer linkages, concentric shafts that give uphole readings of the caliper status, were damaged. This suggests that the trunion that allows the arms to operate was not making contact with at least two of the arms. This would cause the arms to remain open, whereas the movement on the linkages would suggest that they were operating normally. Therefore, the FMS caliper arms most likely opened as soon as the hole was reentered and were severely damaged, possibly flipping backward, when holding the weight of the entire tool string in a narrower part of the hole.

## Data processing

Logging data were recorded onboard the *JOIDES Resolution* by Schlumberger and archived in digital log information standard (DLIS) format. Data were sent by satellite transfer to the Lamont-Doherty Earth Observatory-Borehole Research Group, processed there, and transferred back to the ship for archiving in the shipboard database. Processing and data quality notes are given below.

### Depth shifting

In general, depth shifts are applied to logging data by selecting a reference (base) log (usually the total gamma ray log from the run with the greatest vertical extent and no sudden changes in cable speed), and features in equivalent logs from other passes are aligned by eye. The downhole logs were first shifted to the seafloor based on the logger's seafloor depth of 3267 m wireline depth below rig floor. This depth differs 8 m from the drillers bottom-felt depth. The depth-shifted logs were then depth matched to those of HNGS-HLDS-DITE tool string Pass 2 (Table **T10**).

### Data quality

The quality of wireline logging data were assessed by evaluating whether logged values are reasonable for the lithologies encountered and by checking consistency between different passes of the same tool. Gamma ray logs recorded through the BHA should be used only qualitatively because of the attenuation of the incoming signal. The thick-walled BHA attenuates the signal more than the thinner walled drill pipe. PEF measurements are strongly affected by the use of heavier mud.

A wide (>30.5 cm) and/or irregular borehole affects most recordings, particularly those like the HLDS that require eccentralization and good contact with the borehole wall. The density log roughly correlates with the resistivity logs, but it is largely affected by the hole conditions. The hole diameter measurements recorded with the hydraulic caliper on the HLDS (LCAL) show a very irregular borehole. Good repeatability was observed between Pass 1 and Pass 2, particularly for measurements of electrical resistivity, gamma ray, and density.

The DSI was operated in P&S monopole and upper dipole modes for both downlog and Pass 1 (all with standard frequency). The slowness data from delta-time compressional (DTCO) and delta-time shear upper dipole logs (DT2) are generally of good quality for these passes and thus were converted to acoustic velocities (VCO and VS2, respectively). Reprocessing of the original sonic waveforms, to be performed at a later date, is highly recommended to obtain more reliable velocity results.

The FMS images are generally of good quality below 151 m WMSF because of the relatively good hole condition (hole size < 35.6 cm) and of intermediate quality above 151 m WMSF because of the large borehole size (26–41 cm). The irregular and possibly elliptical shape of the borehole occasionally prevented some FMS pads from directly contacting the formation, resulting in poor-resolution or dark images. Hence, the FMS images (and the high-resolution resistivity logs) should be used with caution in this depth interval.

## Preliminary results

### Electrical resistivity measurements

Three electrical resistivity curves were obtained with the DITE. The spherically focused resistivity (SFLU), medium induction phasor-processed resistivity (IMPH), and deep induction phasor-processed resistivity (IDPH) profiles represent different depths of investigation into the formation (64, 76, and 152 cm, respectively) and different vertical resolutions (76, 152, and 213 cm, respectively). Downhole electrical resistivity measurements covered 225.4 m of the open hole sedimentary and volcaniclastic lithostratigraphic sequences drilled in Hole U1348A (Fig. **F28**). The DITE was the only tool that reached the bottom of the logged interval in Hole U1348A because it was the bottommost tool in the logging tool string (Fig. **F28**).

In the upper 99 m of the logged interval the IMPH values range from 1 to 5.8 Ωm, the IDPH values range from 1.0 to 4.7 Ωm, and the SFLU values range from 0.6 to 7.8 Ωm. In the volcaniclastic stratigraphic units (III–VI) the IMPH measurements range from 1.3 to 24.8 Ωm, the IDPH values range from 1.3 to 21.7 Ωm, and the SFLU values range from 0.8 to 14.6 Ωm (Fig. **F28**).

### Gamma ray measurements

Standard, computed, and individual spectral contributions from $^{40}$K, $^{238}$U, and $^{232}$Th were part of the gamma ray measurements obtained in Hole U1348A with the HNGS. The total gamma ray measurements through the BHA show one anomaly (logging Unit Ip), a peak between 93.2 and 93.7 m WMSF (Fig. **F28**).

Downhole gamma ray measurements in open hole covered 99 m of the bottommost sedimentary sequences (logging Units Is–Vs) and 109 m of the volcaniclastic units (logging Units Iv–IXv). Total gamma ray measurements in the bottommost sediments of

Hole U1348A are moderately variable, ranging from 0.8 to 58.8 gAPI with a mean of 8.2 gAPI. Potassium values are relatively low, with values between 0 and 2.4 wt% and a mean of 0.14 wt% (Fig. F29). Uranium values are mostly between 0 and 4.9 ppm, with a mean of 0.4 ppm. Thorium values range from 0.14 to 4.1 ppm, with a mean of 0.7 ppm.

Total gamma ray measurements in the volcaniclastic units (IIIv–VIv) are higher than the overlying sediments units (Is–IIs), with values between 9.2 and 65.4 gAPI (Fig. F28). Potassium values are relatively high in the volcaniclastics, with values between 0.12 and 2.6 wt% (Fig. F29). Uranium values are mostly between 0.0 and 3.2 ppm (Fig. F29). Thorium ranges from 0.0 to 2.8 ppm, with a mean of 0.7 ppm (Fig. F29).

### Density measurements

Density values range from 1.2 to 2.8 g/cm$^3$ over the sediment section of the open hole (Fig. F30). In the volcaniclastic section, density values are between 1.7 and 2.5 g/cm$^3$. A comparison between discrete physical property sample results and the downhole density log shows that discrete sample data (MAD) are consistent with the downhole data (Fig. F30).

### Sonic velocity measurements

Downhole velocity data were obtained for the open hole interval between 101 and 308.9 m WMSF (Fig. F30). In the upper sediment section (stratigraphic Units I and II), velocity is highly variable, averaging ~2.5 km/s. In the volcaniclastic section velocities are even more variable, between 1.8 and 6.4 km/s. A comparison with discrete sample measurements of *P*-wave velocity shows that the core data are consistent with the downhole measurements (Fig. F30).

### Magnetic field measurements

Measurements of total magnetic moment, magnetic inclination, magnetic intensity, and hole deviation were obtained with the GPIT (Fig. F56). The mean magnetic inclination and total magnetic moment from 101 to 328 m WMSF are 49° and 0.43 Oe, respectively. The magnetic intensity is 0.32 Oe on the *z*-axis and varies between –0.27 and 0.30 Oe on the *x*- and *y*-axes.

### Formation MicroScanner images

FMS images were obtained for the open hole interval between 105 and 328 m WMSF. The diameter of hole from the FMS calipers varied between 20 and 40 cm. High-quality FMS images were obtained in sections of the hole with a diameter <35.6 cm. FMS images from the sediment section show numerous bright, highly resistive layers throughout the unit that are most likely chert layers. FMS images from the volcaniclastic section show sections with subhorizontal contacts, moderately dipping layers, and vesicular or brecciated textures (Fig. F57). Preliminary structural analysis of the lower borehole intervals shows dipping contacts striking northeast to southwest with southeast-oriented dips ranging from 25° to 30° in magnitude that correlate to structures observed in the cores recovered from Hole U1348A (Fig. F58).

## Lithostratigraphic correlations

Preliminary interpretation of the downhole log data divided Hole U1348A into 15 logging units within 3 main sections, the section covered by the BHA, the sedimentary sequences in open hole, and the volcaniclastic sequences (Figs. F28, F29, F30). Logging units in the section covered or partially influenced by the BHA were interpreted on the basis of the gamma ray downhole logs, and only intervals that showed significant anomalies were characterized as logging units. Logging units within the open hole section that contained sedimentary sequences were also interpreted on the basis of the gamma ray fluctuations, whereas the volcaniclastic sequence was characterized using both the gamma ray and resistivity logs.

One logging unit was qualitatively identified in the section covered by the BHA (Fig. F28):

- Logging Unit Ip (93.1–97.7 m WMSF) is characterized by a significant increase in gamma ray measurements. A large contribution from thorium is apparent in the spectral gamma ray measurements (Figs. F28, F29).

Five logging units were identified in the upper sedimentary sequence (stratigraphic Units I and II) in the open hole below the BHA based on gamma ray downhole logs (Fig. F28):

- Logging Unit Is (101.1 to 165.7 m WMSF) is characterized by gradual increases in resistivity and gamma ray measurements. At the base of this unit, both resistivity and gamma ray values decrease slightly.
- Logging Unit IIs (165.7–170.4 m WMSF) is defined by a sharp increase in total gamma ray measurements that is mostly associated with an increase in uranium (Fig. F29).
- Logging Unit IIIs (170.4–187.4 m WMSF) is defined by a decrease in gamma ray values with respect to Unit IIs. Gamma ray and resistivity measurements show small variations within this unit, but overall the values are fairly consistent (Fig. F29).

- Logging Unit IVs (187.4–193.5 m WMSF) is characterized by a sharp increase in gamma ray measurements and a decrease in resistivity (Fig. F28). The gamma ray anomaly is mostly caused by high contributions from thorium and potassium (Fig. F29).
- Logging Unit Vs (193.5 to 204.3 m WMSF) is defined by a decrease in gamma ray measurements with respect to Unit IVs. The gamma ray values are consistent throughout the unit. Electrical resistivity measurements show an increase at the top of the unit, followed by a decrease in values in the lowermost part of the unit.

The volcaniclastic sequence below 154.93 m WMSF is divided into nine logging units using the downhole resistivity and natural gamma logs (Fig. F28):

- Logging Unit Iv (204.3–210.5 m WMSF) is defined by an increase in resistivity to a maximum value of ~25 Ωm. Gamma ray measurements sharply decrease, whereas density and compressional wave velocities increase (Fig. F30).
- Logging Unit IIv (210.5–214.6 m WMSF) is characterized by a sharp decrease in resistivity and a sharp increase in gamma radiation. Spectral gamma ray measurements indicate contributions from thorium, uranium, and potassium (Fig. F29). Decreases in both density and compressional wave velocity also define this unit (Fig. F30).
- Logging Unit IIIv (214.6–245.8 m WMSF) has consistent resistivity and gamma ray values throughout the unit. Gamma ray values are mostly controlled by potassium, which averages 1.29 wt% throughout the interval (Fig. F29).
- Logging Unit IVv (245.8–260.1 m WMSF) is defined by sharply increasing resistivity values (Fig. F28). Total gamma ray, potassium, and compressional wave velocity also decrease.
- Logging Unit Vv (260.1–267.5 m WMSF) is characterized by sharply increasing resistivity and gamma ray values. Potassium increases, whereas uranium and thorium have low values. Density decreases through the unit, whereas compressional wave velocities are higher than in the surrounding units.
- Logging Unit VIv (267.5–273.0 m WMSF) is characterized by low resistivity values and a large peak in gamma radiation. Spectral gamma ray measurements indicate a large contribution from uranium in this unit, with lower contributions from thorium and potassium. Bulk density and compressional wave velocity are low throughout the interval.
- Logging Unit VIIv (273.0–287.2 m WMSF) is defined by sharply increasing resistivity values in the upper part of the unit. NGR decreases sharply at the top of the unit and then increases in the lower part of the unit (Fig. F28).
- Logging Unit VIIIv (287.2–291.3 m WMSF) is defined by sharply increasing resistivity values, whereas natural gamma ray values decrease. Spectral gamma ray data indicate that potassium, thorium, and uranium are low (Fig. F29). Density and compressional wave values increase sharply at the top of the unit.
- Logging Unit IXv (291.3–326.6 m WMSF) is characterized by lower resistivity values than the overlying unit, and clear cycles are present within the unit. NGR data only partially cover the unit and values decrease sharply at the top of the unit and then increase slowly (Fig. F28). Potassium, thorium, and uranium values are low, as are density and compressional wave velocity.

# References


Ando, A., Huber, B.T., MacLeod, K.G., Ohta, T., and Khim, B.-K., 2009a. Blake Nose stable isotopic evidence against the mid-Cenomanian glaciation hypothesis. *Geology,* 37(5):451–454. **doi:10.1130/G25580A.1**

Ando, A., Kaiho, K., Kawahata, H., and Kakegawa, T., 2008. Timing and magnitude of early Aptian extreme warming: unraveling primary $\delta^{18}O$ variation in indurated pelagic carbonates at Deep Sea Drilling Project Site 463, central Pacific Ocean. *Palaeogeogr., Palaeoclimatol., Palaeoecol.,* 260(3–4):463–476. **doi:10.1016/j.palaeo.2007.12.007**

Ando, A., Nakano, T., Kaiho, K., Kobayashi, T., Kokado, E., and Khim, B.-K., 2009b. Onset of seawater $^{87}Sr/^{86}Sr$ excursion prior to Cenomanian–Turonian Oceanic Anoxic Event 2? New Late Cretaceous strontium isotope curve from the central Pacific Ocean. *J. Foraminiferal Res.,* 39(4):322–334. **doi:10.2113/gsjfr.39.4.322**

Bach, W., Hegner, E., Erzinger, J., and Satir, M., 1994. Chemical and isotopic variations along the superfast spreading East Pacific Rise from 6 to 30°S. *Contrib. Mineral. Petrol.*, 116(4):365–380. **doi:10.1007/BF00310905**

Bellier, J.-P., and Moullade, M., 2002. Lower Cretaceous planktonic foraminiferal biostratigraphy of the western North Atlantic (ODP Leg 171B), and taxonomic clarification of key index species. *Rev. Micropaleontol.,* 45(1):9–26. **doi:10.1016/S0035-1598(02)80003-4**

Boudagher-Fadel, M.K., Banner, F.T., and Whittaker, J.E., 1997. *The Early Evolutionary History of Planktonic Foraminifers:* London (Chapman and Hall).

Bouma, A.H., 1962. *Sedimentology of Some Flysch Deposits: A Graphic Approach to Facies Interpretation:* Amsterdam (Elsevier).

Bukry, D., 1981. Synthesis of silicoflagellate stratigraphy for Maestrichtian to Quaternary marine sediments. *In* Warme, T.E., Douglas, R.C., and Winterer, E.L. (Eds.), *The Deep Sea Drilling Project: A Decade of Progress*. Spec. Publ.—Soc. Econ. Paleontol. Mineral., 32:433–444.

Busby, C., Adams, B.F., Mattinson, J., and Deoreo, S., 2006. View of an intact oceanic arc, from surficial to mesozonal levels: Cretaceous Alisitos arc, Baja California. *J. Volcanol. Geotherm. Res.,* 149(1–2):1–46. **doi:10.1016/j.jvolgeores.2005.06.009**

Cann, J.R., 1970. Rb, Sr, Y, Zr, and Nb in some ocean floor basaltic rocks. *Earth Planet. Sci. Lett.,* 10(1):7–11. **doi:10.1016/0012-821X(70)90058-0**

Carlisle, D., 1963. Pillow breccias and their aquagene tuffs, Quadra Island, British Columbia. *J. Geol.,* 71(1):48–71. **doi:10.1086/626875**

Clague, D.A., Paduan, J.B., and Davis, A.S., 2009. Widespread strombolian eruptions of mid-ocean ridge basalt. *J. Volcanol. Geotherm. Res.,* 180(2–4):171–188. **doi:10.1016/j.jvolgeores.2008.08.007**

Fisher, R.V., and Schmincke, H.-U., 1984. *Pyroclastic Rocks:* New York (Springer-Verlag).

Fiske, R.S., 1963. Subaqueous pyroclastic flows in the Ohanapecosh Formation, Washington. *Geol. Soc. Am. Bull.,* 74(4):391–406. **doi:10.1130/0016-7606(1963)74[391:SPFITO]2.0.CO;2**

Fiske, R.S., and Matsuda, T., 1964. Submarine equivalents of ash flows in the Tokiwa Formation, Japan. *Am. J. Sci.,* 262:76–106.

Fitton, J.G., and Godard, M., 2004. Origin and evolution of magmas on the Ontong Java Plateau. *In* Fitton, J.G., Mahoney, J.J., Wallace, P.J., and Saunders, A.D. (Eds.), *Origin and Evolution of the Ontong Java Plateau.* Geol. Soc. Spec. Publ., 229(1):151–178. **doi:10.1144/GSL.SP.2004.229.01.10**

Fontilea, K., Marsaglia, K.M., and Dean, N., 2006. A petrological and geochemical study of Cretaceous siliceous rocks from Shatsky Rise. *In* Bralower, T.J., Premoli Silva, I., and Malone, M.J. (Eds.), *Proc. ODP, Sci. Results,* 198: College Station, TX (Ocean Drilling Program), 1–45. **doi:10.2973/odp.proc.sr.198.107.2006**

Gibson, H.L., Morton, R.L., and Hudak, G.J., 2000. Submarine volcanic processes, deposits, and environments favorable for the location of volcanic-associated massive sulfide deposits. *In* Barrie, C.T., and Hannington, M.D. (Eds.), *Volcanic-Associated Massive Sulfide Deposits: Processes and Examples in Modern and Ancient Settings*. Rev. Econ. Geol., 8:13–51.

Heiken, G., and Wohletz, K., 1985. *Volcanic Ash:* Berkeley (Univ. of California Press).

Honnorez, J., and Kirst, P., 1975. Submarine basaltic volcanism: morphometric parameters for discriminating hyaloclastites from hyalotuffs. *Bull. Volcanol.,* 39(3):441–465. **doi:10.1007/BF02597266**

Holbourn, A., Kuhnt, W., and Soeding, E., 2001. Atlantic paleobathymetry, paleoproductivity and paleocirculation in the late Albian: the benthic foraminiferal record. *Palaeogeogr., Palaeoclimatol., Palaeoecol.,* 170(3–4):171–196. **doi:10.1016/S0031-0182(01)00223-1**

Humphris, S.E., and Thompson, G., 1978. Trace element mobility during hydrothermal alteration of oceanic basalts. *Geochim. Cosmochim. Acta,* 42(1):127–136. **doi:10.1016/0016-7037(78)90222-3**

Kirkpatrick, R.J., 1979. Processes of crystallization in pillow basalts, Hole 396B, DSDP Leg 46. *In* Dmitriev, L., Heirtzler, et al., 1979. *Init. Repts. DSDP,* 46: Washington, DC (U.S. Govt. Printing Office), 271–282. **doi:10.2973/dsdp.proc.46.117.1979**

Kirschvink, J.L., 1980. The least-squares line and plane and the analysis of palaeomagnetic data. *Geophys. J. R. Astron. Soc.,* 62(3):699–718. **doi:10.1111/j.1365-246X.1980.tb02601.x**

Klaus, A., and Sager, W.W., 2002. Data report: high-resolution site survey seismic reflection data for ODP Leg 198 drilling on Shatsky Rise, northwest Pacific. *In* Bralower, T.J., Premoli Silva, I., Malone, M.J., et al., *Proc. ODP, Init. Repts.,* 198: College Station, TX (Ocean Drilling Program), 1–21. **doi:10.2973/odp.proc.ir.198.111.2002**

Le Maitre, R.W., Bateman, P., Dudek, A., Keller, J., Lameyre, J., Le Bas, M.J., Sabine, P.A., Schmid, R., Sorensen, H., Streckeisen, A., Woolley, A.R., and Zanettin, B., 1989. *A Classification of Igneous Rocks and Glossary of Terms:* Oxford (Blackwell).

Lowe, D.R., 1979. Sediment gravity flows: their classification and some problems of application to natural flows and deposits. *In* Doyle, L.J., and Pilkey, O.H. (Eds.), *Geology of Continental Slopes*. Spec. Publ.—Soc. Econ. Paleontol. Mineral., 27:75–82.

Lowe, D.R., 1982. Sediment gravity flows, II. Depositional models with special reference to the deposits of high-density turbidity currents. *J. Sediment. Petrol.,* 52(1):279–297. **http://jsedres.sepmonline.org/cgi/content/abstract/52/1/279**

Macdonald, G.A., 1968. Composition and origin of Hawaiian lavas. *In* Coats, R.R., Hay, R.L., and Anderson, C.A. (Eds.), *Studies in Volcanology: A Memoir in Honor of Howel Williams*. Mem.—Geol. Soc. Am., 116:477–522.

Macdonald, G.A., and Katsura, T., 1964. Chemical composition of Hawaiian lavas. *J. Petrol.,* 5(1):82–133.

Mahoney, J.J., Duncan, R.A., Tejada, M.L.G., Sager, W.W., and Bralower, T.J., 2005. Jurassic–Cretaceous boundary age and mid-ocean-ridge–type mantle source for Shatsky Rise. *Geology,* 33(3):185–188. **doi:10.1130/G21378.1**

Mahoney, J.J., Fitton, J.G., Wallace, P.J., et al., 2001. *Proc. ODP, Init. Repts.,* 192: College Station, TX (Ocean Drilling Program). **doi:10.2973/odp.proc.ir.192.2001**

Mahoney, J.J., Sinton, J.M., Kurz, M.D., Macdougall, J.D., Spencer, K.J., and Lugmair, G.W., 1994. Isotope and trace element characteristics of a super-fast spreading ridge: East Pacific Rise 13–23°S. *Earth Planet. Sci. Lett.,* 121(1–2):173–193. **doi:10.1016/0012-821X(94)90039-6**

Moore, J.G., and Clague, D.A., 2002. Mapping the Nuuanu and Wailau landslides in Hawaii. *In* Takahashi, E., Lip-

man, P.W., Garcia, M.O., Naka, J., and Aramaki, S. (Eds.), *Hawaiian Volcanoes: Deep Underwater Perspectives*. Geophys. Monogr., 128:233–244.

Nakanishi, M., Sager, W.W., and Klaus, A., 1999. Magnetic lineations within Shatsky Rise, northwest Pacific Ocean: implications for hot spot–triple junction interaction and oceanic plateau formation. *J. Geophys. Res., [Solid Earth],* 104(B4):7539–7556. **doi:10.1029/1999JB900002**

Natland, J.H., and Mahoney, J.J., 1982. Alteration in igneous rocks at Deep Sea Drilling Project Sites 458 and 459, Mariana fore-arc region: relationship to basement structure. *In* Hussong, D.M., Uyeda, S., et al., *Init. Repts. DSDP,* 60: Washington, DC (U.S. Govt. Printing Office), 769–788. **doi:10.2973/dsdp.proc.60.145.1982**

Nyong, E.E., and Olsson, R.K., 1984. A paleoslope model of Campanian to lower Maestrichtian foraminifera in the North American Basin and adjacent continental margin. *Mar. Micropaleontol.,* 8(6):437–477. **doi:10.1016/0377-8398(84)90009-4**

Ogg, J.G., Ogg, G., and Gradstein, F.M., 2008. *The Concise Geologic Time Scale*: Cambridge (Cambridge Univ. Press). **http://www.cambridge.org/catalogue/catalogue.asp?isbn=9780521898492**

Patino, L.C., Velbel, M.A., Price, J.R., and Wade, J.A., 2003. Trace element mobility during spheroidal weathering of basalts and andesites in Hawaii and Guatemala. *Chem. Geol.,* 202(3–4):343–364. **doi:10.1016/j.chemgeo.2003.01.002**

Peacock, M.A., 1926. The petrology of Iceland, Part I. The basic tuffs. *Trans. R. Soc. Edinburgh,* 55:51–76.

Petrizzo, M.R., and Huber, B.T., 2006. On the phylogeny of the late Albian genus *Planomalina*. *J. Foraminiferal Res.,* 36(3):233–240. **doi:10.2113/gsjfr.36.3.233**

Ray, J.R., Mahoney, J.J., Duncan, R.A., Ray, J.S., Wessel, P., and Naar, D., submitted. Chronology and geochemistry of the Nazca Ridge and Easter Seamount Chain: a 30 m.y. hotspot record. *J. Petrol.*

Rittman, A., 1958. Il meccanismo di formazione delle lave a pillows e dei consideiti tuff palagonitici. *Att. Acad. Gioenia Sci. Nat. Catania,* 4:310–317.

Rittman, A., 1962. *Volcanoes and Their Activity:* New York (Interscience Publ.).

Sager, W.W., 2005. What built Shatsky Rise, a mantle plume or ridge tectonics? *In* Foulger, G.R., Natland, J.H., Presnall, D.C., and Anderson, D.L. (Eds.), *Plates, Plumes, and Paradigms*. Spec. Pap.—Geol. Soc. Am., 388:721–733. **doi:10.1130/0-8137-2388-4.721**

Sager, W.W., and Han, H.-C., 1993. Rapid formation of the Shatsky Rise oceanic plateau inferred from its magnetic anomaly. *Nature (London, U. K.),* 364(6438):610–613. **doi:10.1038/364610a0**

Sager, W.W., Kim, J., Klaus, A., Nakanishi, M., and Khankishieva, L.M., 1999. Bathymetry of Shatsky Rise, northwest Pacific Ocean: implications for ocean plateau development at a triple junction. *J. Geophys. Res., [Solid Earth],* 104(4):7557–7576. **doi:10.1029/1998JB900009**

Shafer, J.T., Neal, C.R., and Castillo, P.R., 2004. Compositional variability in lavas from the Ontong Java Plateau: results from basalt clasts within the volcaniclastic succession at Ocean Drilling Program Leg 192 Site 1184. *In* Fitton, J.G., Mahoney, J.J., Wallace, P.J., and Saunders, A.D. (Eds.), *Origin and Evolution of the Ontong Java Plateau.* Geol. Soc. Spec. Publ., 229(1):333–351. **doi:10.1144/GSL.SP.2004.229.01.19**

Shipboard Scientific Party, 2002a. Explanatory notes. *In* Bralower, T.J., Premoli Silva, I., Malone, M.J., et al., *Proc. ODP, Init. Repts.,* 198: College Station, TX (Ocean Drilling Program), 1–63. **doi:10.2973/odp.proc.ir.198.102.2002**

Shipboard Scientific Party, 2002b. Site 1213. *In* Bralower, T.J., Premoli Silva, I., Malone, M.J., et al., *Proc. ODP, Init. Repts.,* 198: College Station, TX (Ocean Drilling Program), 1–110. **doi:10.2973/odp.proc.ir.198.109.2002**

Sikora, P.J., and Olsson, R.K., 1991. A paleoslope model of late Albian to early Turonian foraminifera of the west Atlantic margin and North Atlantic Basin. *Mar. Micropaleontol.,* 8(1–2):25–72. **doi:10.1016/0377-8398(91)90005-Q**

Sinton, J.M., Smaglik, S.M., Mahoney, J.J., and Macdonald, K.C., 1991. Magmatic processes at superfast spreading mid-ocean ridges: glass compositional variations along the East Pacific Rise 13°–23°S. *J. Geophys. Res., [Solid Earth],* 96:6133–6155. **doi:10.1029/90JB02454**

Sliter, W.V., 1977. Cretaceous benthic foraminifers from the western South Atlantic Leg 39, Deep Sea Drilling Project. *In* Supko, P.R., Perch-Nielsen, K., et al., *Init. Repts. DSDP,* 39: Washington, DC (U.S. Govt. Printing Office), 657–697. **doi:10.2973/dsdp.proc.39.130.1977**

Sliter, W.V., and Baker, R.A., 1972. Cretaceous bathymetric distribution of benthic foraminifers. *J. Foraminiferal Res.,* 2(4):167–183. **doi:10.2113/gsjfr.2.4.167**

Smith, W.H.F., and Sandwell, D.T., 1997. Global sea floor topography from satellite altimetry and ship depth soundings. *Science,* 277(5334):1956–1962. **doi:10.1126/science.277.5334.1956**

Stephen, R.A., Kasahara, J., Acton, G.D., et al., 2003. *Proc. ODP, Init. Repts.,* 200: College Station, TX (Ocean Drilling Program). **doi:10.2973/odp.proc.ir.200.2003**

Stow, D.A.V., 1986. Deep clastic seas. *In* Reading, H.G. (Ed.), *Sedimentary Environments and Facies:* London (Blackwell Sci. Publ.), 399–446.

Tejada, M.L.G., Mahoney, J.J., Duncan, R.A., and Hawkins, M.P., 1996. Age and geochemistry of basement and alkalic rocks of Malaita and Santa Isabel, Solomon Islands, southern margin of Ontong Java Plateau. *J. Petrol.* 37(2):361–394. **doi:10.1093/petrology/37.2.361**

Tejada, M.L.G., Mahoney, J.J., Neal, C.R., Duncan, R.A., and Petterson, M.G., 2002. Basement geochemistry and geochronology of Central Malaita, Solomon Islands, with implications for the origin and evolution of the Ontong Java Plateau. *J. Petrol.,* 43(3):449–484. **doi:10.1093/petrology/43.3.449**

Verga, D., and Premoli Silva, I., 2003a. Early Cretaceous planktonic foraminifera from the Tethys: the large, many-chambered representatives of the genus *Globigerinelloides*. *Cretaceous Res.,* 24(6):661–690. **doi:10.1016/j.cretres.2003.07.007**

Verga, D., and Premoli Silva, I., 2003b. Early Cretaceous planktonic foraminifera from the Tethys: the small, few-chambered representatives of the genus *Globigerinelloides*. *Cretaceous Res.,* 24(3):305–334. **doi:10.1016/S0195-6671(03)00045-4**

Verga, D., and Premoli Silva, I., 2005. Early Cretaceous planktonic foraminifera from the Tethys: the upper Aptian, planispiral morphotypes with elongate chambers. *Cretaceous Res.,* 26(2):239–259. **doi:10.1016/j.cretres.2005.01.004**

Widmark, J.G.V., 1997. Deep-sea benthic foraminifera from Cretaceous–Tertiary boundary strata in the South Atlantic Ocean: taxonomy and paleoecology. *Fossils Strata,* 43:1–94.

Yamagishi, H., 1987. Studies on the Neogene subaqueous lavas and hyaloclastites in southwest Hokkaido. *Rept. Geol. Surv. Hokkaido,* 59:55–117.

**Publication:** 3 November 2010
**MS 324-105**

**Figure F1.** Bathymetry of Tamu Massif and location of Sites U1347 and U1348. Contours and colors indicate bathymetric depths predicted by satellite altimetry (Smith and Sandwell, 1997). Contours shown at 200 m intervals; dark contours shown for kilometer multiples. Red line = track of Cruise TN037 site survey (Klaus and Sager, 2002), open circles = prior drill sites, blue circle = location of Site 1213.

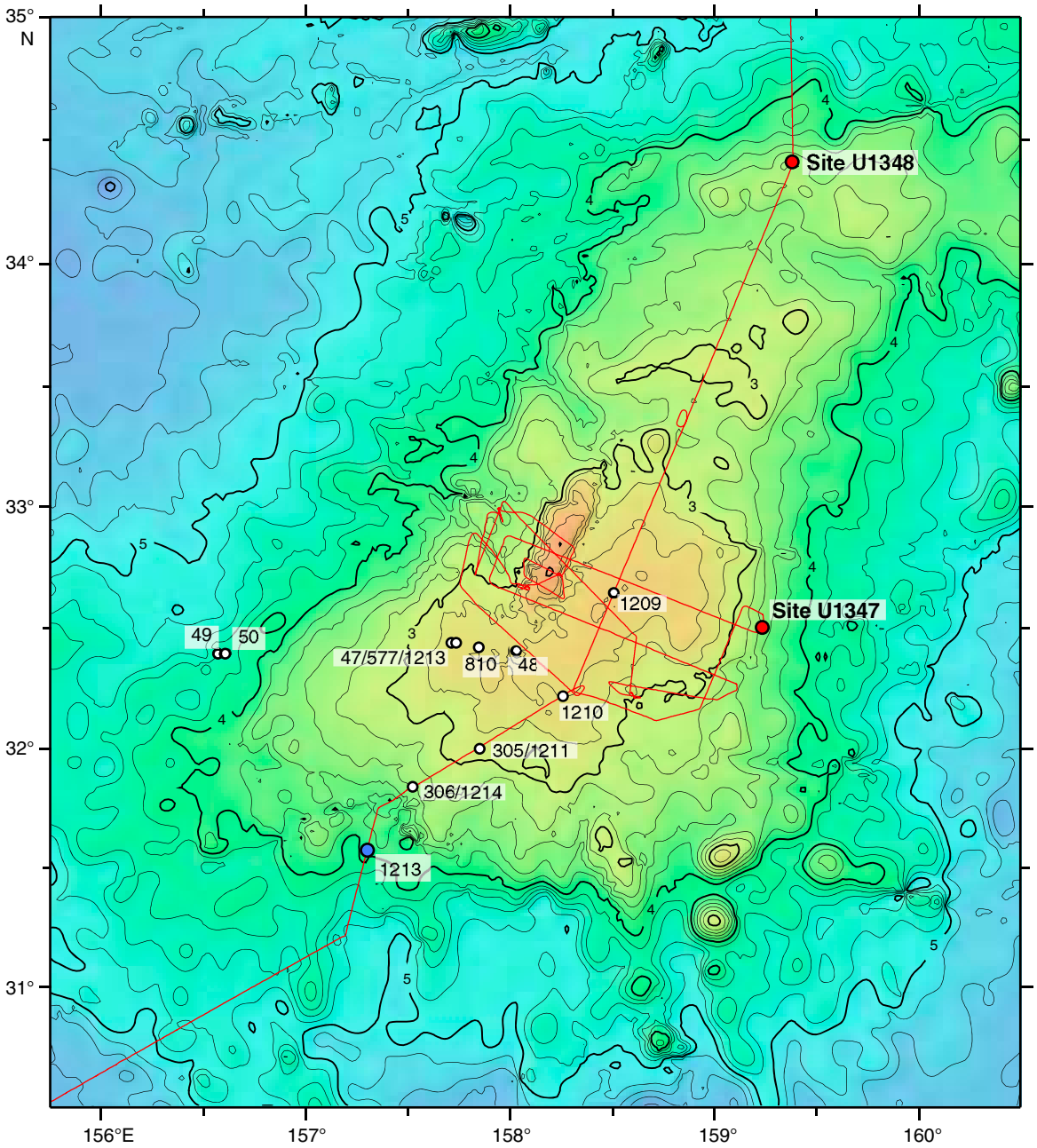

**Figure F2.** Seismic section and precruise layer interpretation (color overlay), Site U1348. See Klaus and Sager (2002). UTC = Universal Time Coordinated.

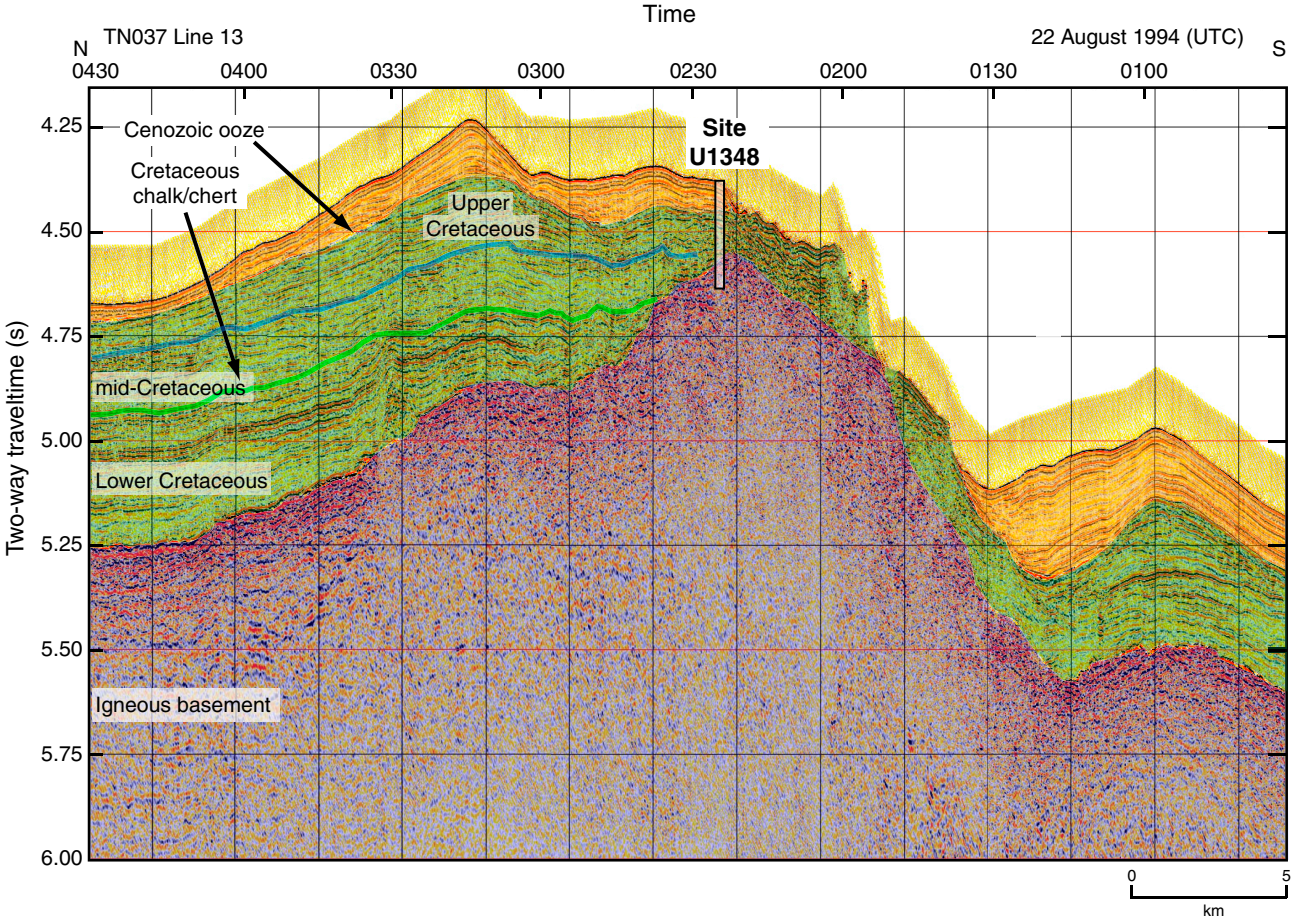

**Figure F3.** Close-up of seismic section and precruise layer interpretation (color overlay), Site U1348. See Klaus and Sager (2002). UTC = Universal Time Coordinated.

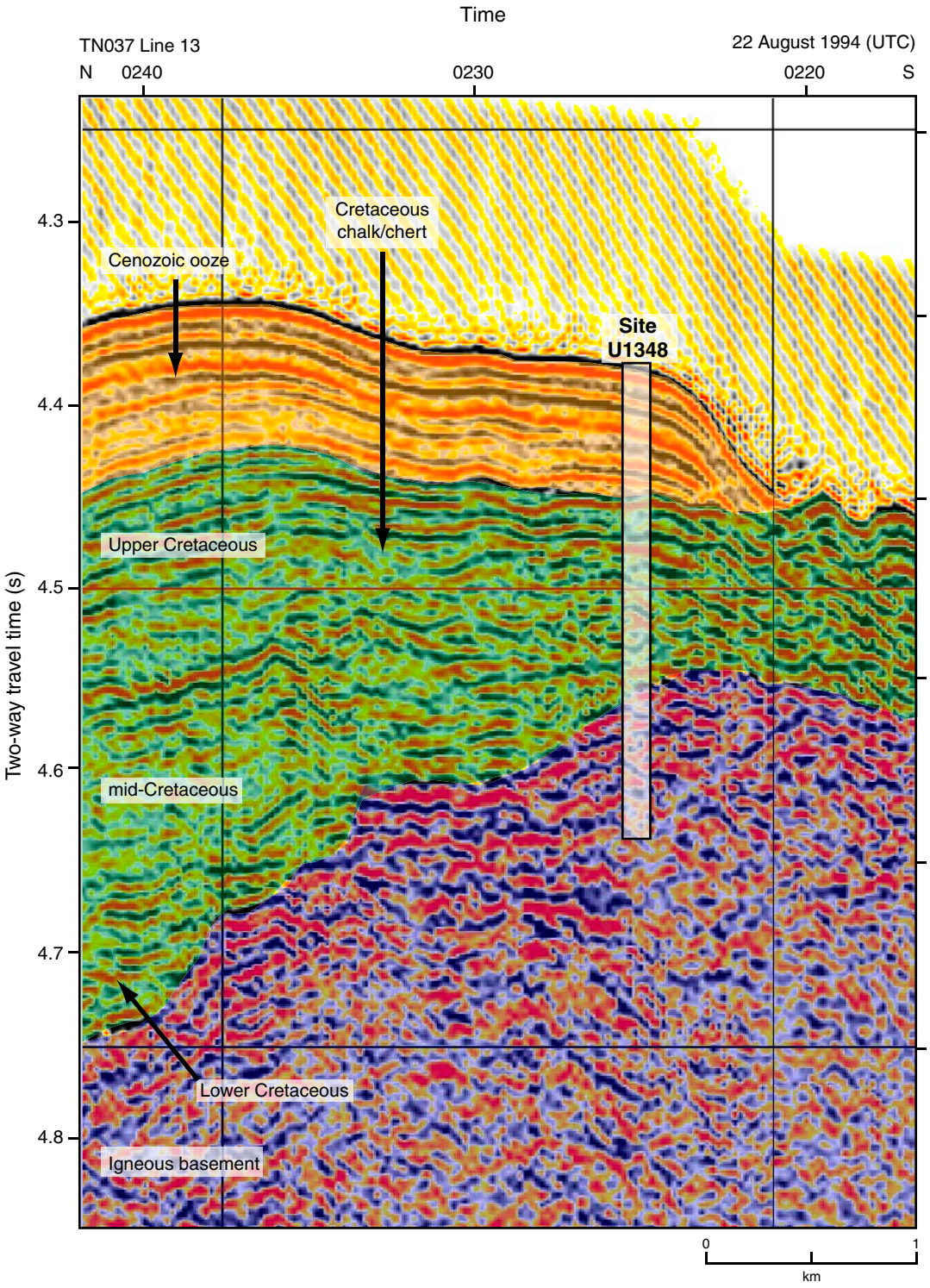

**Figure F4.** Plot of operation time vs. penetration depth, Hole U1348A. Dashed line = planned penetration progress, solid blue line = actual depth achieved. DWKS = Drawworks, FMS = Formation MicroScanner.

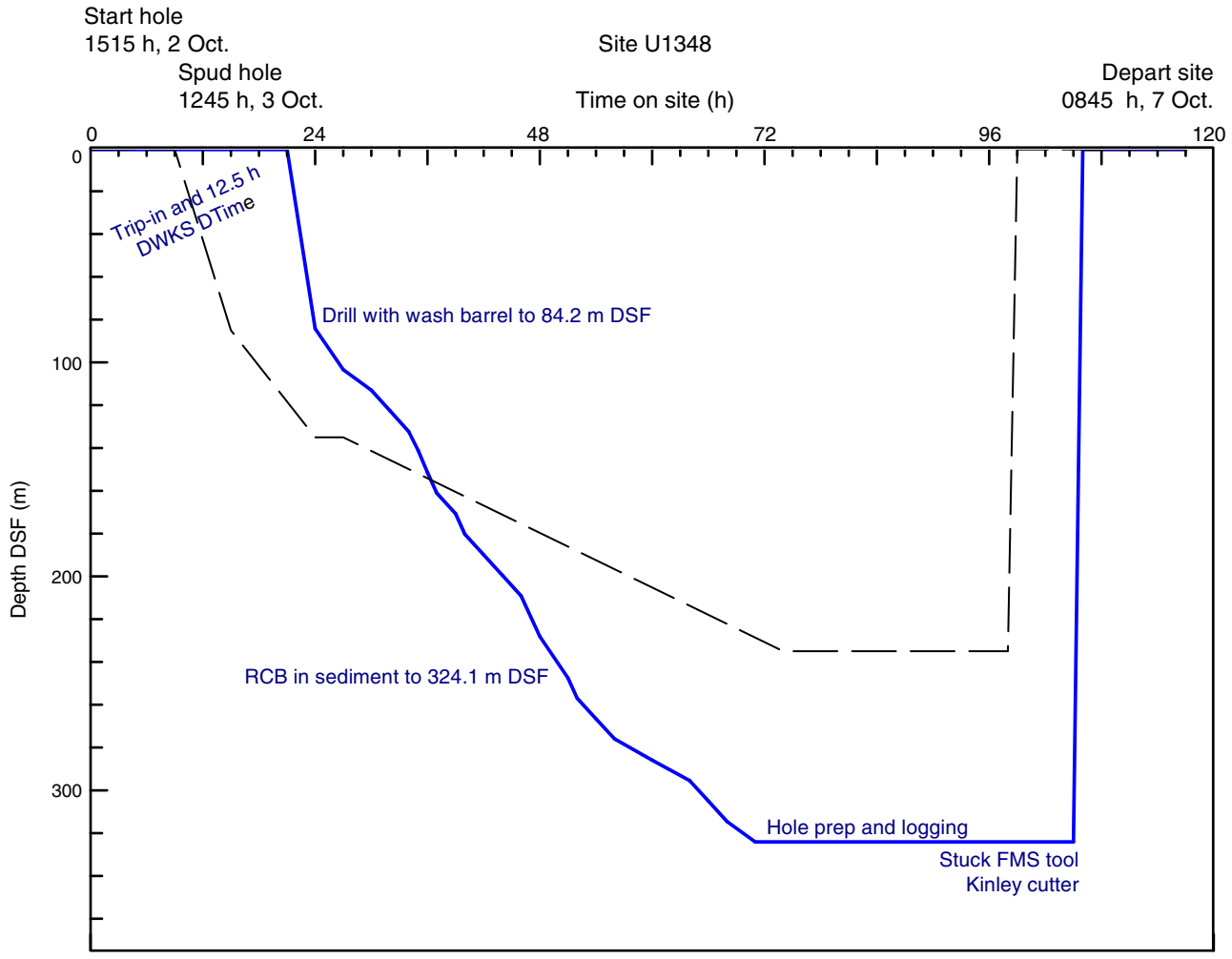

**Figure F5.** Lithostratigraphy, Site U1348.

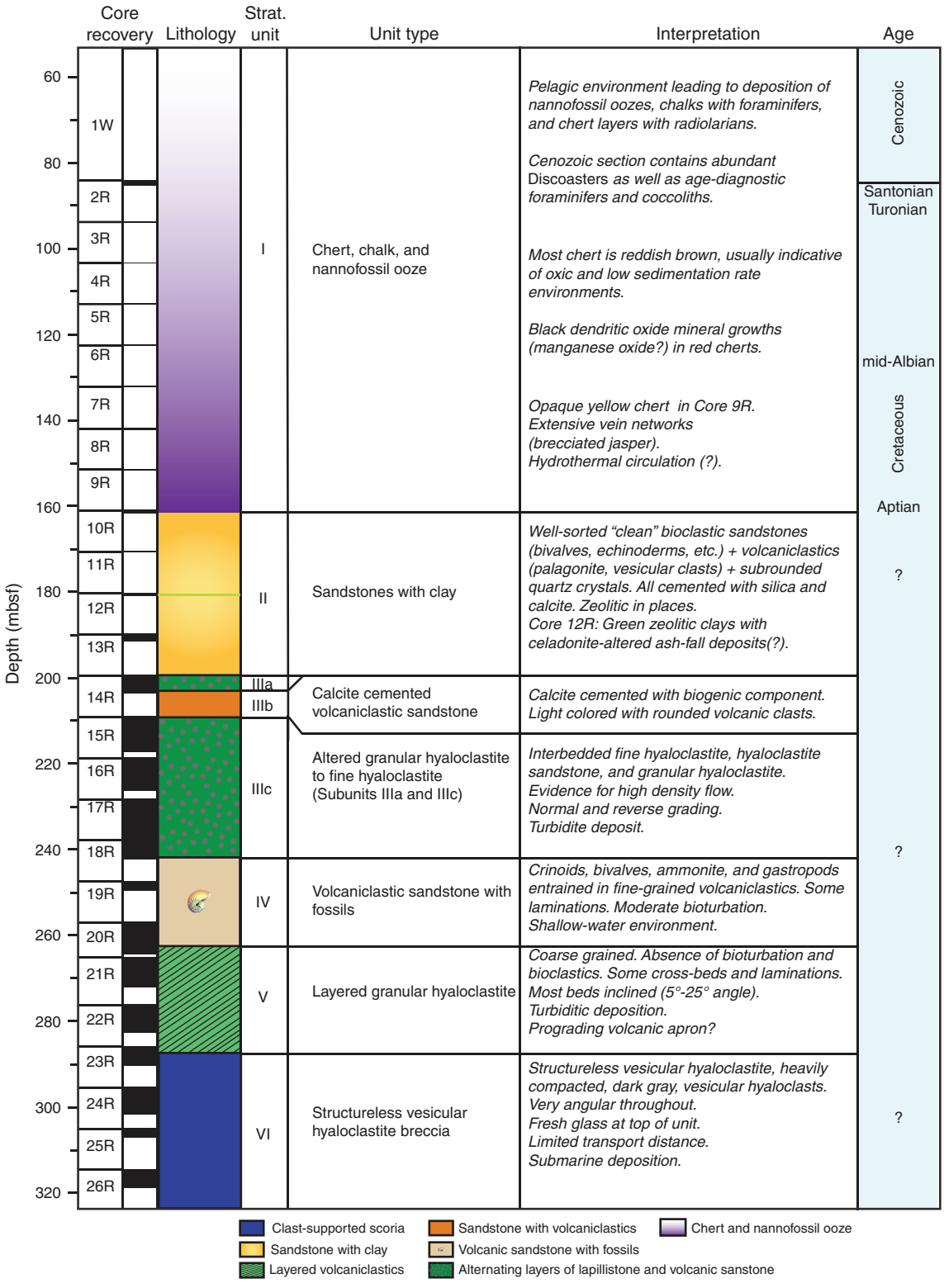

**Figure F6.** Photographs of cherts and porcellanite, Hole U1348A. **A.** Reddish brown chert with whitish pink porcellanite streaks and inclusions. **B.** Pinkish red chert with whitish pink porcellanite streaks bisected by a prominent siliceous vein. **C, D.** Black dendritic mineral growths (C) within red chert and (D) along a siliceous vein. **E.** Circular porcellanite radiolarian "ghosts" adjacent to a large pale porcellanite patch (replaced burrow?).

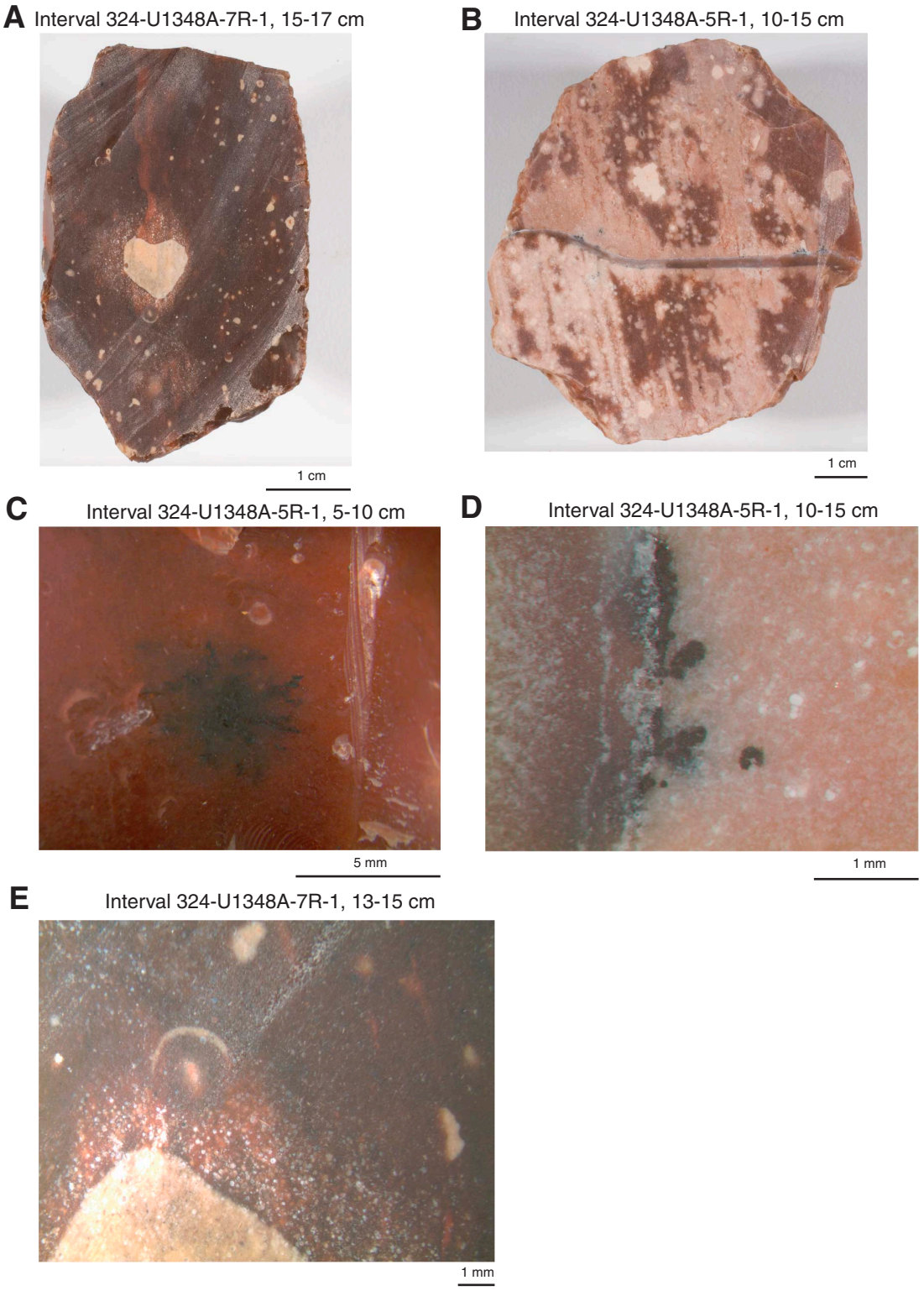

**Figure F7.** Core photograph of soupy nannofossil ooze, Hole U1348A. Contact between the light gray (mid-Cenozoic) and pale yellow (Late Cretaceous) ooze is indistinct and could represent drilling disturbance or a genuine unconformity.

**Figure F8.** Photograph of yellow brecciated chert (jasper) recemented by clear silica, Hole U1348A.

**Figure F9. A.** Photograph of a portion of stratigraphic Unit II in Hole U1348A that contains structureless, predominantly altered, quartz-cemented dark yellow sandstone with light gray streaks of chert and a few altered volcanic clasts. **B, C.** Thin section photomicrographs of quartz cement under (B) plane-polarized light and (C) cross-polarized light.

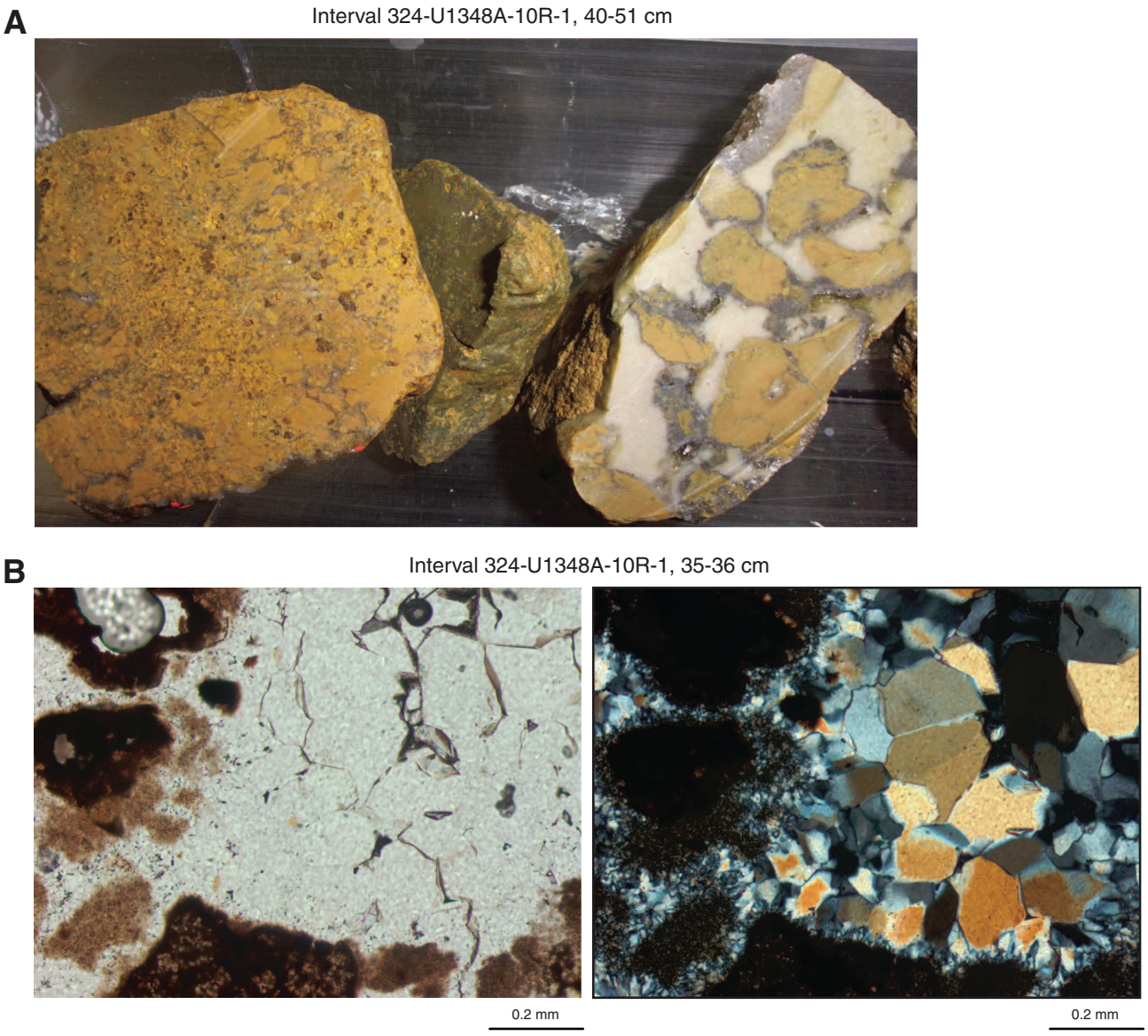

**Figure F10. A.** Photograph of bright yellow nuggets of coarse biogenic sandstone, Hole U1348A. **B.** Photograph of rounded, oblong coral fragment (~1–2 mm), which is the main component of the sandstone in this interval. Striated outer surface of the coral is visible.

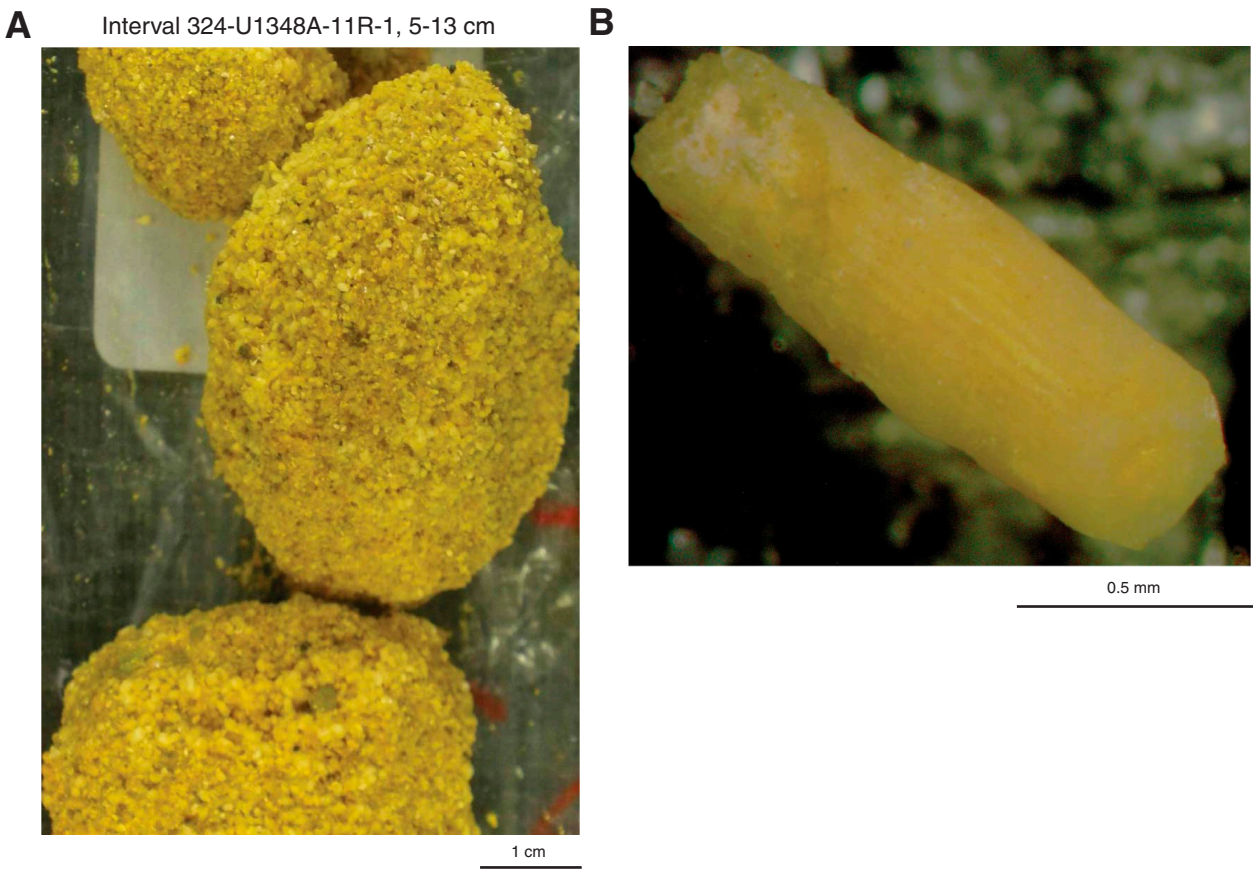

**Figure F11.** Core photographs of (**A**) light greenish yellow sediments composed of zeolites and (**B**) greenish celadonite-rich interval, Hole U1348A.

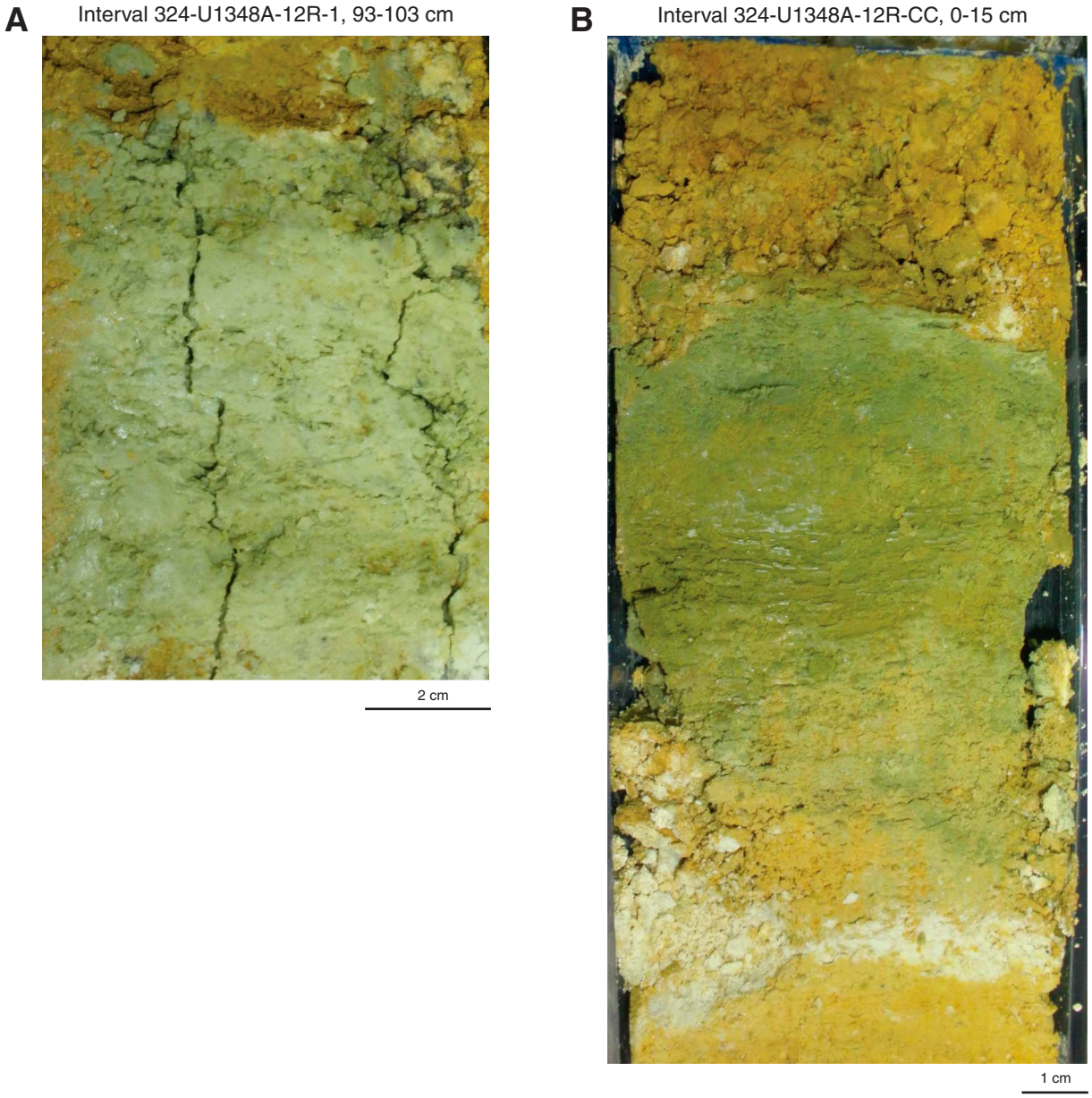

**Figure F12.** Thin section photomicrographs, Hole U1348A. **A, B, C, D.** Biogenic components under (A, C) plane-polarized light and (B, D) cross-polarized light. **E, F.** Altered, broken feldspar lath under (E) plane-polarized light and (F) cross-polarized light.

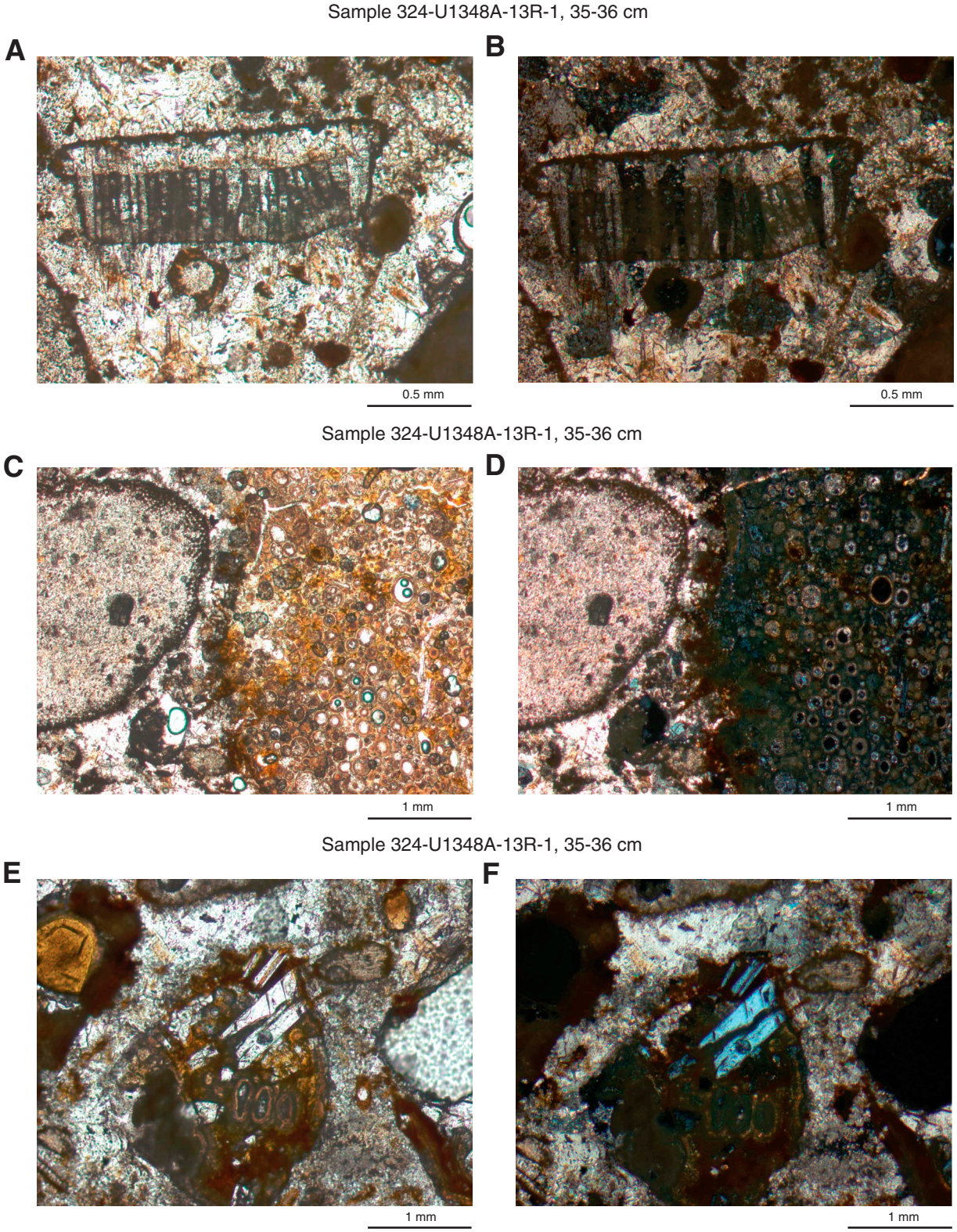

**Figure F13. A.** Core photograph of a portion of stratigraphic Subunit IIIa with structureless bedding. A very large, angular, aphyric clast is in the center of the image within a finer hyaloclastic matrix. Some of the constituent volcanic clasts are angular, whereas others have a more rounded shape. **B.** Core photograph of a portion of Subunit IIIb in Hole U1348A showing a greater proportion of carbonate relative to volcaniclastics. Volcanic constituents are smaller and much more rounded than those in Subunits IIIa or IIIc. Bioclastic elements such as bivalves are also present in this subunit.

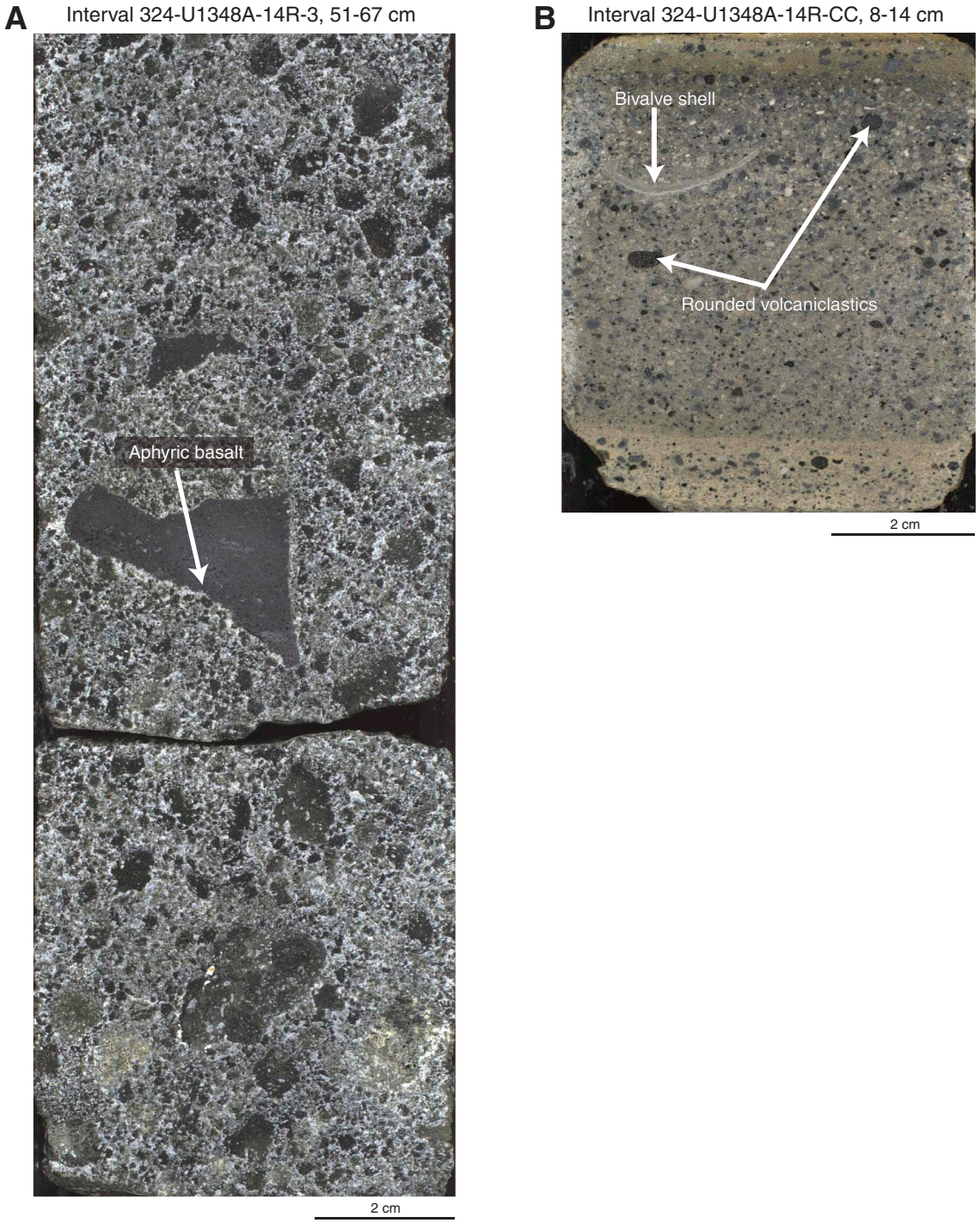

**Figure F14.** Core photographs of typical clast-rich nature of stratigraphic Subunits IIIa and IIIc, Hole U1348A (interval 324-U1348A-15R-2, 95–115 cm).

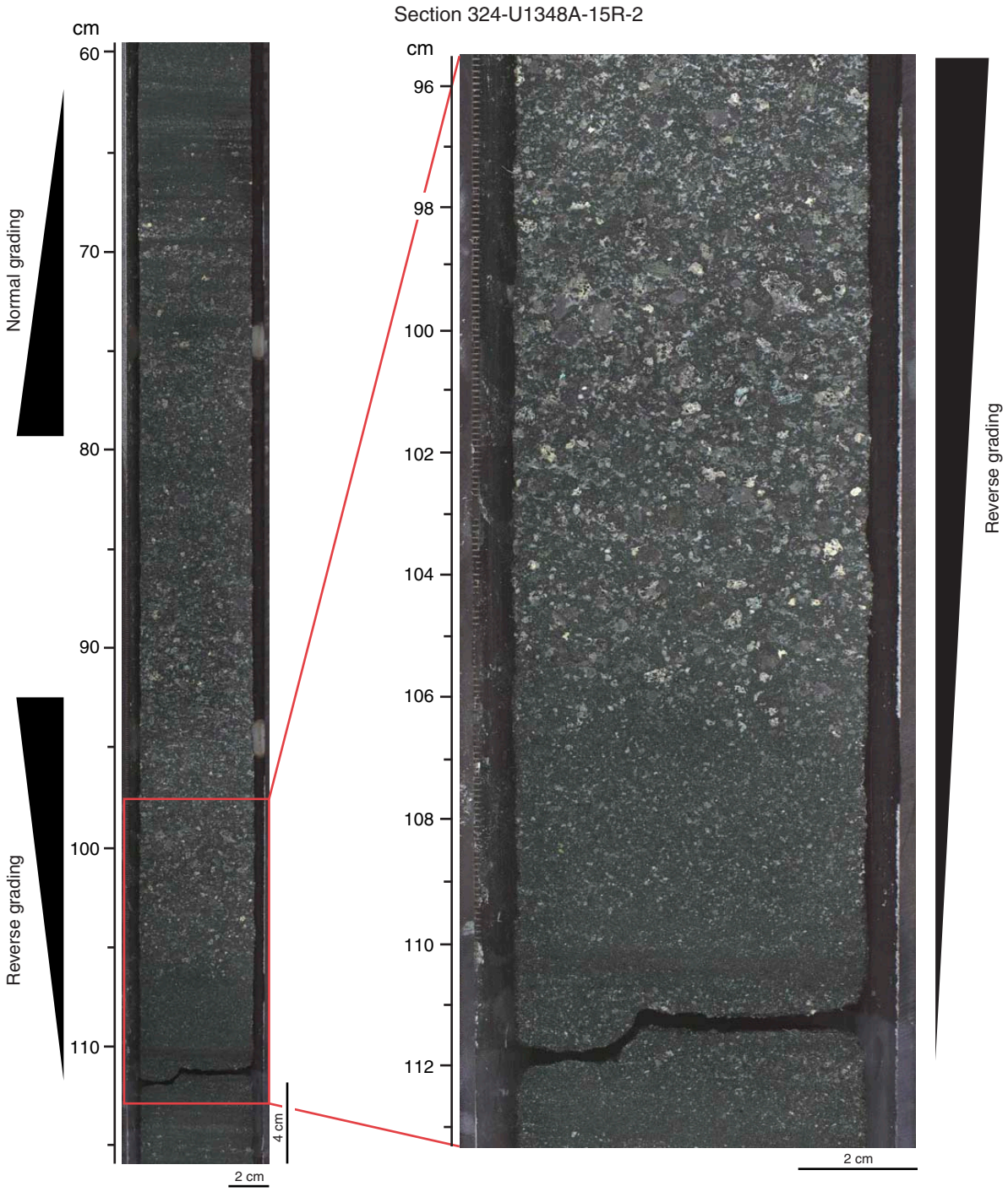

**Figure F15. A.** Core photograph of lower reverse-graded portion of thick clast-rich sequences, Hole U1348A. **B.** Core photograph of clast-rich sequence and concentrated altered vesicular clasts.

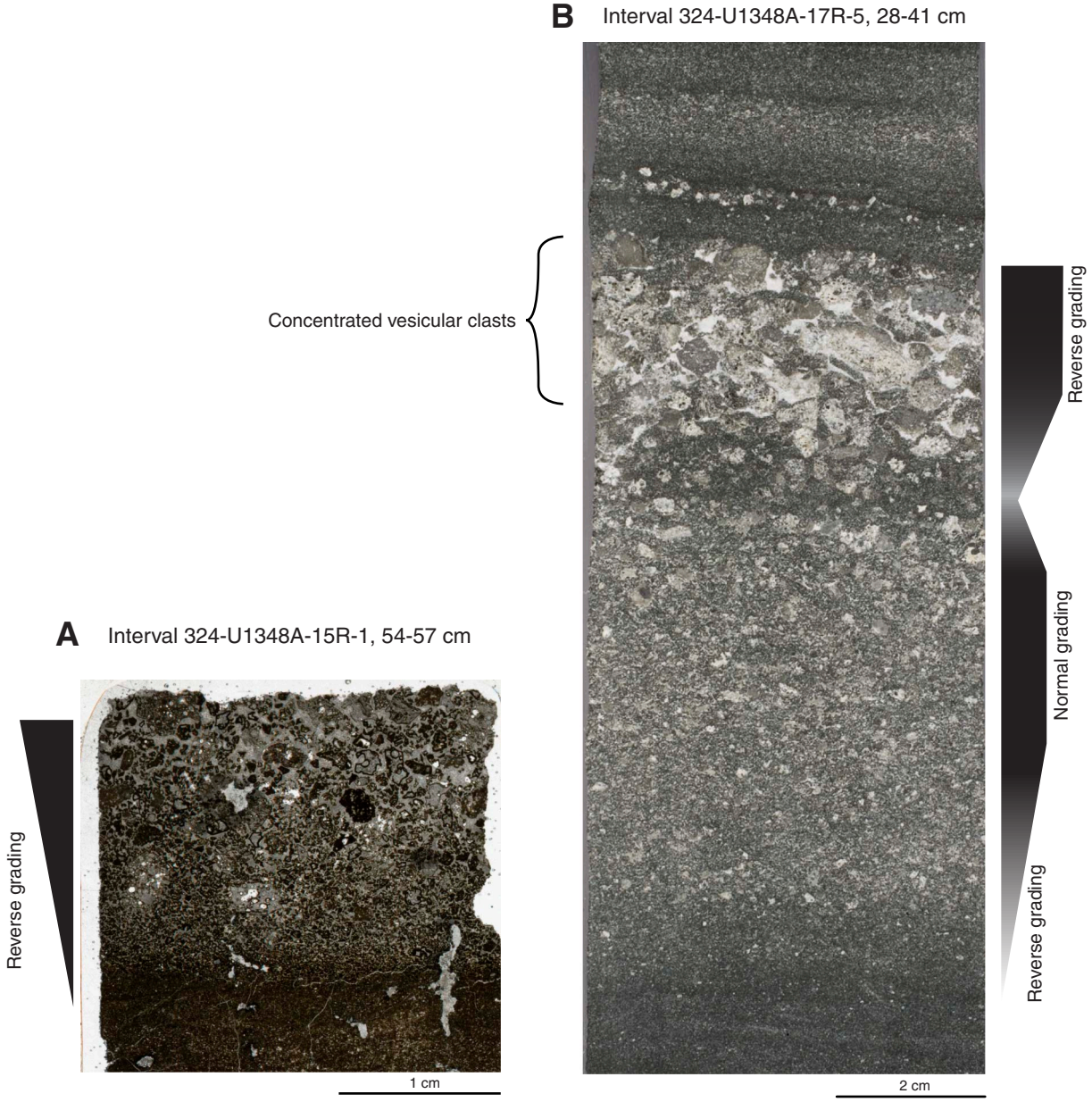

**Figure F16.** Core photographs of succession of fine- to medium-bedded granular hyaloclastites, hyaloclastite sandstone, and fine hyaloclastites, Hole U1348A. CV = concentrated vesicular clasts, CR = clast-rich sequence.

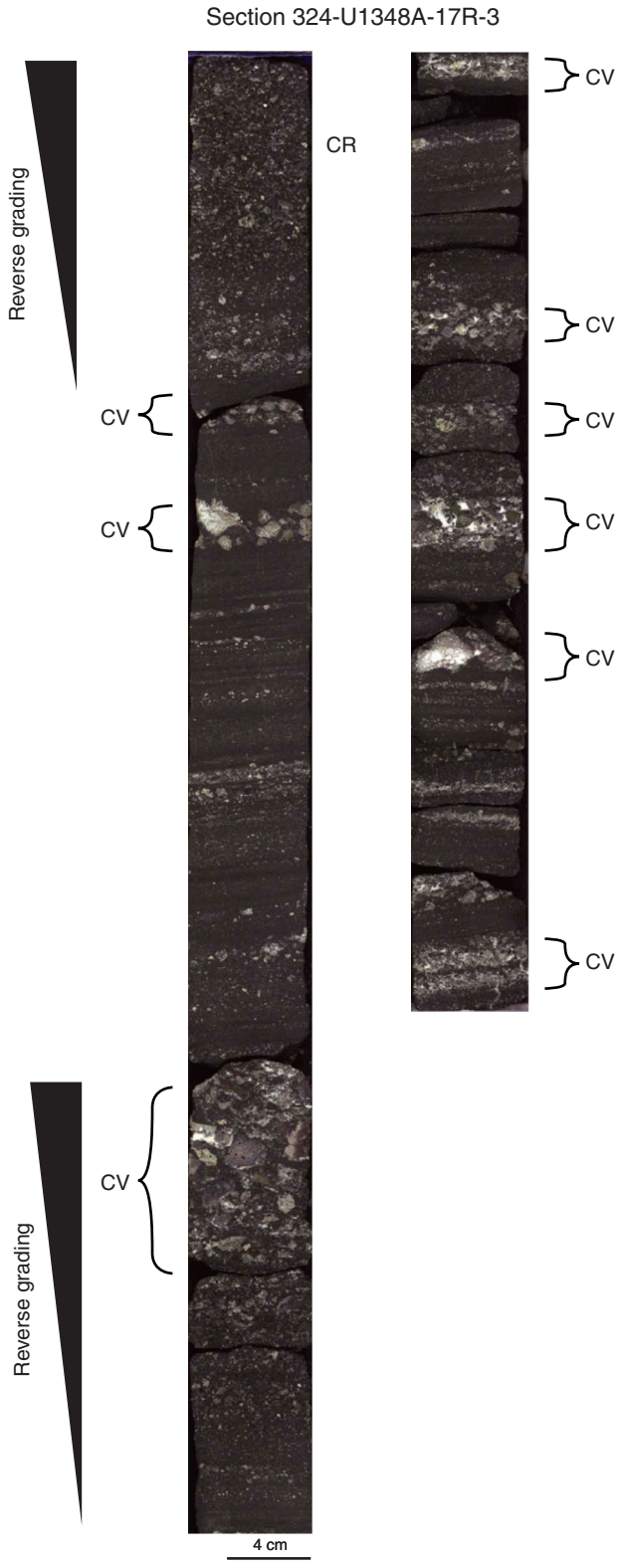

**Figure F17.** Core photographs of large bioclastic components in stratigraphic Unit IV, Hole U1348A. **A.** Large articulated brachiopod shell and other shelly fragments. **B.** Juxtaposed ammonite and gastropod fossils.

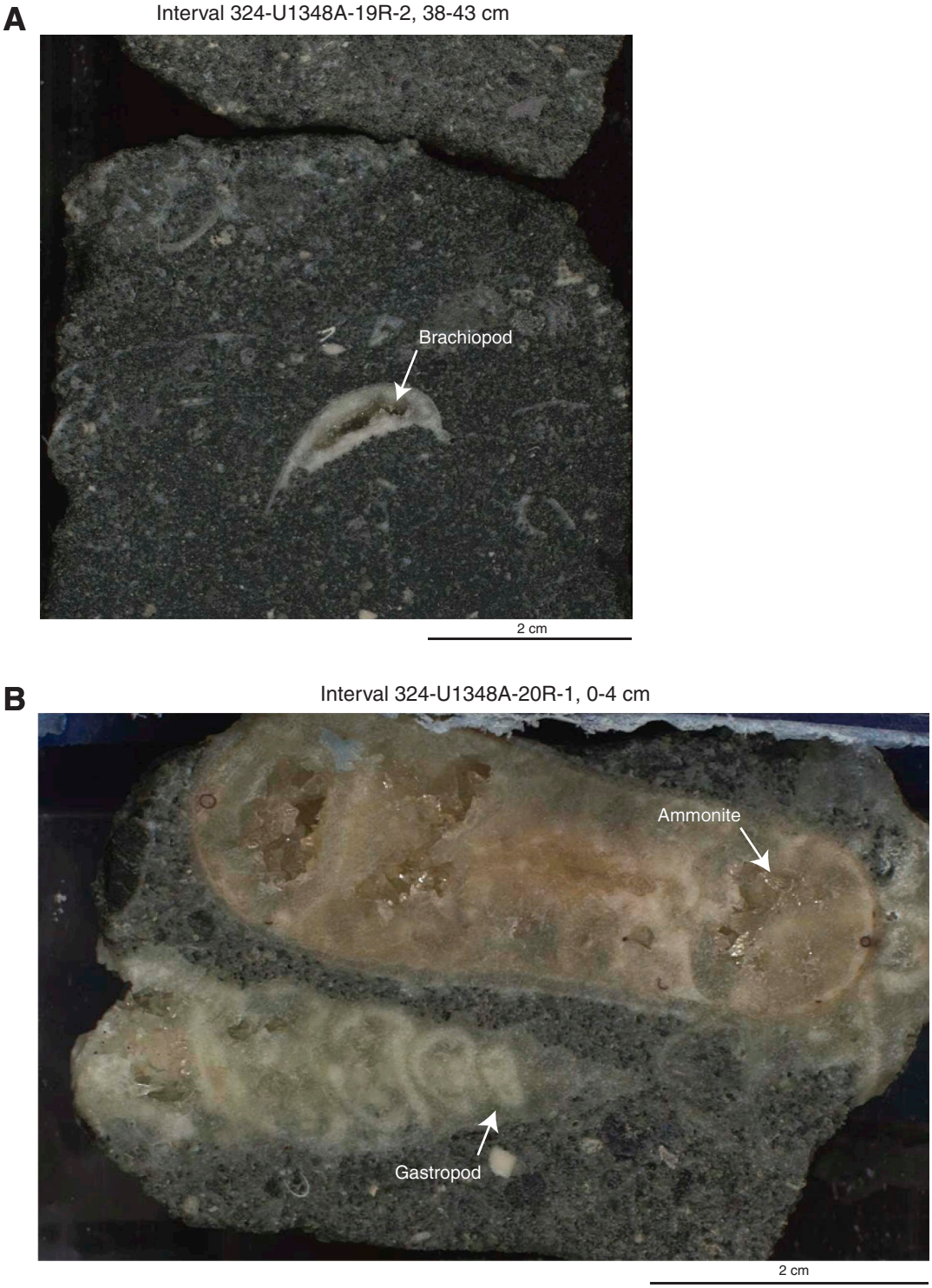

**Figure F18.** Thin section photomicrograph of red vesicular clast, Hole U1348A. Calcite-cemented matrix and surrounding smaller volcanic and biogenic material is visible.

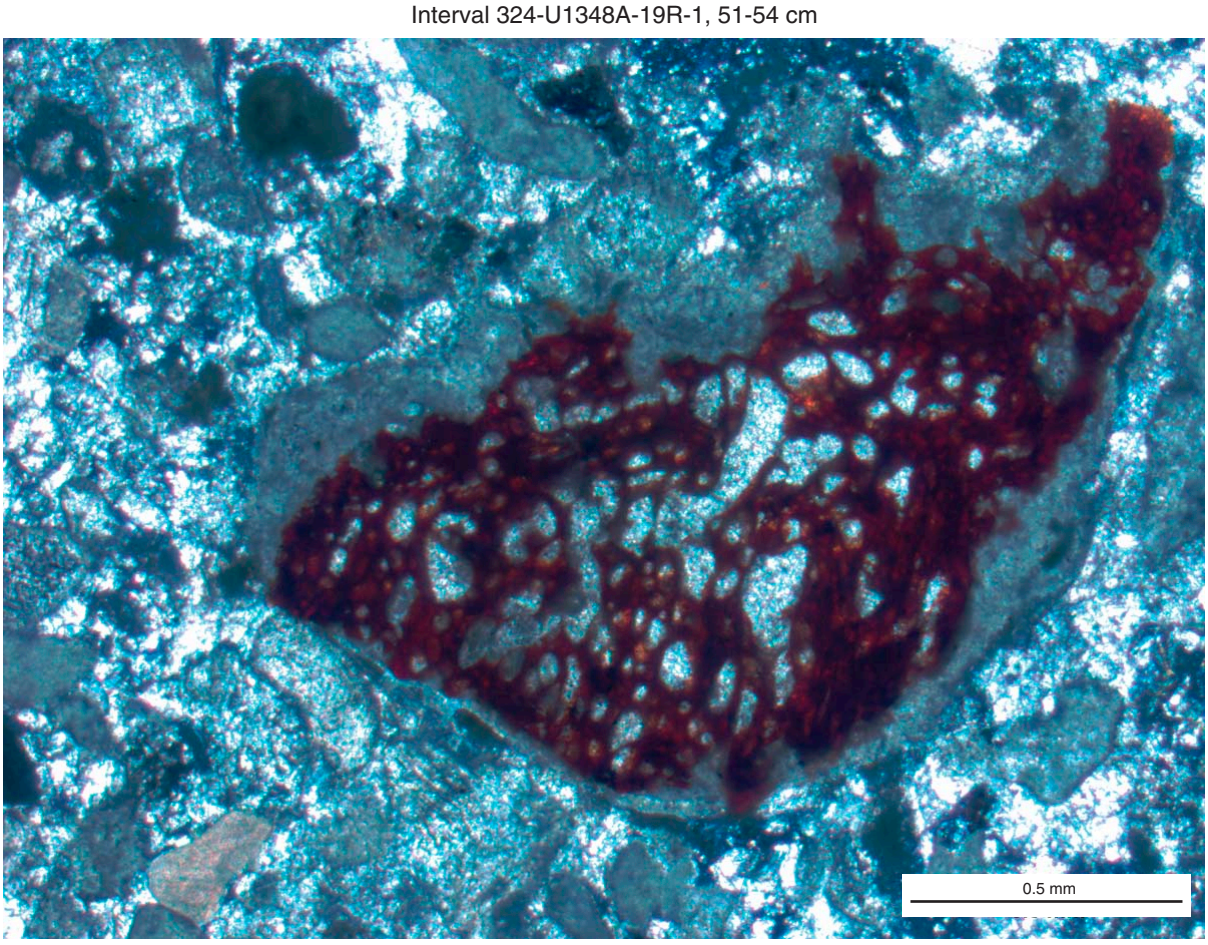

**Figure F19.** Core photographs of typical graded hyaloclastic sequence in stratigraphic Unit V, Hole U1348A. Inset shows laminated and graded structure.

**Figure F20.** Core photographs of structureless clast-supported texture of stratigraphic Unit VI, Hole U1348A.

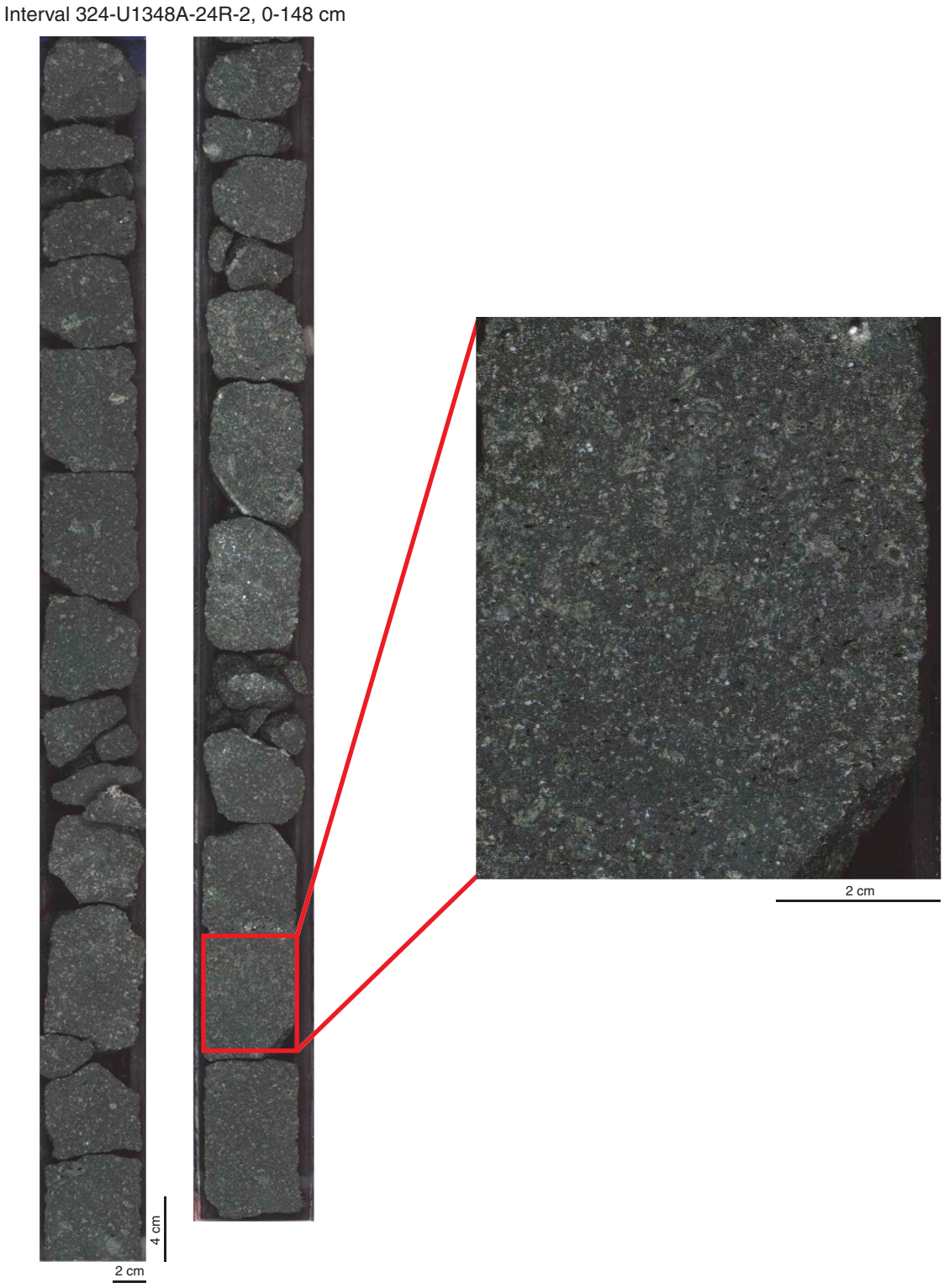

**Figure F21.** Sketch of example of high-density turbidite, showing deposits from the high-density stage, Hole U1348A. Divisions are simplified from Lowe (1982) where layers R2 and R3 represent end stages of gravel wave deposition followed by high-density depositional stages S1 to S3.

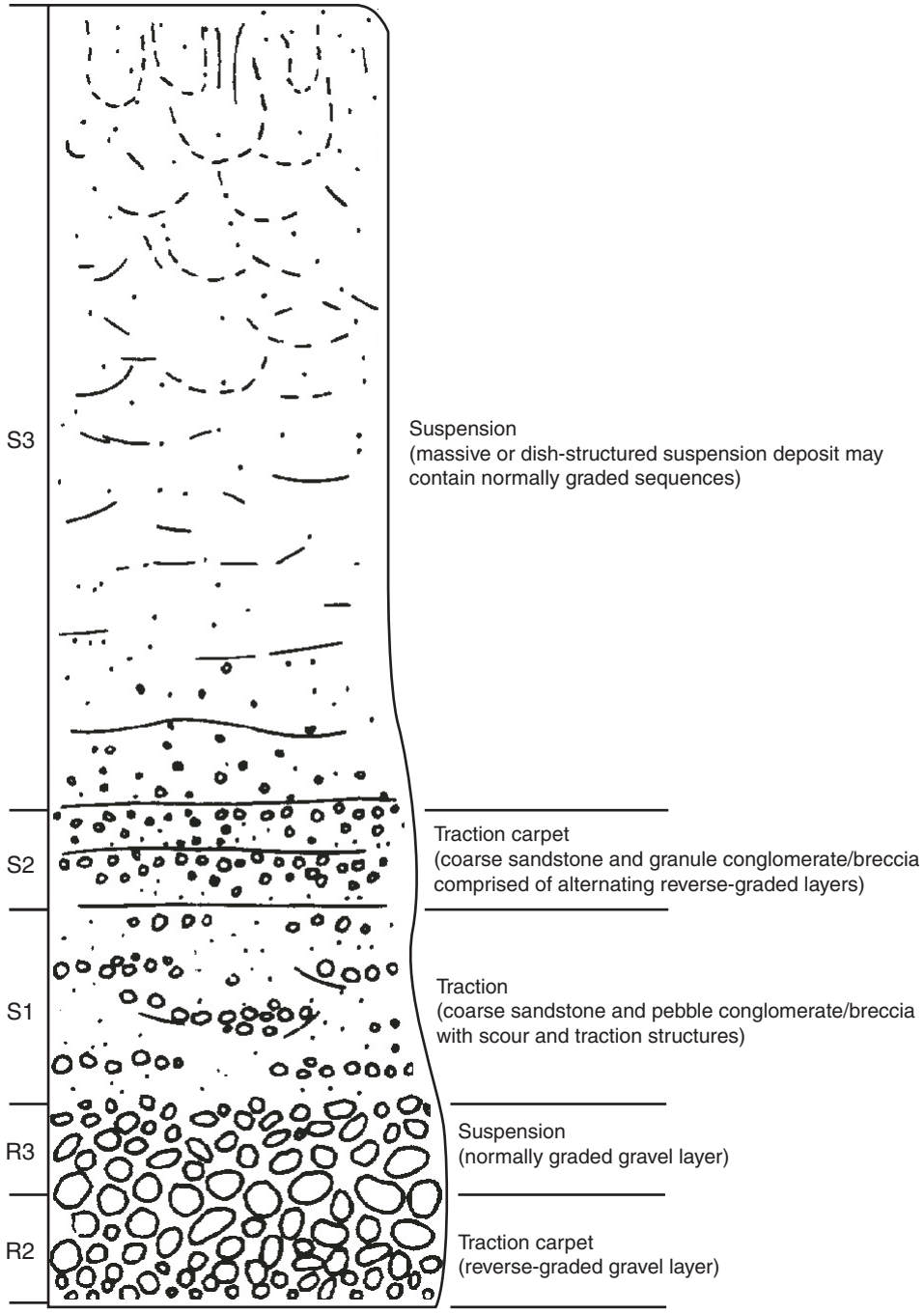

**Figure F22.** Conceptual model of the formation of stratigraphic Units III–V at Site U1348. Uppermost panel shows formation of Unit V (layered granular hyaloclastite) through the action of turbidity currents and grain flows on top of the existing structureless, granular hyaloclastites of Unit VI. As deposition of the Unit V hyaloclastites continues and the volcanic slope apron progrades, the dip of the laminated strata decreases from ~20° to <10°. The central panel shows formation of the bioclastic-rich Unit IV. Volcanic activity is diminished at this time, leading to a relatively larger bioclastic element contributing to the sediments. The lowermost panel shows deposition of Unit III layered and graded granular and fine hyaloclastites through the action of a series of high-density turbidity currents.

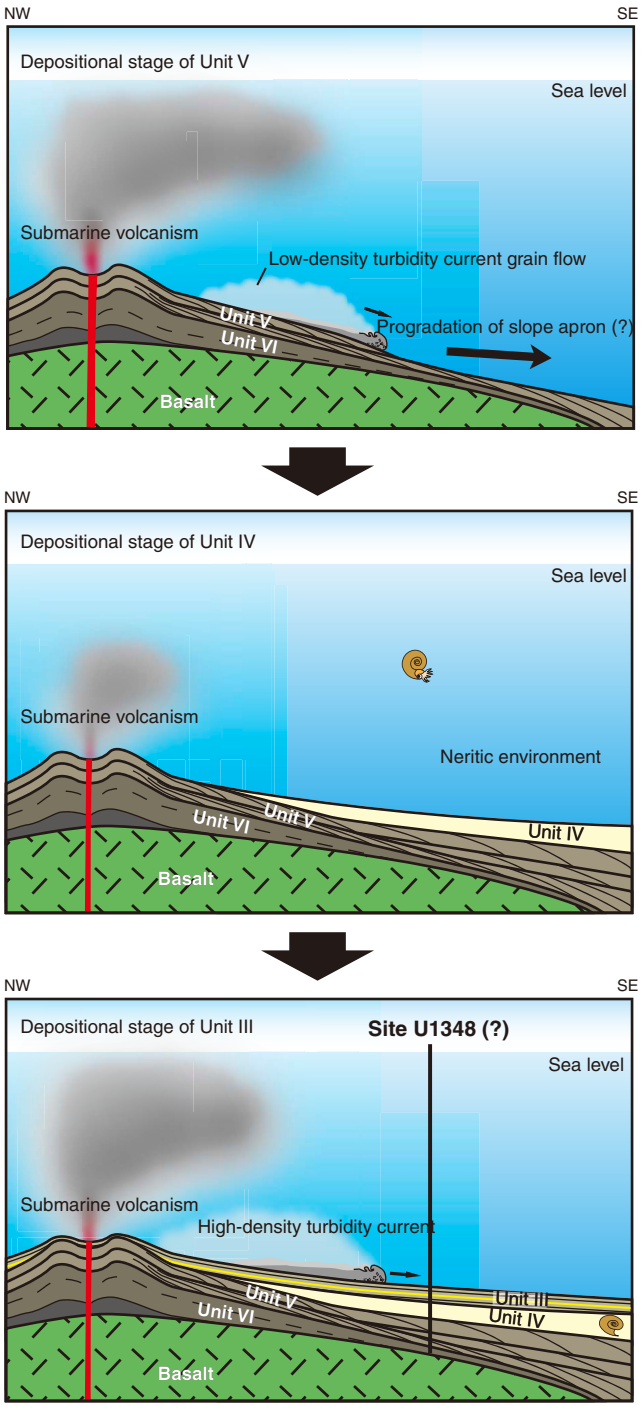

**Figure F23.** Age-depth relationship of Site U1348 (stratigraphic Unit I), based on primary zonal marker species as well as secondary markers and/or assemblage of planktonic foraminifers (PF).

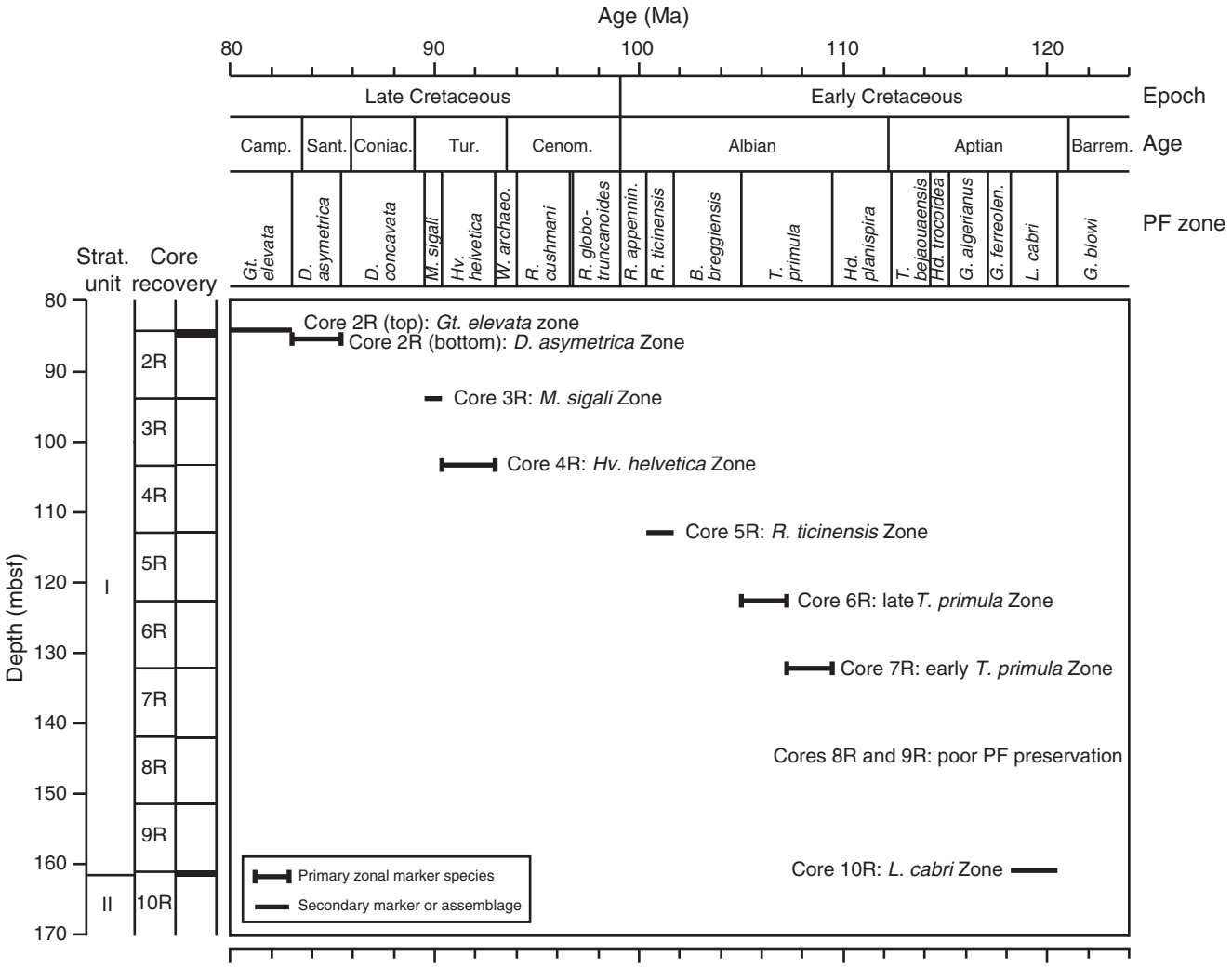

**Figure F24.** Recovery overview, Hole U1348A. Individual unit thicknesses are minimum estimates based on the measured upper and lower contacts identified in the core. Stratigraphic unit thicknesses are based on available coring information (black) and downhole logging measurements (gray).

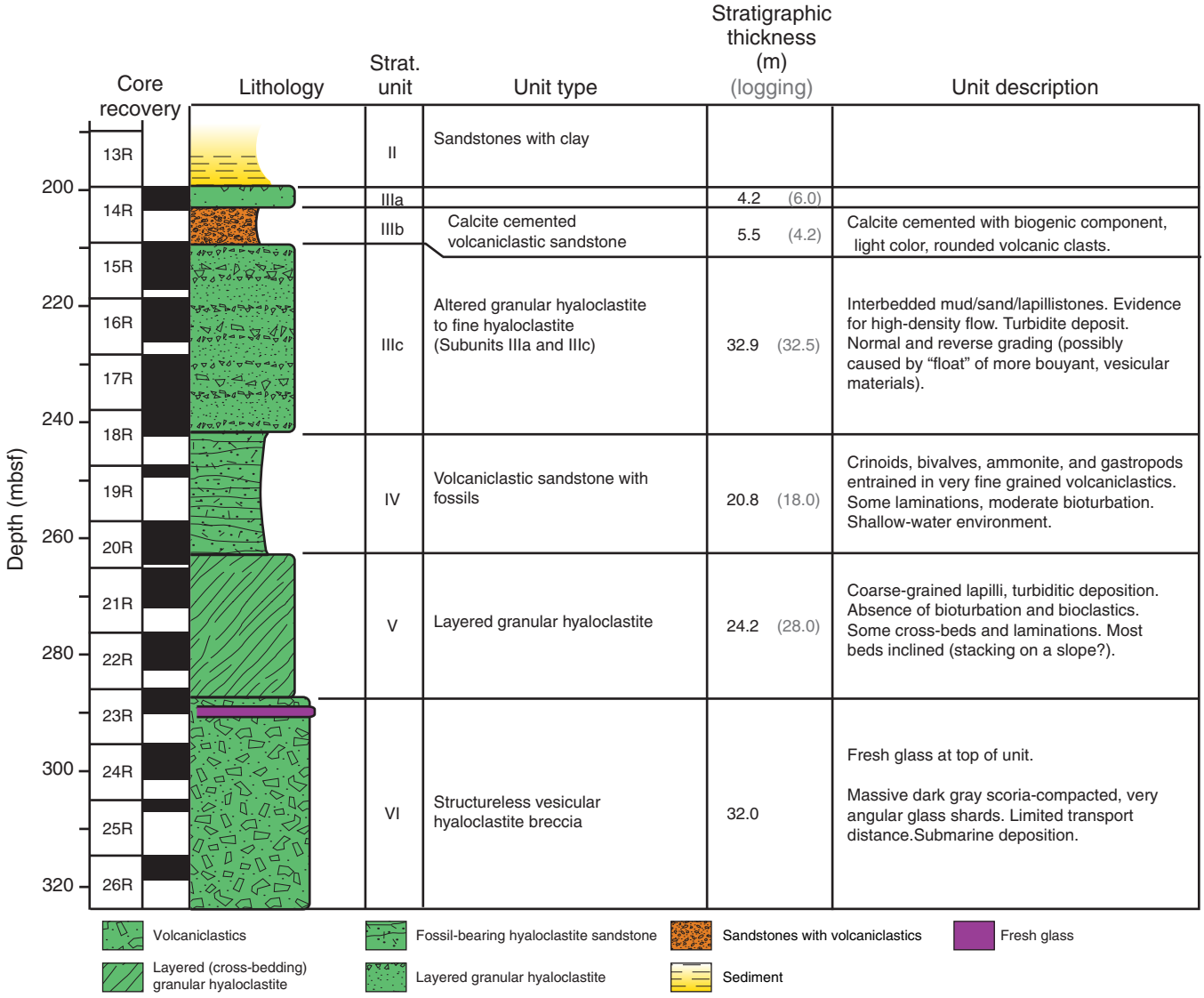

**Figure F25.** Overview of volcanological and physical parameters for Cores 324-U1348A-13R through 26R, Hole U1348A. Note the appearance of a zone of fresh basaltic glass (26 cm) within the volcaniclastic sequence. L* = SHMSL reflectance, NGR = natural gamma radiation, GRA = gamma ray attenuation density, MS = magnetic susceptibility (see **"Physical properties"** for more details).

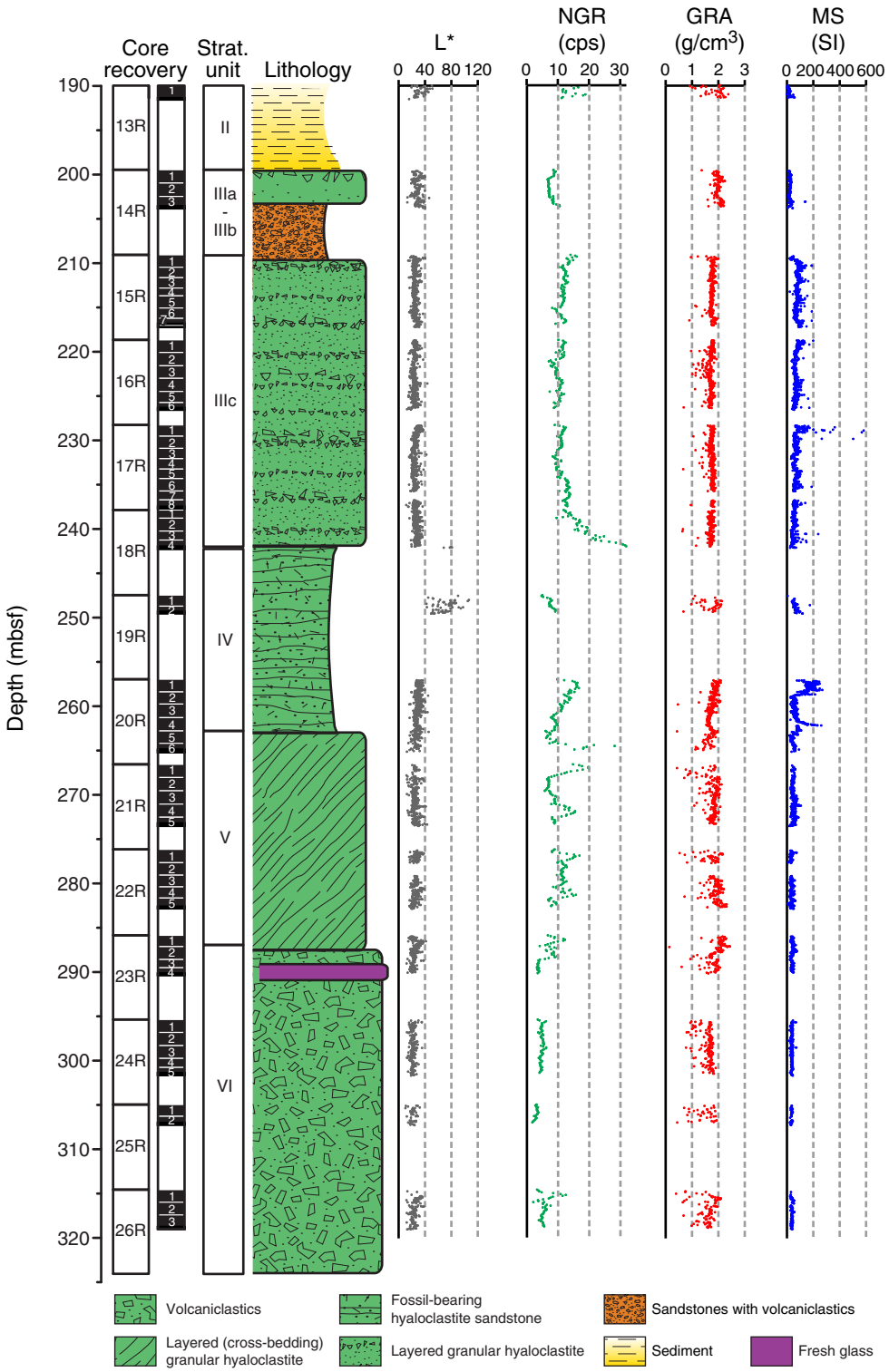

**Figure F26.** (**A**) Core section image, (**B**) thin section scan, and photomicrographs (plane-polarized transmitted light) of sparsely vesicular vitric tuff in Section 324-U1348A-18R-1, top of Unit III, with (**C**) glass shards and bubble wall fragments, (**D**) subrounded vesicular basalt clasts, and (**E**) fine hyaloclastite matrix, Hole U1348A. Thin section scan location of B is indicated by the red box in A. Width of field of view of photomicrographs is ~15 mm (1.25×) in panels C, D, and E. White arrows = orientation in core.

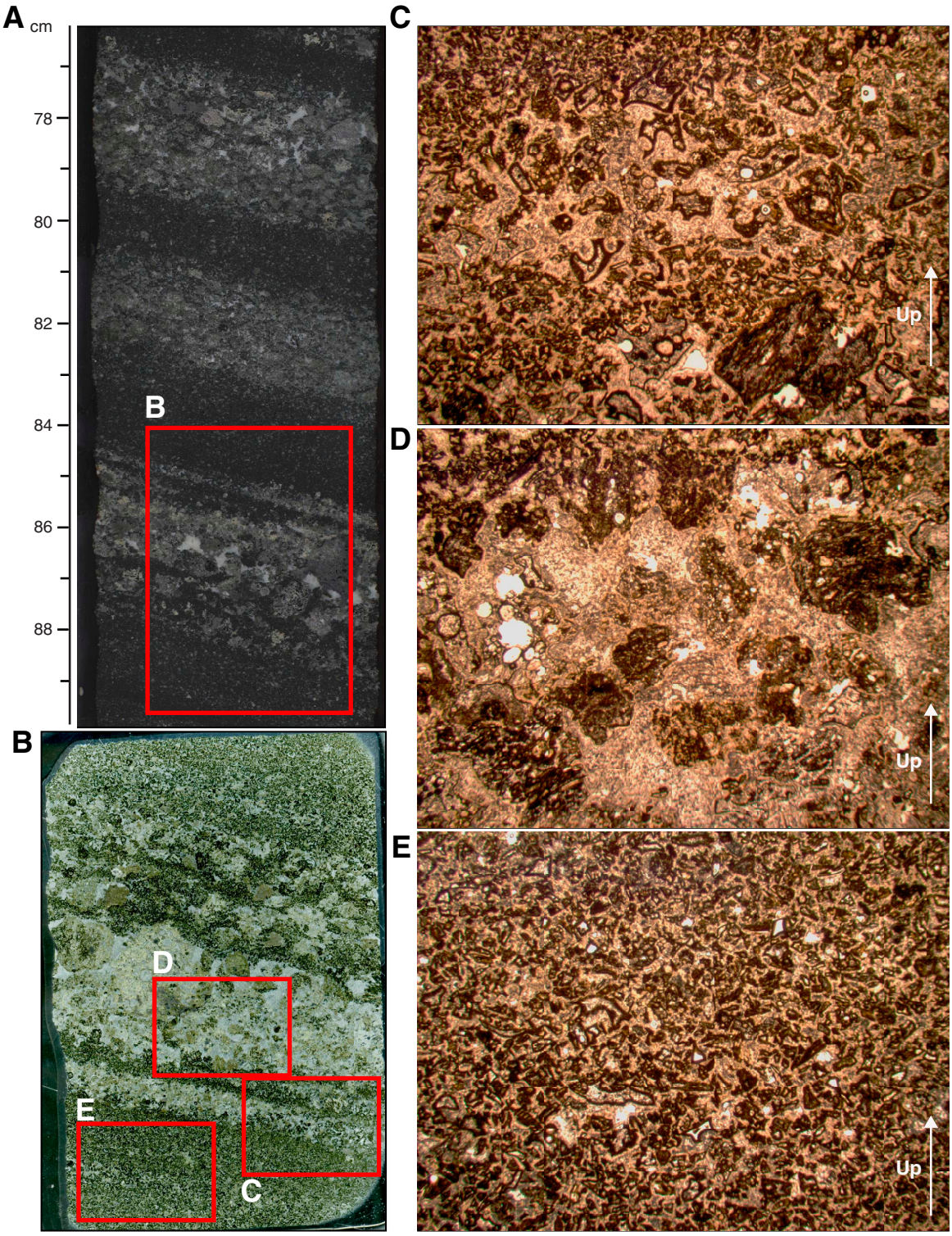

**Figure F27.** (**A**) Core section image, (**B**) thin section scan of angular glass shards in calcite cement, and (**C**, **D**) photomicrographs (plane-polarized light) of glass shards (bright colored fragments) at the top of Unit VI, Hole U1348A. Thin section scan location of B is indicated by the red box in A. Red boxes in B indicate photomicrograph locations. Width of field of view of photomicrographs is ~15 mm (1.25×).

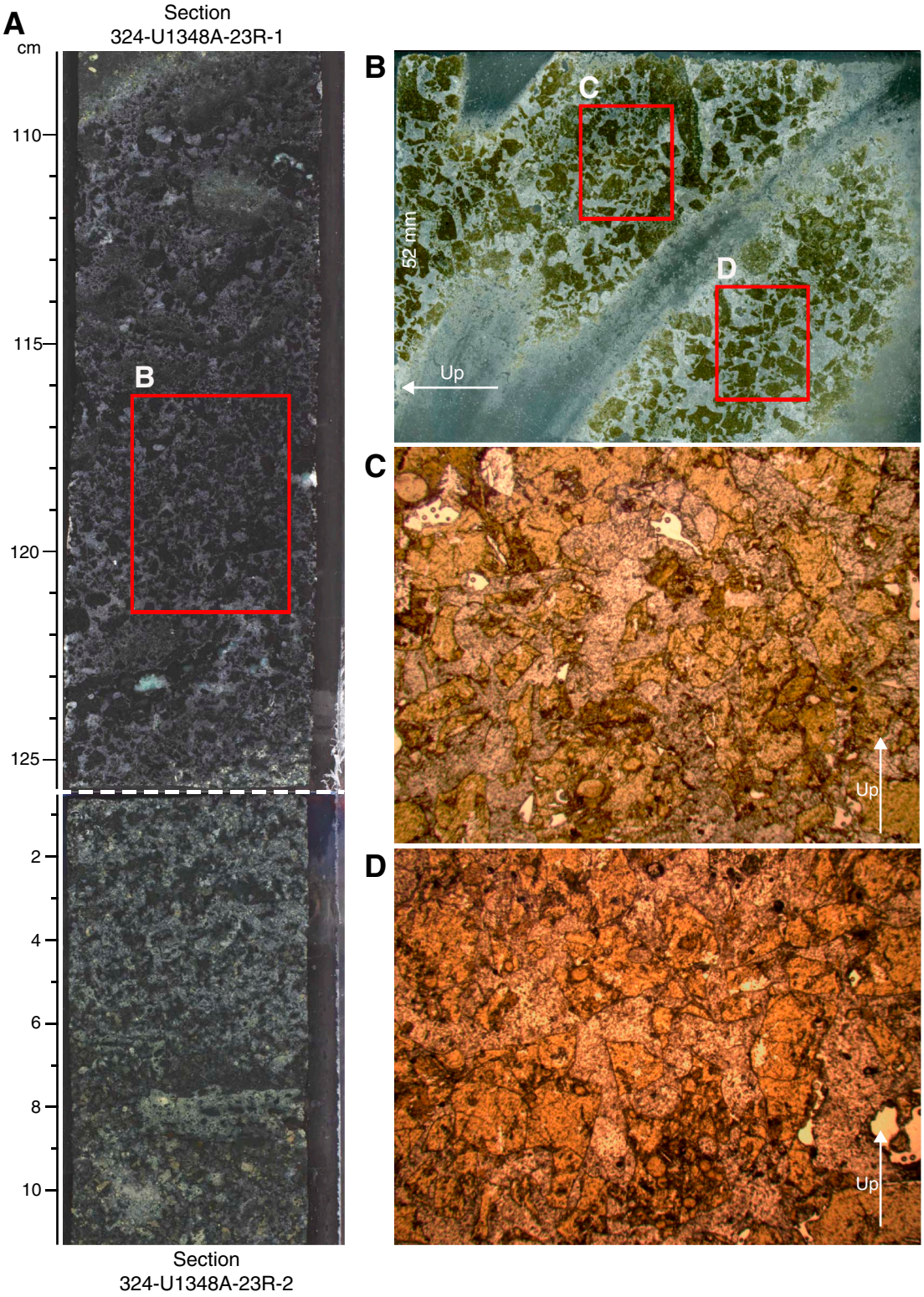

**Figure F28.** Downhole caliper, electrical resistivity, and gamma ray logs, Hole U1348A. IDPH = deep induction phasor-processed resistivity, IMPH = medium induction phasor-processed resistivity, SFLU = spherically focused resistivity, HSGR = gamma ray log, HCGR = computed gamma radiation.

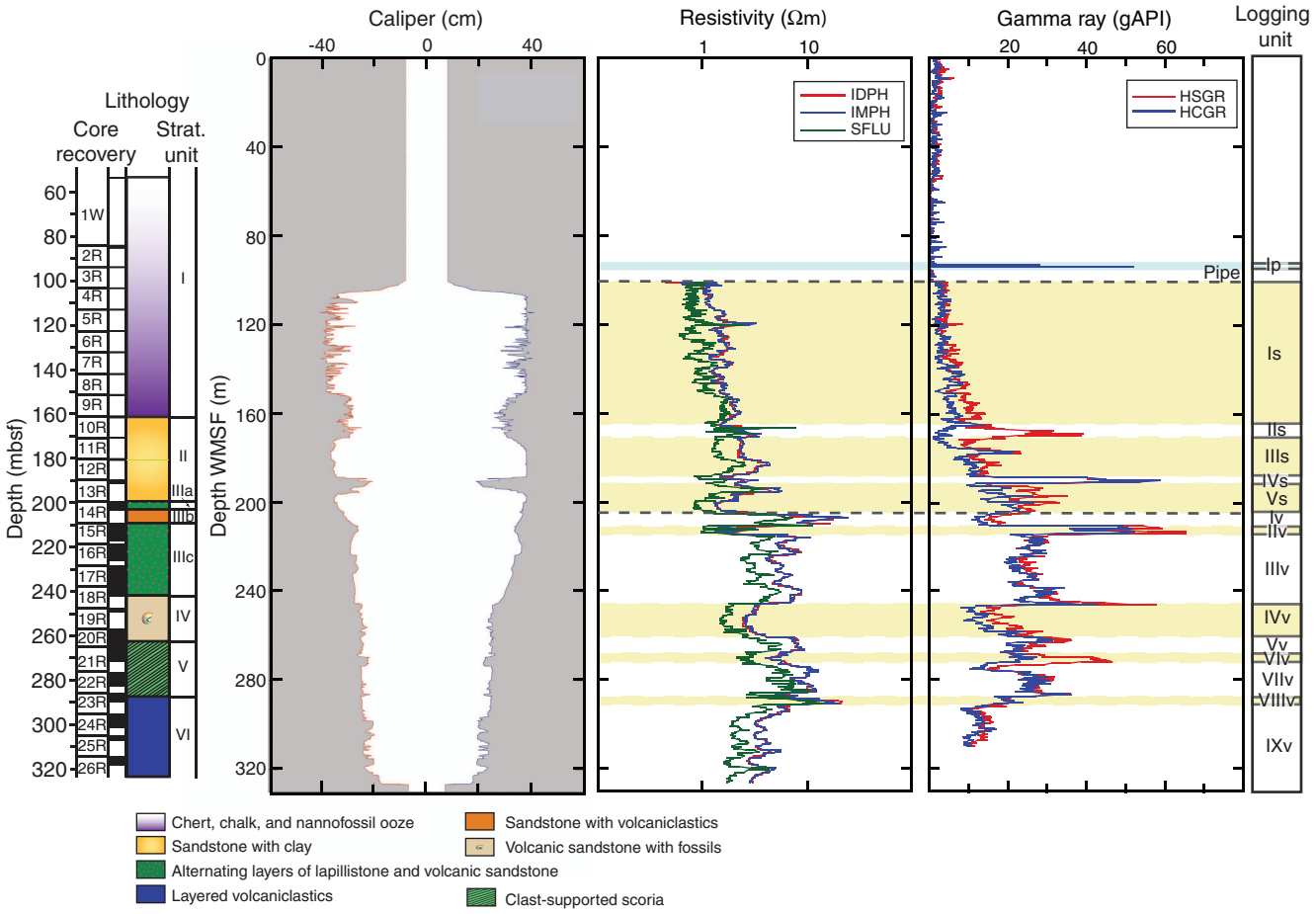

**Figure F29.** Whole-rock $K_2O$ elemental concentrations and downhole spectral gamma ray logs of uranium, potassium, and thorium, Hole U1348A. Solid circles = whole rock $K_2O$ elemental concentrations from ICP-AES measurements on core samples. HFK = gamma ray log potassium measurement.

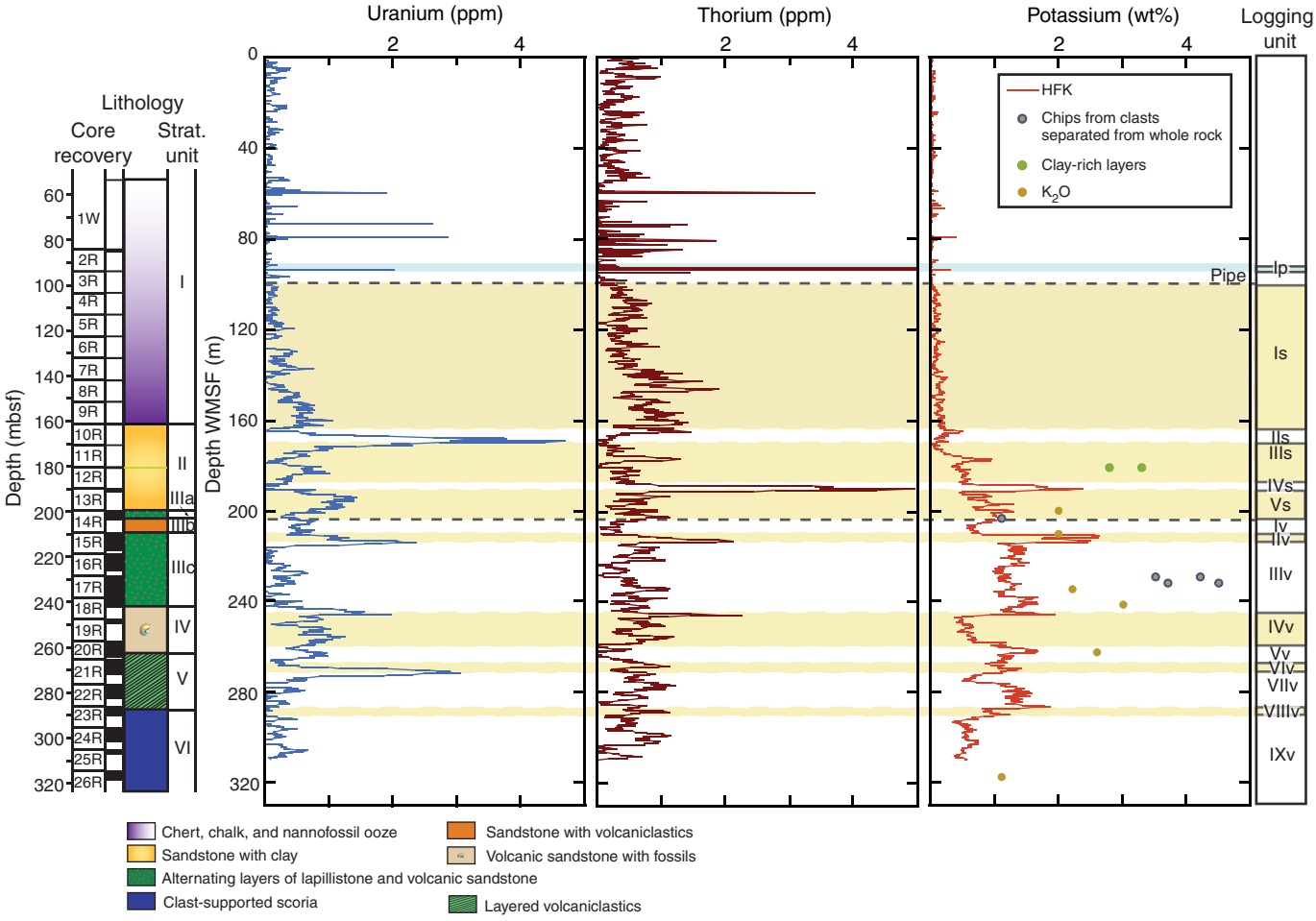

**Figure F30.** Downhole caliper, density, and *P*-wave velocity, Hole U1348A. Solid circles = physical property measurements made on core samples. HROM = high-resolution corrected bulk density, MAD = moisture and density, VCO = compressional velocity.

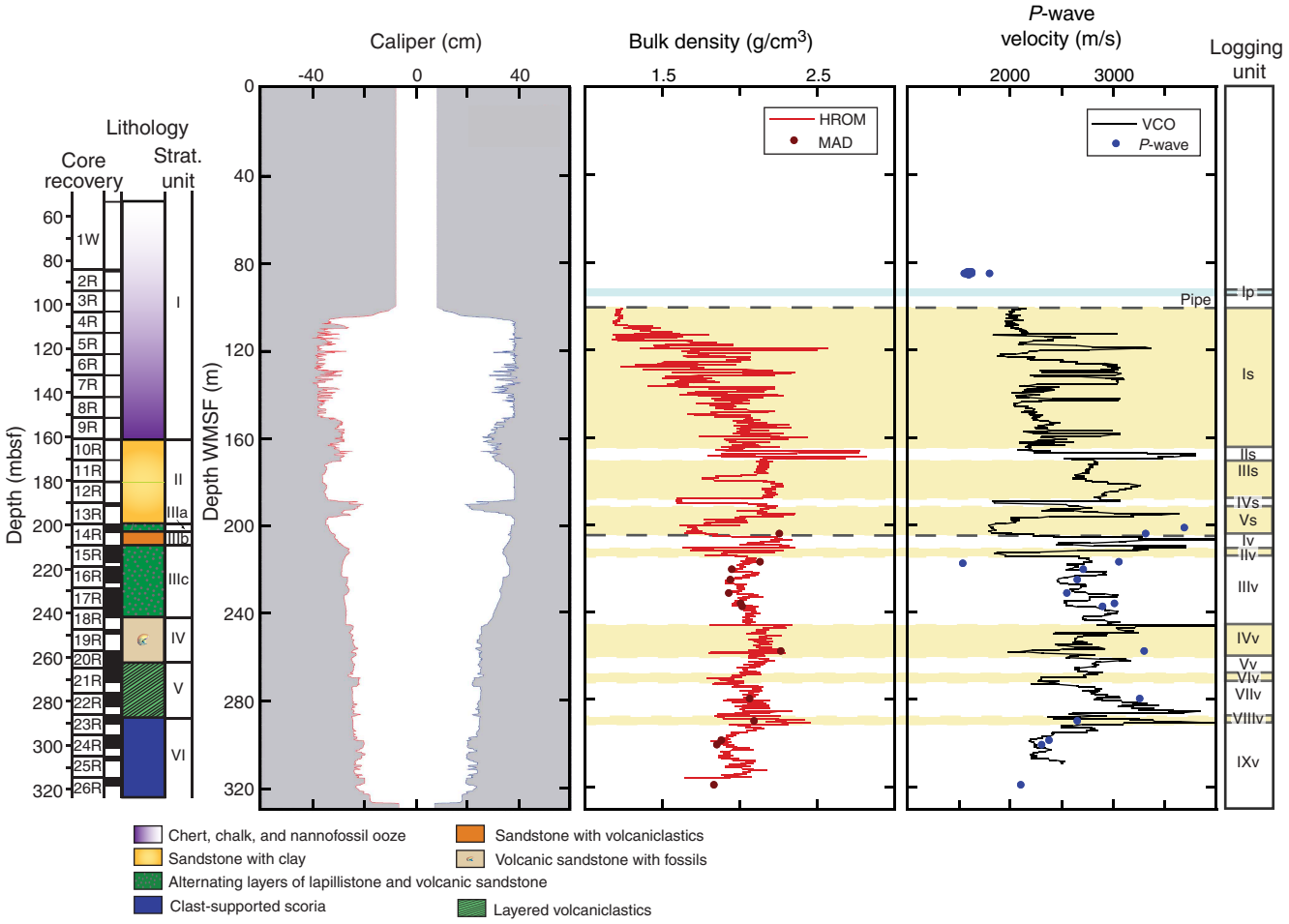

**Figure F31.** Scheme for physical-chemical alteration of volcanic glass shards, Hole U1348A. **A.** Original glass shard with minor vesiculation and incipient fractures. **B.** Edges of the original shard become replaced, initially through a devitrification process caused by palagonitization. **C.** Palagonitization progresses further inward, replacing the greater proportion of the primary glass composition and spheroids begin to develop. **D.** Clay-rich boundaries form around the palagonitized shard, and spheroids increase in both size and frequency. **E.** Further alteration produces a series of clay boundaries, both around the palagonitized shard and around the developing spheroids inside. **F.** The former glass shard now consists of spheroids set in a pseudomorphed outline preserved as a thin clay rind set within a zeolite matrix. **G.** Compaction, either through increasing overburden or mechanical weakening caused by the mineral replacement process, distorts the clay rims of spheroids, imparting a closely packed texture of oblate structures. **H.** Continued compaction results in a fine-grained material set in a zeolite/calcite matrix.

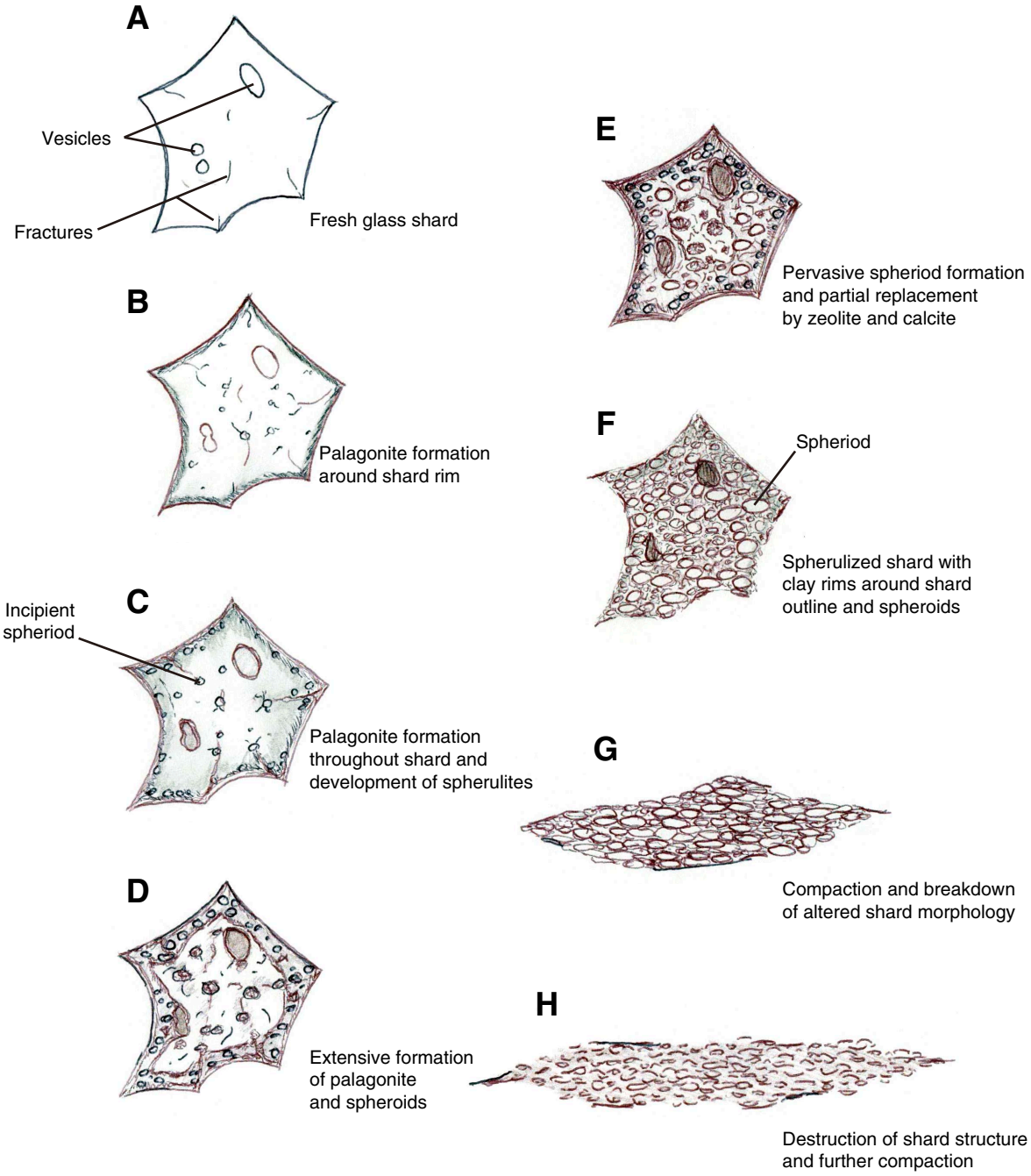

**Figure F32.** Thin section photomicrograph of angular fresh to partly altered glass fragments embedded in calcite cement, Hole U1348A. Darker brown portions are altered. Curving fracture surfaces bound the fragments. Small plagioclase crystals can be discerned in many pieces (Thin Section 197; Sample 324-U1348A-23R-1, 116–122 cm). **A.** Large shards at the top can be fit back together in puzzle-piece fashion. **B.** Large glass shard.

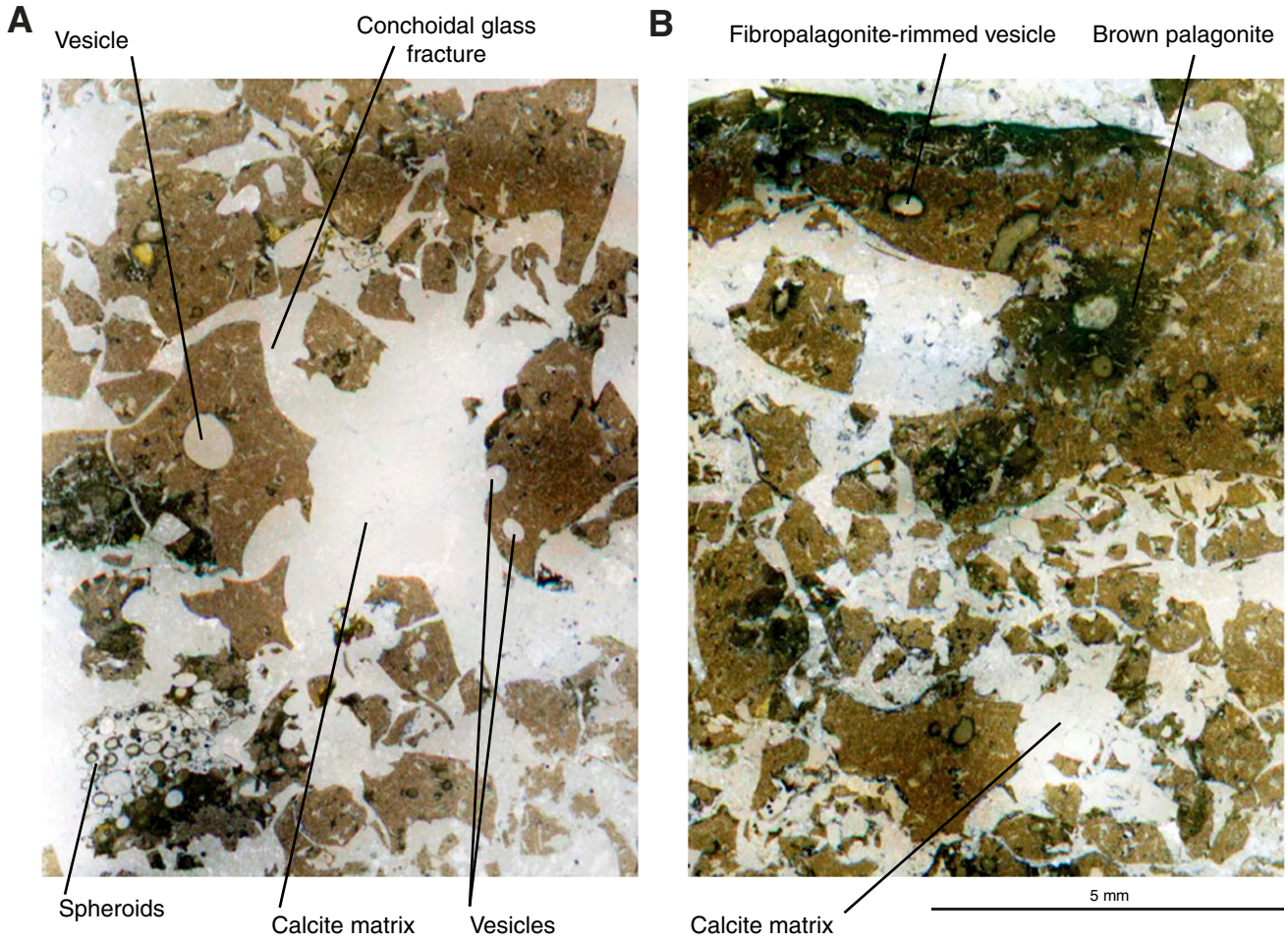

**Figure F33.** Composite photomicrograph of the large shard at the top of B in Figure F32, Hole U1348A. The distinction between darker altered and lighter brown fresh glass is evident. Altered glass can be seen adjacent to vesicles and along fractures, reaching into the interior of the shard. The shard is divided into fracture-bounded segments, many of them delineated and rounded by alteration. Fibrous orange clays line two vesicles on the left. The white matrix is calcite (Thin Section 197; Sample 324-U1348A-23R-1, 116–122 cm).

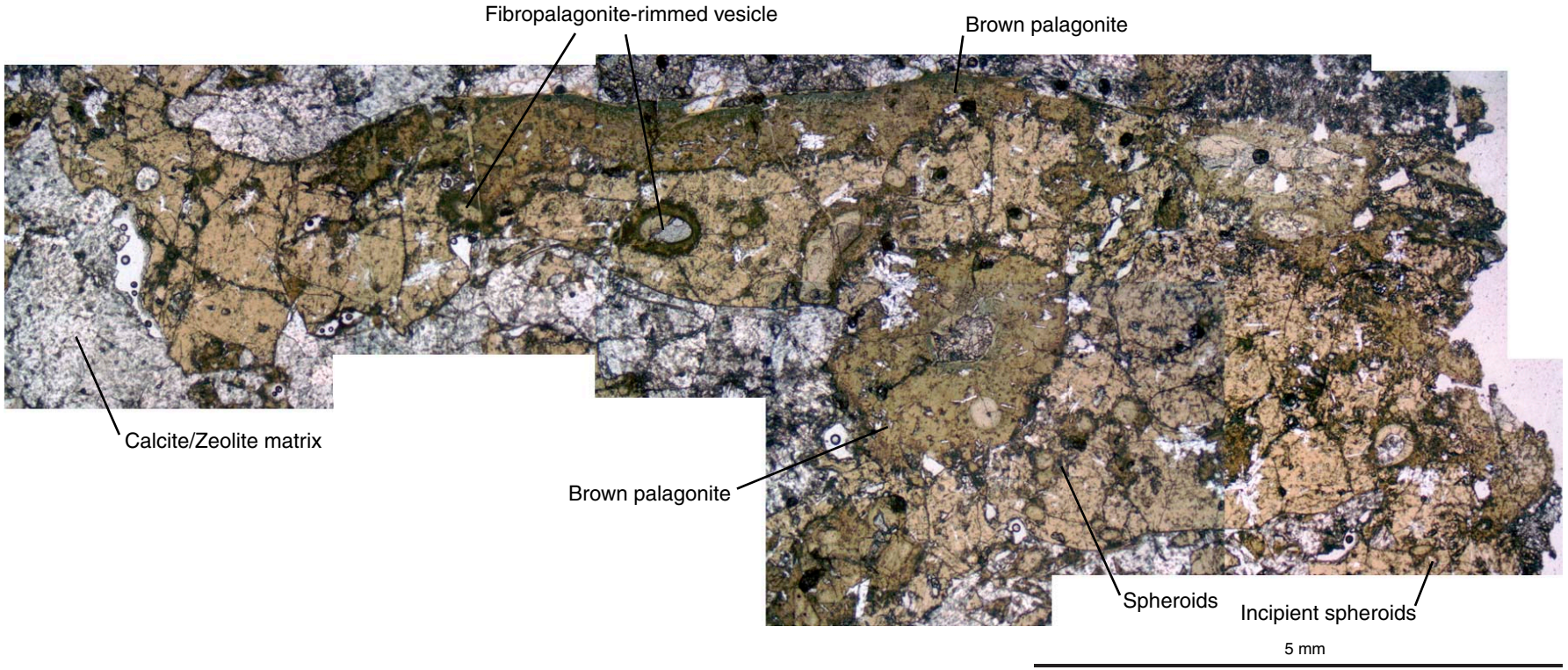

**Figure F34.** Thin section photomicrographs emphasizing details of spheroid formation in glass (Thin Section 197; Sample 324-U1348A-23R-1, 116–122 cm), Hole U1348A. **A.** Light brown areas of fresh glass. Altered areas contain fibrous orange clays along fractures and surrounding incipient spheroids. **B.** Fresh olivine (high relief) and intergrown plagioclase (white and elongate) and clinopyroxene (white and almost square) microlites. **C.** Larger bundle of intergrown plagioclase and clinopyroxene. **D.** Spheroids with almost the same color as the glass but surrounded by fibrous orange clays arranged along small cracks in the glass. **E.** Same view as D but emphasizing the radial pattern of fibropalagonite developing in the spheroids. Fresh plagioclase needles are white. A–D are under plane-polarized transmitted light; E is under partial cross-polarized light.

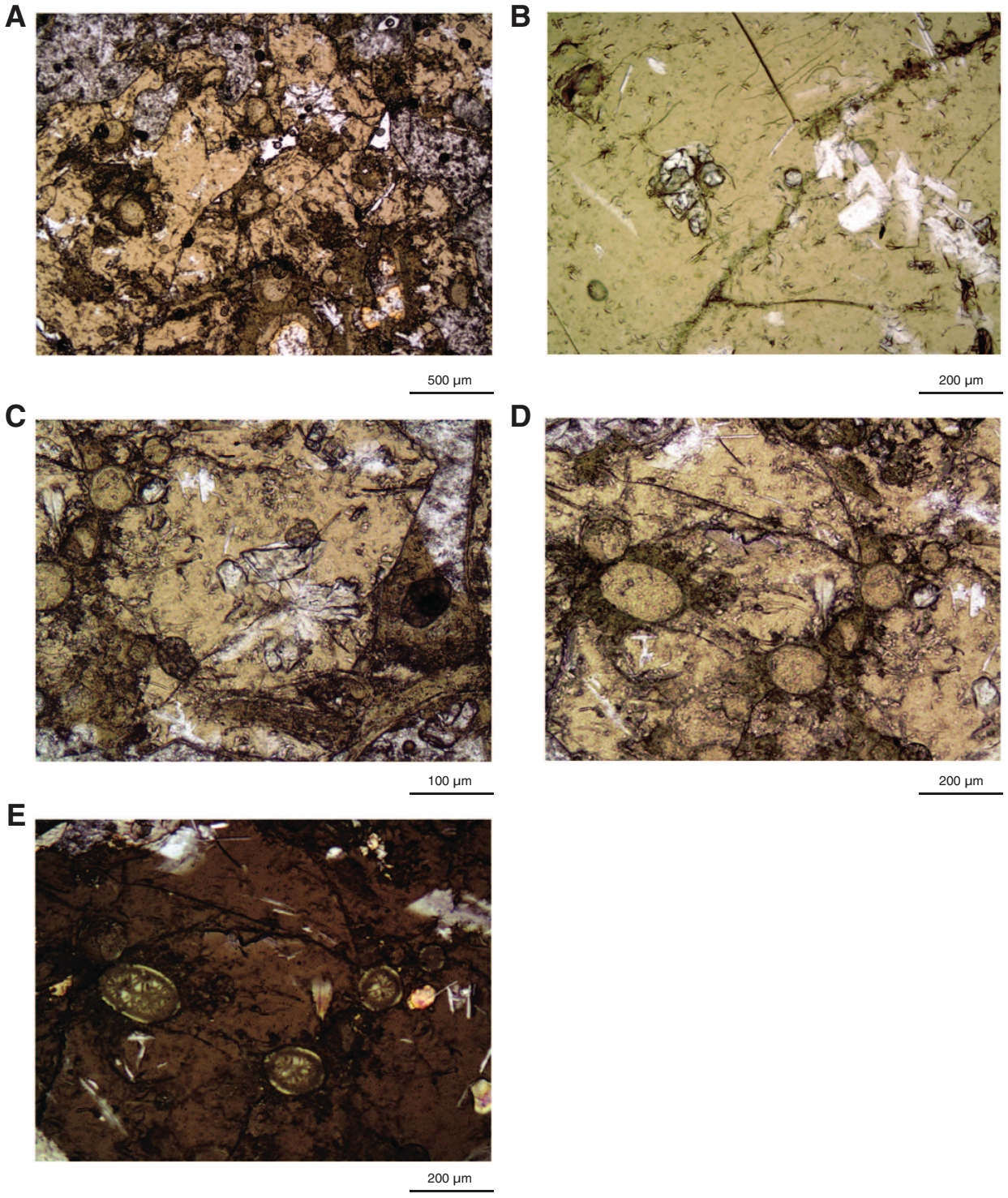

**Figure F35.** Thin section photomicrographs emphasizing details of glass shard transformation and characteristics of palagonite development in altered hyaloclastite, Hole U1348A. **A.** Extensive spheroid development at the edge of an altered glass grain (Thin Section 155; Sample 324-U1348A-13R-1, 43–47 cm). **B–D.** Thin Section 157 (Sample 324-U1348A-14R-1, 18–20 cm). B. Bubble-wall outline of an altered shard rimmed with fibropalagonite and with a completely replaced interior. C. Altered stretched glass with "ribs," having the same alteration features. D. Irregular hyaloclastite glass shard with closely spaced interior spheroids. **E.** Outlines of angular glass shards rimmed with fibropalagonite and interiors replaced by calcite and surrounded by radiating zeolite that defines an original porosity of ~30% (Thin Section 169; Sample 324-U1348A-18R-3, 11–15 cm). Transmitted light.

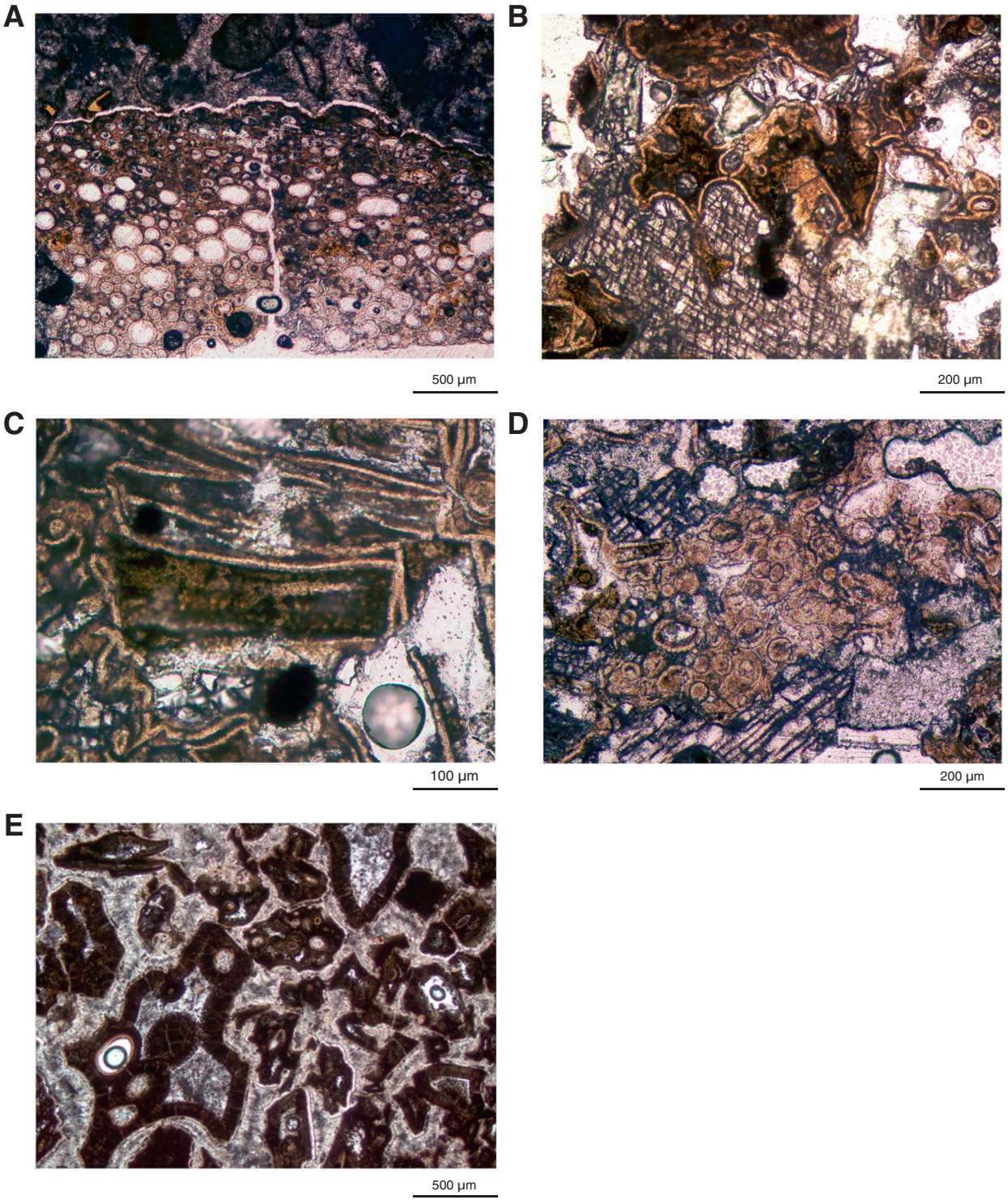

**Figure F36.** Thin section photomicrographs showing details of replacement and cementation of altered glass, Hole U1348A. **A.** Detail of a shard rimmed with fibropalagonite and with the interior replaced by calcite, set in zeolite or phosphorite (Thin Section 161; Sample 324-U1348A-16R-2, 54–57 cm). **B.** Calcite replacing the interior of an angular shard; the shard is set in cement of calcite (upper left) and phosphorite (no birefringence, bottom and right) (Thin Section 165; Sample 324-U1348A-16R-2, 76–78 cm). **C–E.** Thin Section 162 (Sample 324-U1348A-15R-5, 55–59 cm). C. Fibrous high-Mg calcite or aragonite cement. D. Fibropalagonite rims altered to green clays, with interior replacement and calcite-phosphorite cement. E. Detail of nonbirefringent phosphorite cementing altered palagonite. **F.** Altered angular and subround hyaloclastite with fibropalagonite rims and spectacularly developed fibrous zeolite (probably phillipsite) cement (Thin Section 165; Sample 324-U1348A-16R-2, 76–78 cm). **G.** Authigenic minerals in vesicles, mainly clays (light brown), but with a combined rosette of calcite and phillipsite (right) and round botryoidal pyrite (black) (Thin Section 158; Sample 324-U1348A-14R-3, 54–56 cm). A, D, F, and G are under transmitted light; B, C, and E are under cross-polarized light. (**Figure shown on next page.**)

Figure F36 (continued). (Caption shown on previous page.)

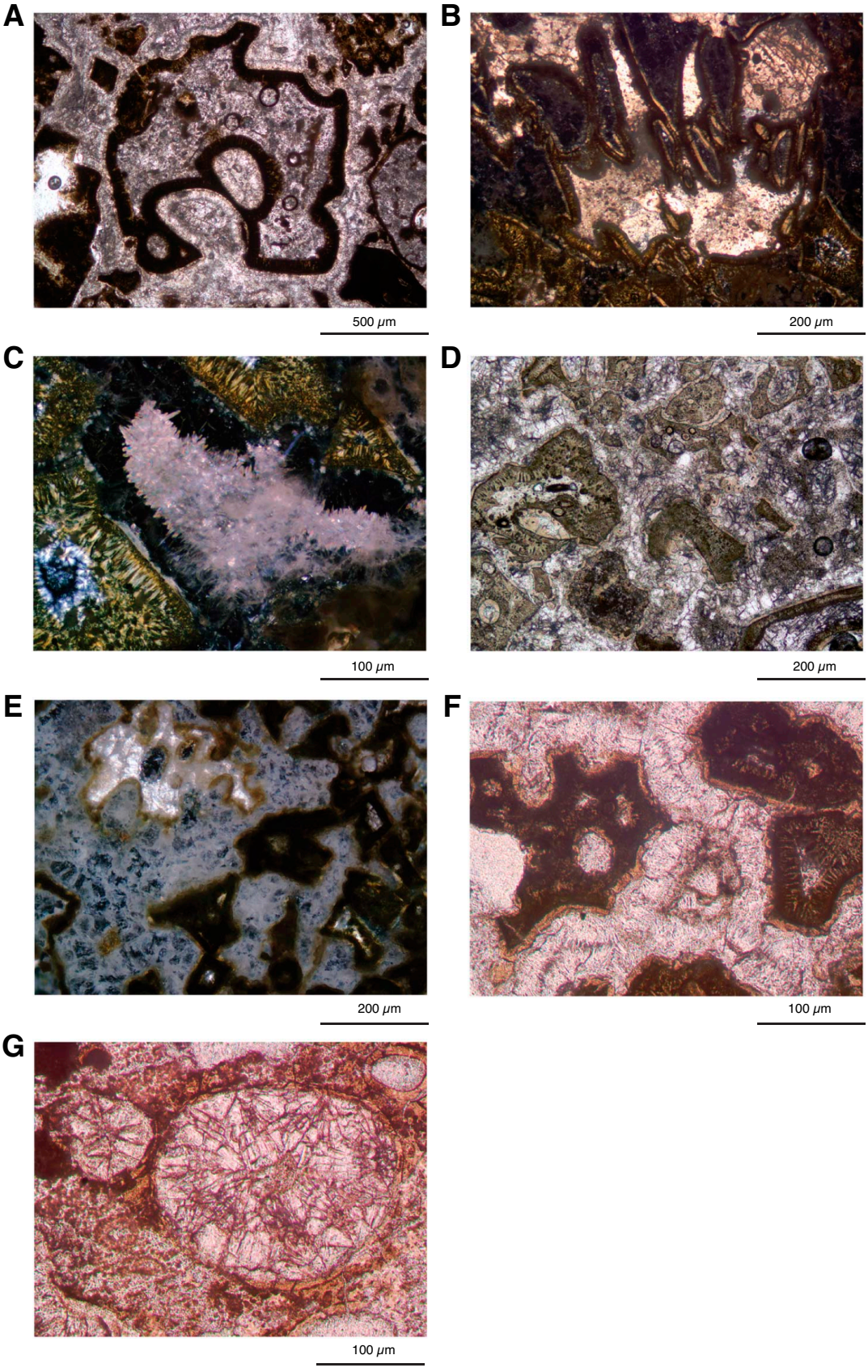

**Figure F37.** Core photograph and thin section photomicrographs detailing textural variations across a basalt clast, probably a pillow fragment (Thin Section 163; Sample 324-U1348A-15R-5, 55–59 cm), Hole U1348A. **A.** Clast embedded in breccia (interval 324-U1348A-14R-3, 57–60 cm). **B.** Oxidized spherulitic texture at the edge of the clast. Vesicles are lined with orange clays and (at left) calcite. **C.** Sheaf spherulitic texture and acicular plagioclase microlites. **D.** Radiating acicular plagioclase spherulites and microlites ~1 cm from original edge of clast, the farthest limit into the clast provided by the thin section. B–D are transmitted light. Note: photomicrographs of B–D show example of photomicrographic variation from edge to inner parts of a basaltic clast. The clasts of A–C were cored from different intervals.

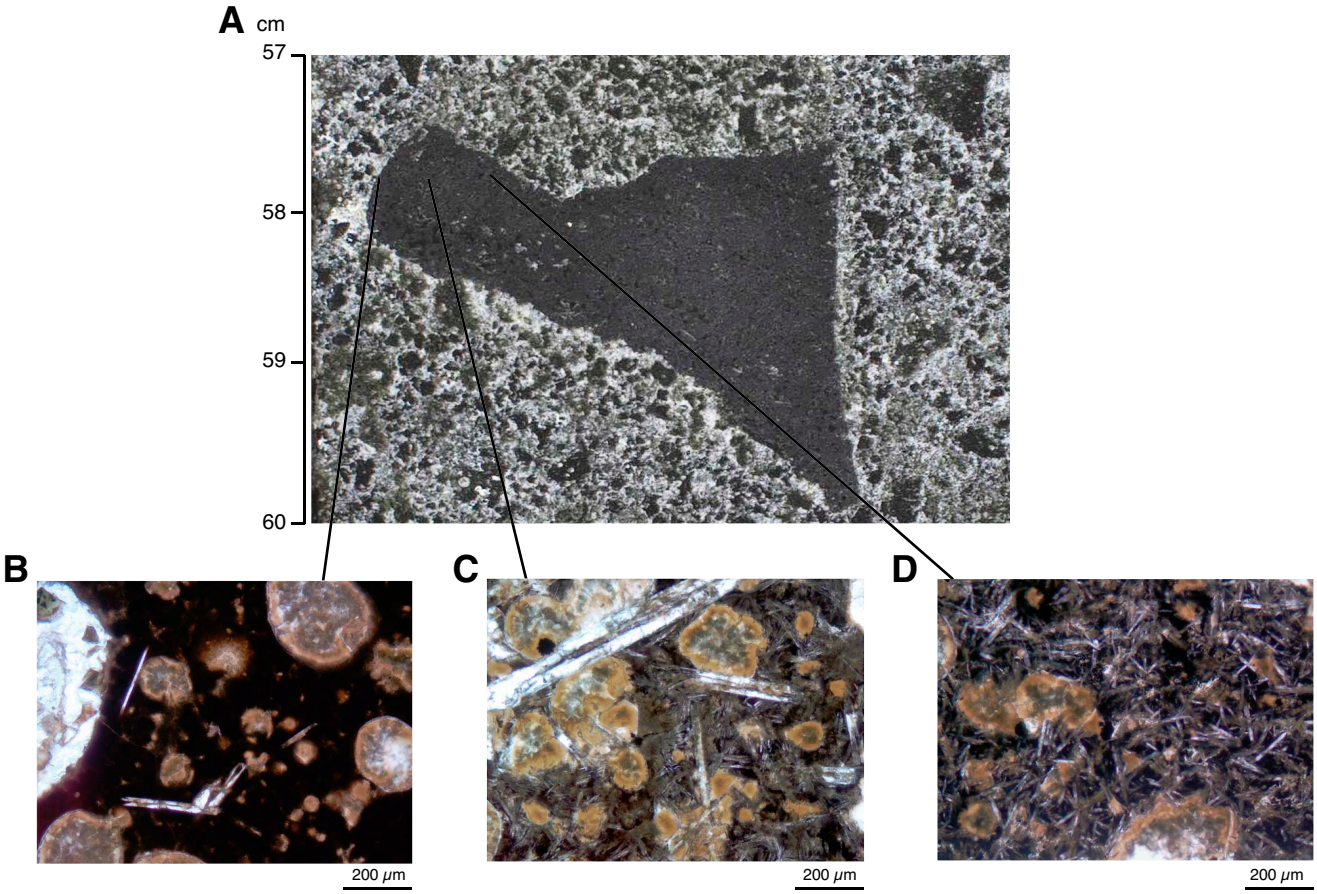

**Figure F38.** Thin section photomicrograph of a vitric clast altered to palagonite (pal) with a corona alteration of zeolite (zeo), Hole U1348A. The vitric clasts are cemented by calcite (cc) (Thin Section 165; Sample 324-U1348A-16R-2, 76–78 cm). Plane-polarized light.

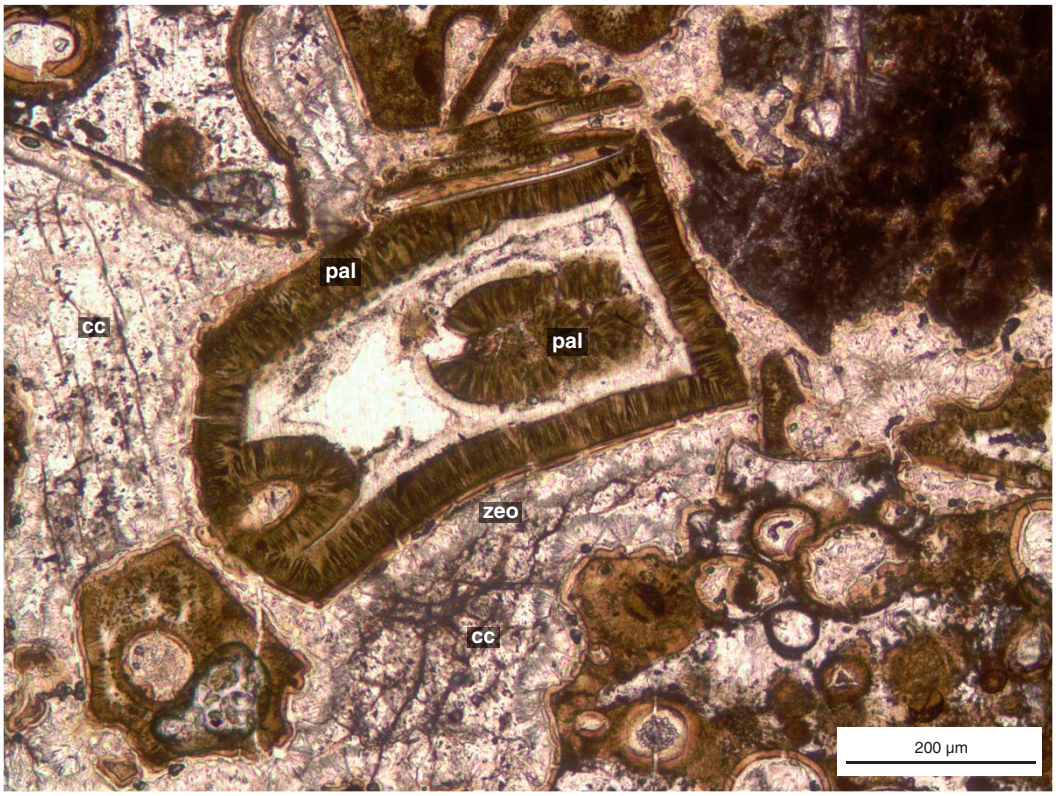

**Figure F39.** X-ray diffraction spectra of two volcaniclastic samples, (**A**) Sample 324-U1348A-20R-2, 36–39 cm, and (**B**) Sample 324-U1348A-15R-1, 95–96 cm, showing that secondary mineral assemblages are predominantly composed of calcite, phillipsite, montmorillonite, nontronite, and palygorskite, Hole U1348A.

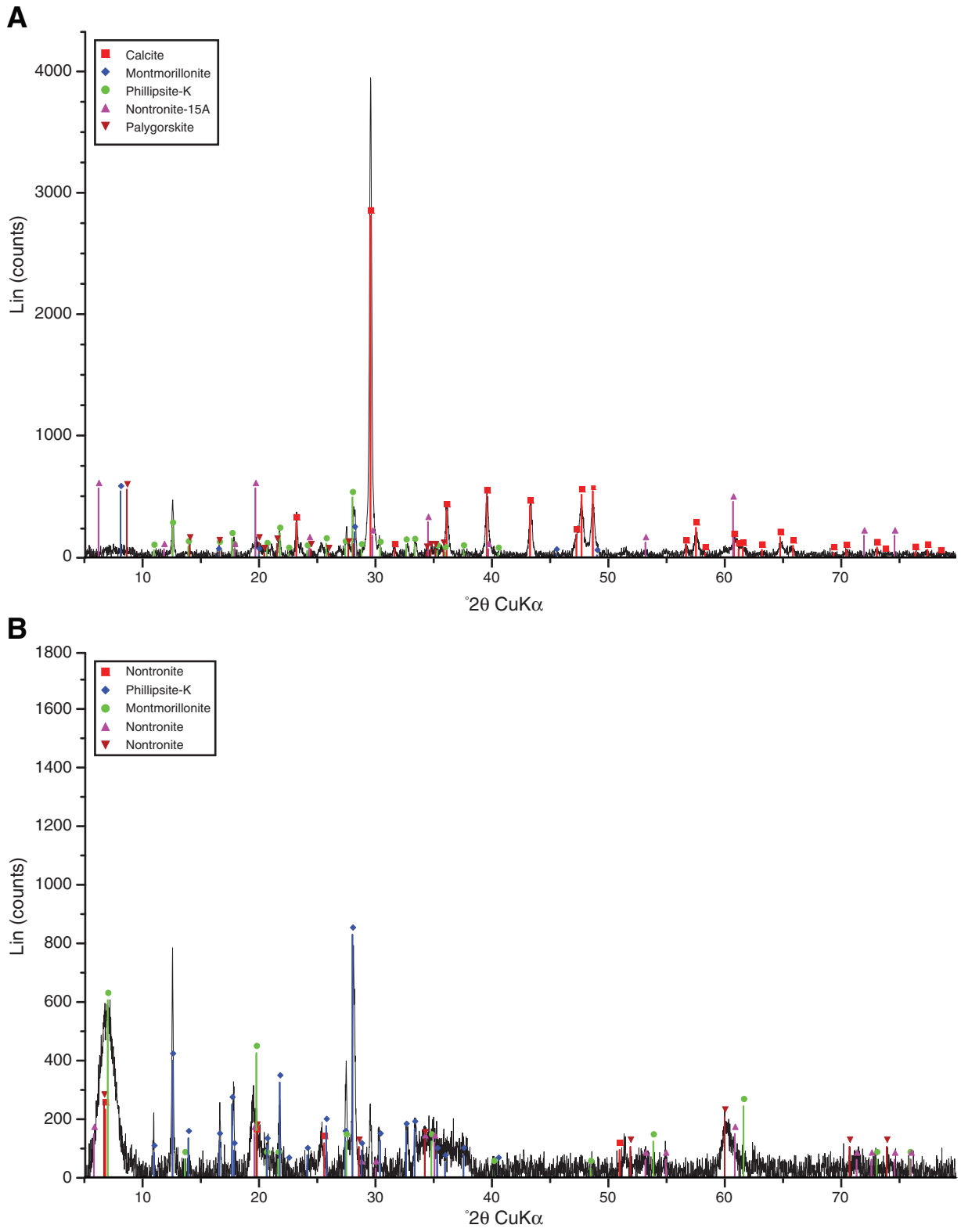

**Figure F40.** Thin section photomicrographs of vitric clasts altered to palagonite (pal) and cemented by calcite (cc), Hole U1348A. The inner parts of the vitric clasts are filled with zeolite (zeo) or calcite (Thin Section 169; Sample 324-U1348A-18R-3, 11–15 cm). (**A**) is under plane-polarized light and (**B**) is under cross-polarized light.

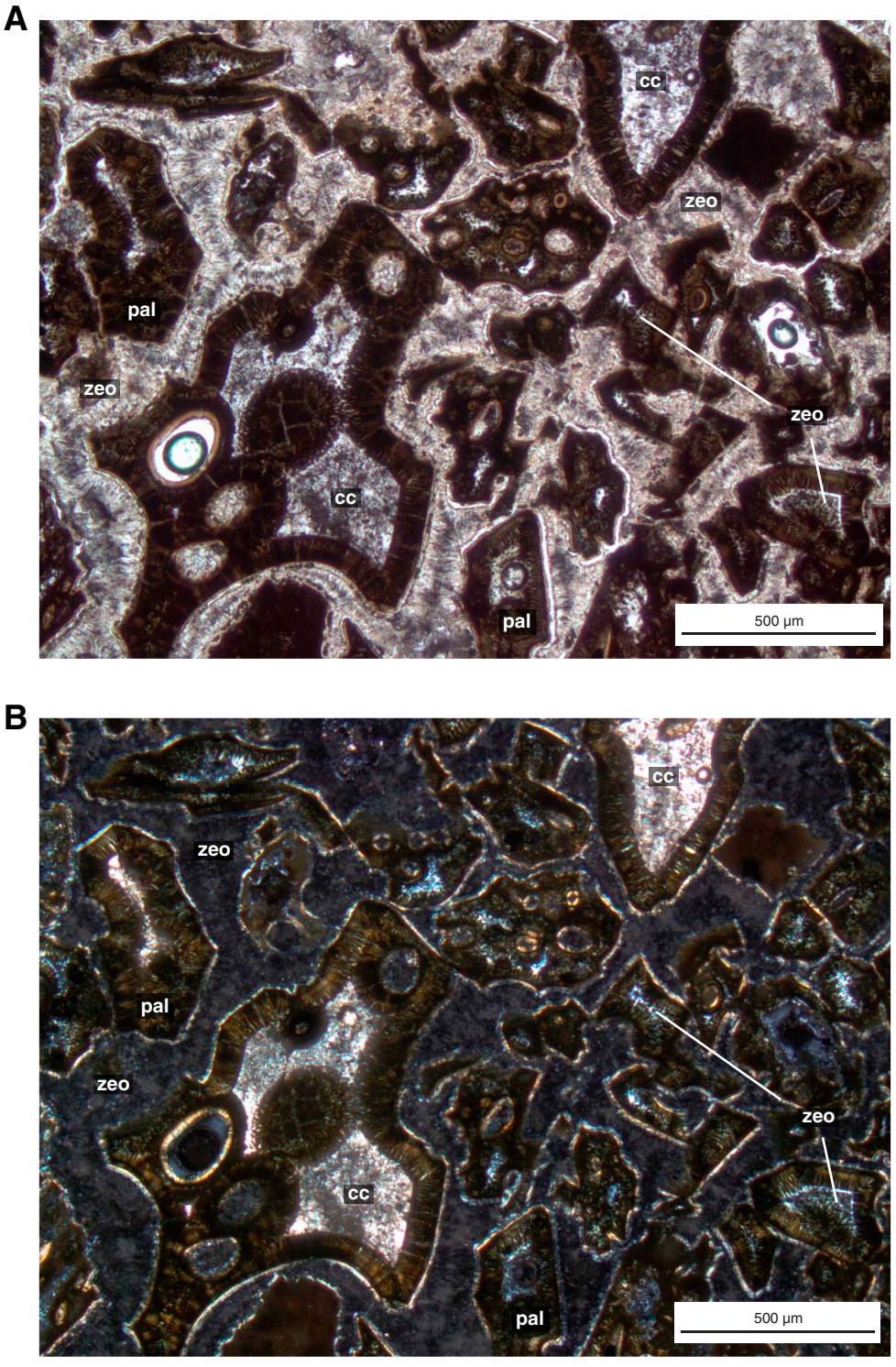

**Figure F41.** Photomicrograph of a basaltic clast, Hole U1348A. Alteration and mineralogy of this basaltic clast is similar to alteration of basaltic rocks recovered from top of Hole U1347A. The groundmass is highly altered to brown clays, whereas plagioclase microliths still remain relatively unaffected by alteration (Thin Section 158; Sample 324-U1348A-14R-3, 54–56 cm). Cross-polarized light.

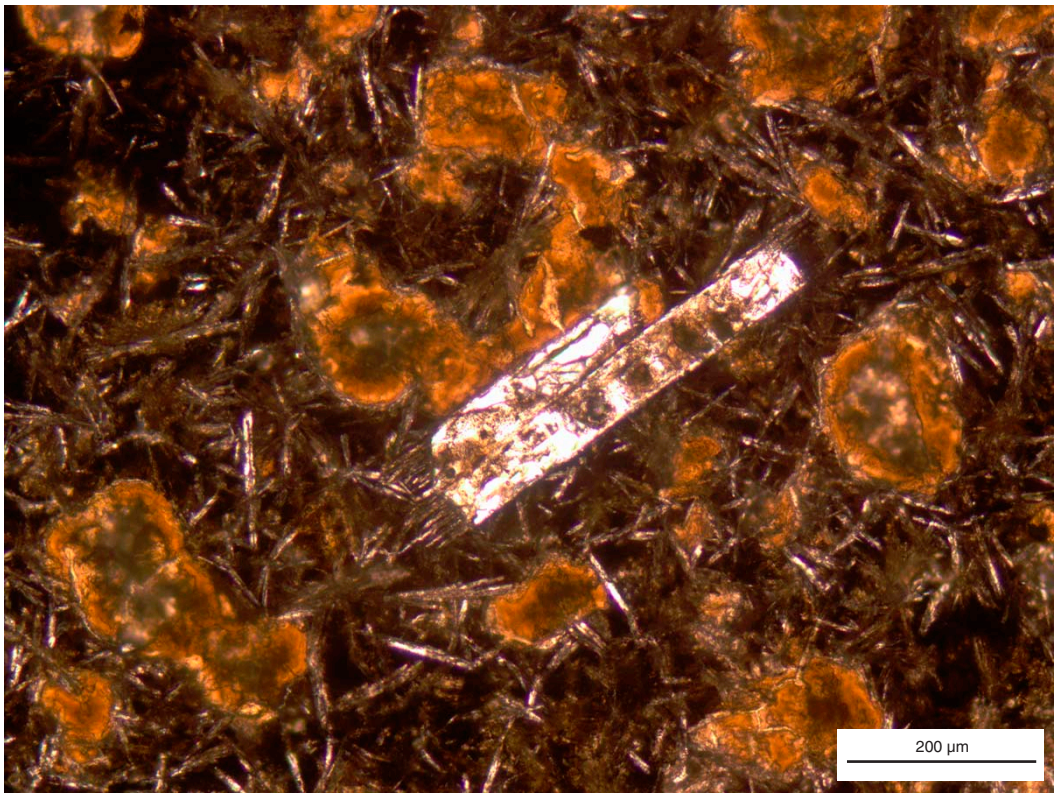

**Figure F42.** Thin section photomicrographs of zeolite (zeo; likely phillipsite) and calcite cement (cc) between vitric clasts altered to palagonite (pal), Hole U1348A (Thin Section 181; Sample 324-U1348A-22R-4, 84–87 cm). (**A**) is under plane-polarized light and (**B**) is under cross-polarized light.

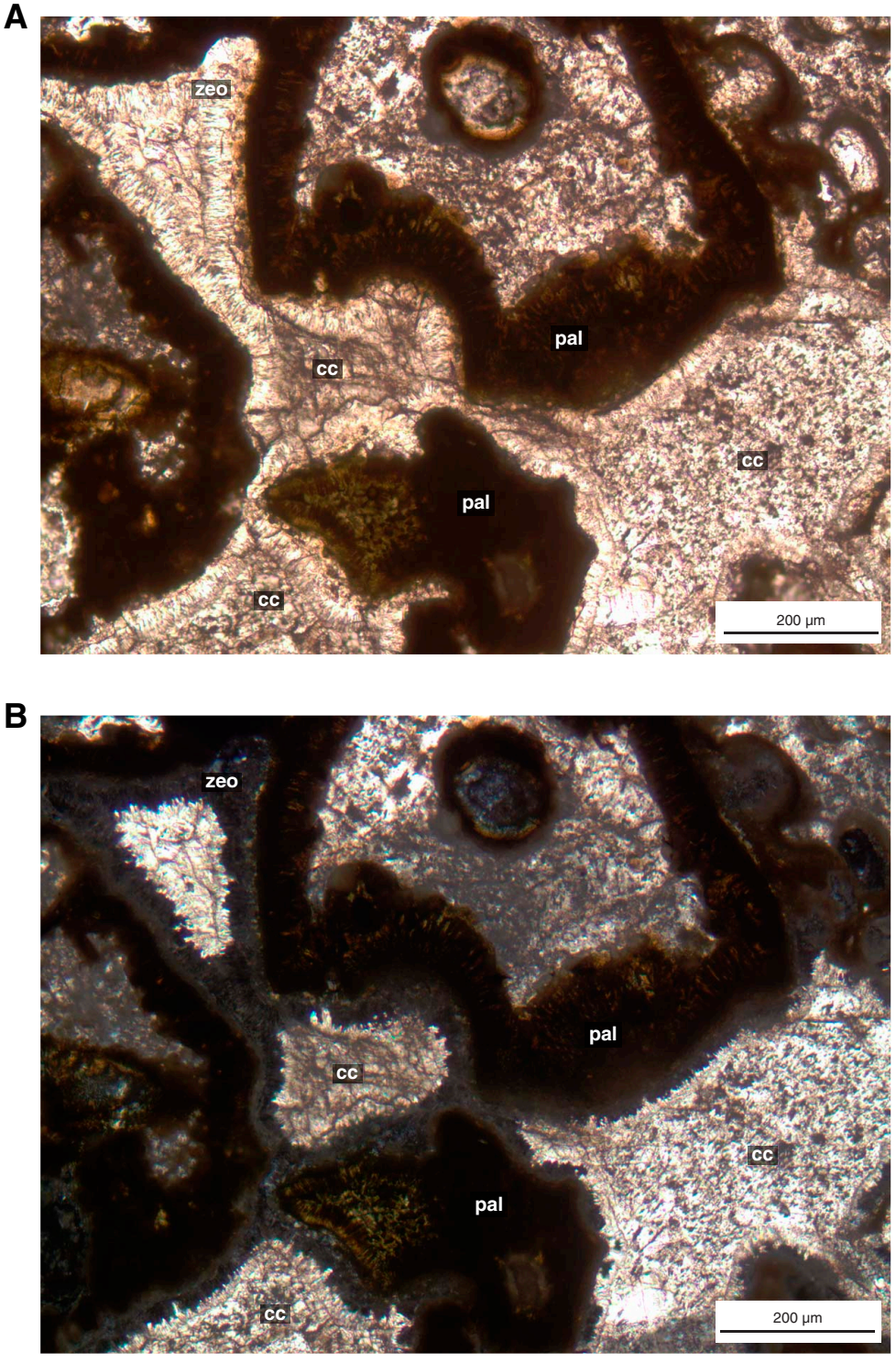

**Figure F43.** Downhole occurrences of secondary mineralogy, Hole U1348A.

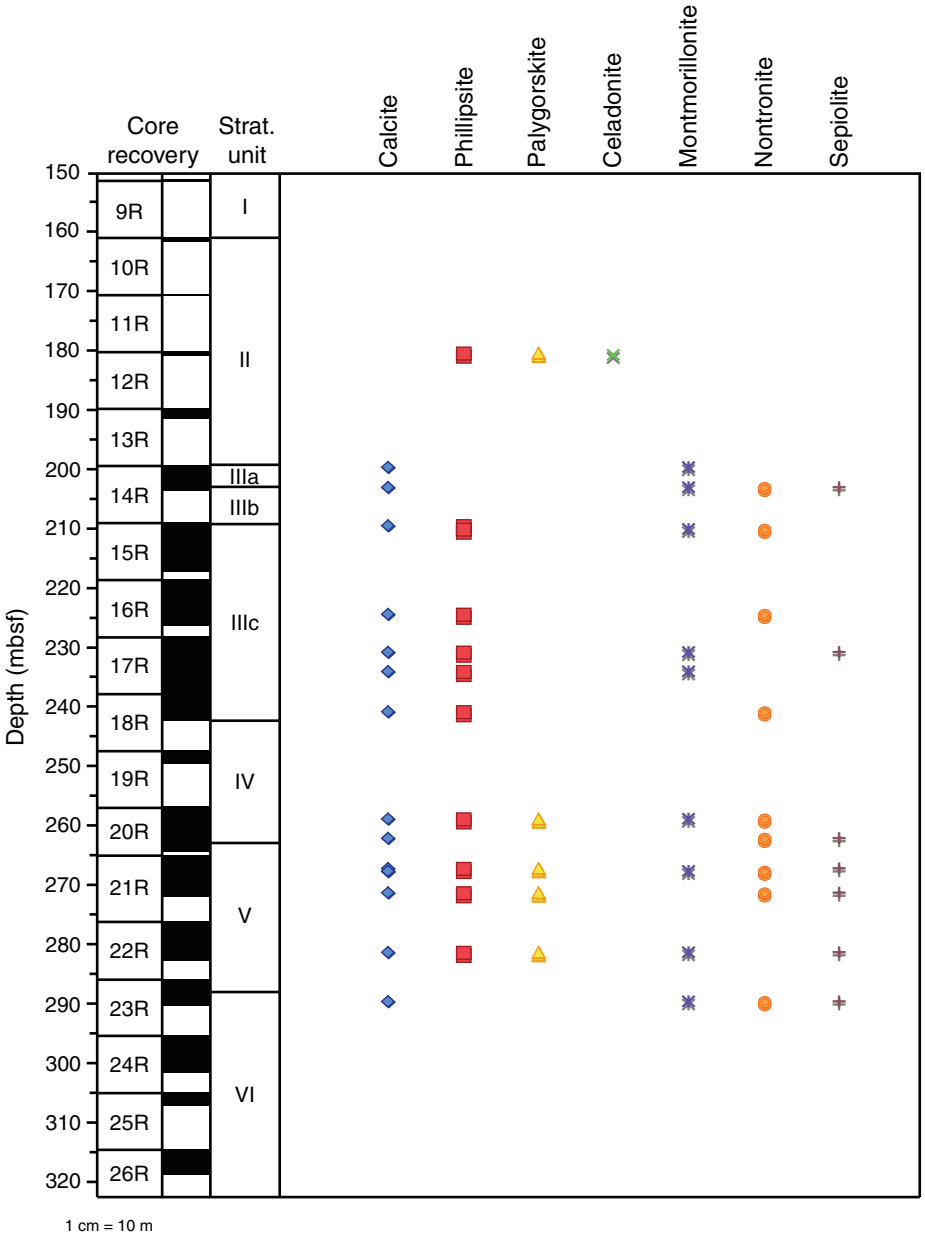

**Figure F44.** Thin section photomicrograph of corona reaction of zeolite (zeo) around palagonitic clast (pal), Hole U1348A (Thin Section 171; Sample 324-U1348A-19R-CC). phil = phillipsite. Plane-polarized light.

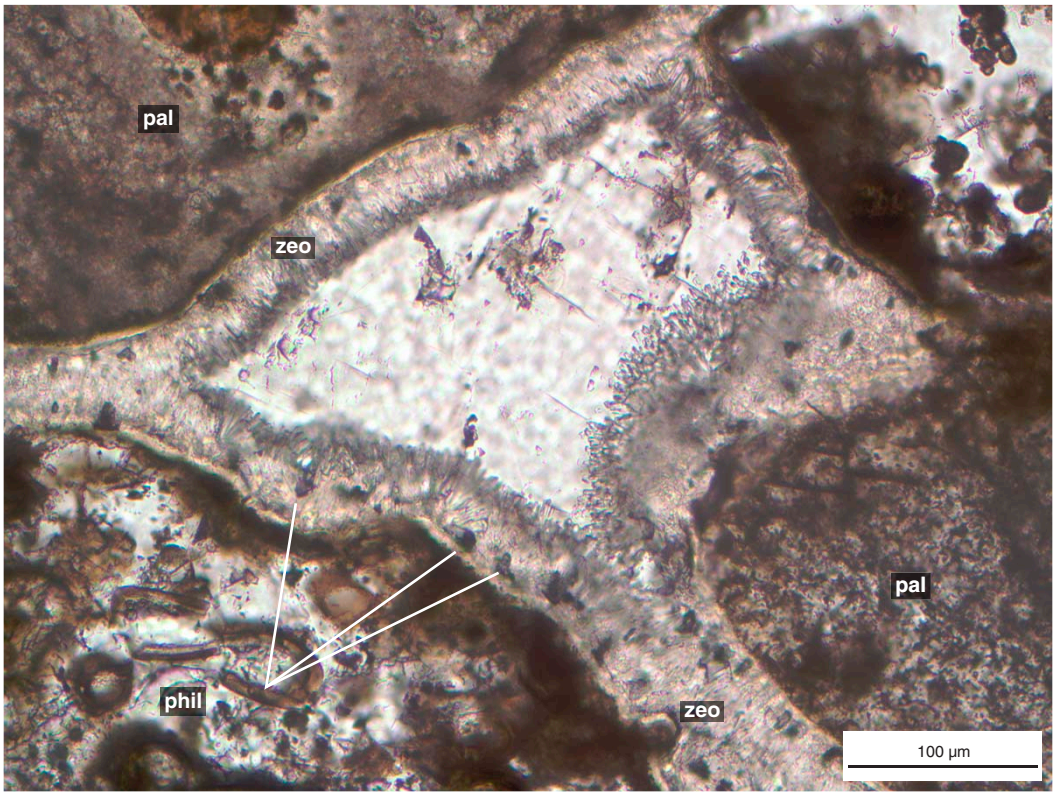

**Figure F45.** Sketch of volcaniclastic sediments showing relationship between bedding and en echelon veins, Hole U1348A (Section 324-U1348A-15R-1).

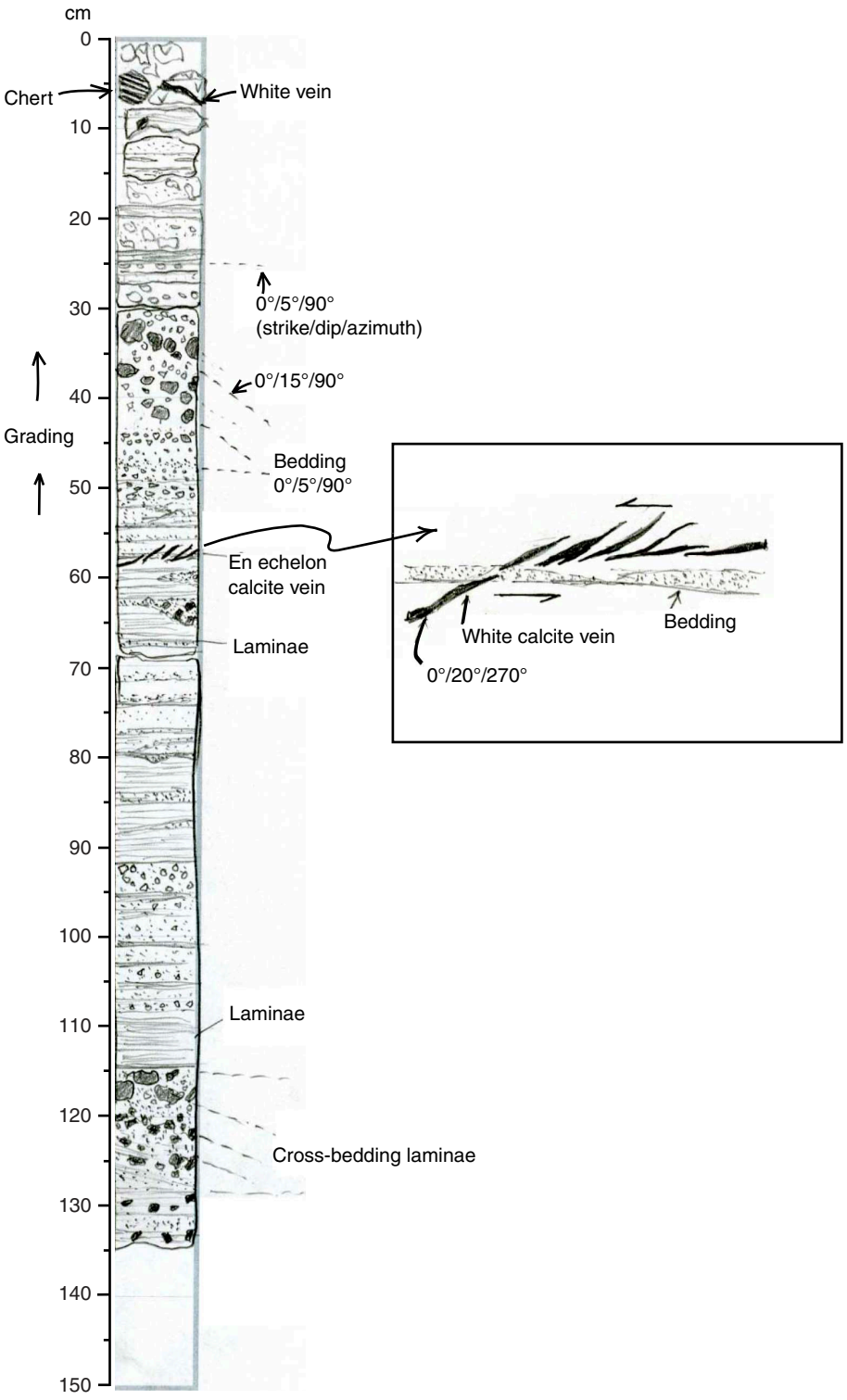

**Figure F46.** Rose diagrams of bedding dips showing variation of dip angles, Hole U1348A. All data recorded in the LIMS database.

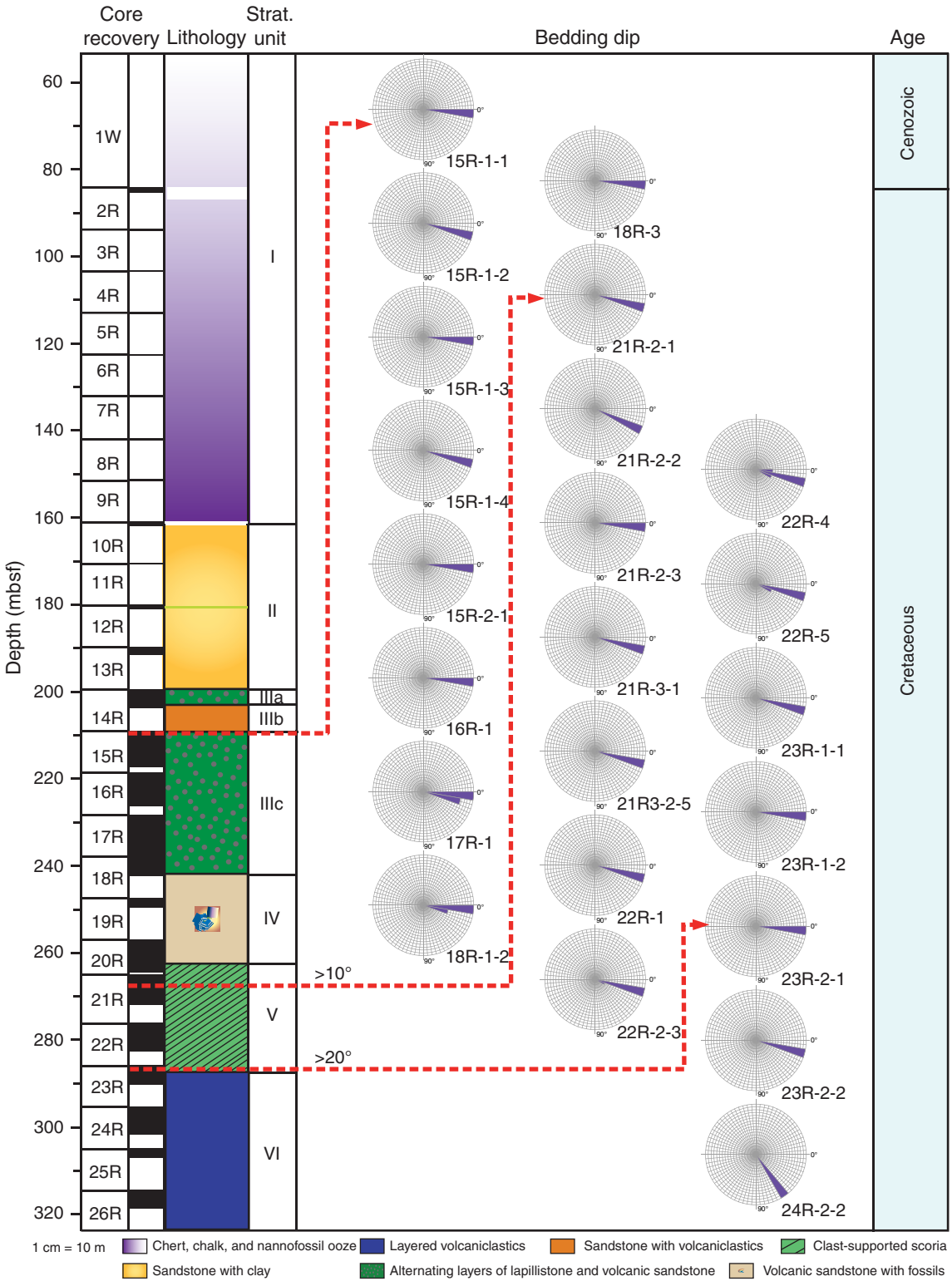

**Figure F47.** Sketch of massive volcaniclastics showing relationship between veins and beddings, Hole U1348A (Core 324-U1348A-26R).

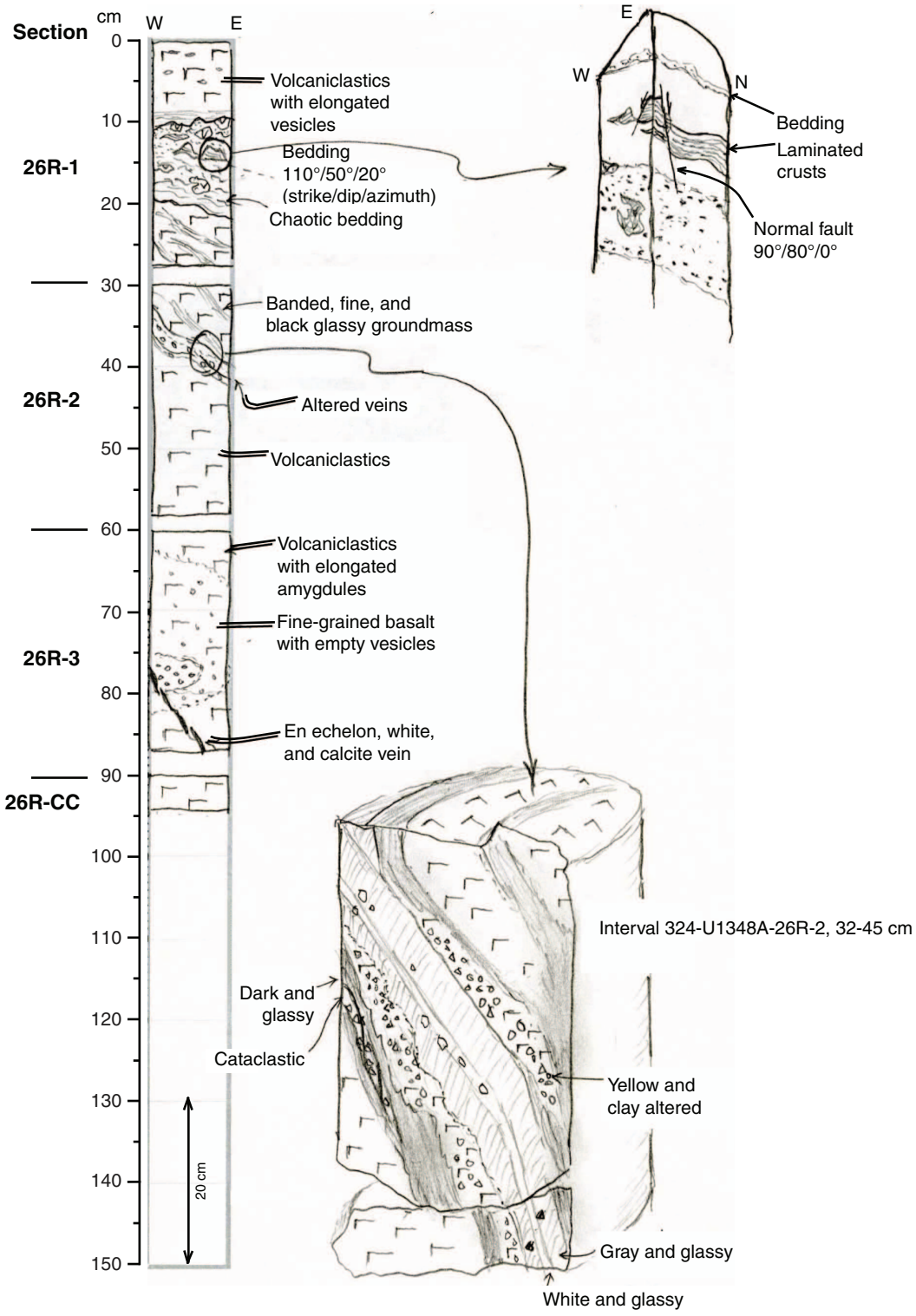

**Figure F48**. **A.** Core photograph of curved yellow veins filled with yellow clay and dark green slivers, Hole U1348A (interval 324-U1348A-18R-2, 70–118 cm). **B.** Core photograph of en echelon white veins filled with polycrystalline calcite (interval 324-U1348A-21R-5, 27–60 cm). **C.** Core photograph of en echelon white veins (interval 324-U1348A-15R-1, 58–62 cm). **D.** Core photograph of quartz vein cutting through chert bedding (interval 324-U1348A-5R-1, 8–13 cm). **E.** Rose diagram of vein dips. All data recorded in the LIMS database (iodp.tamu.edu/database/index.html).

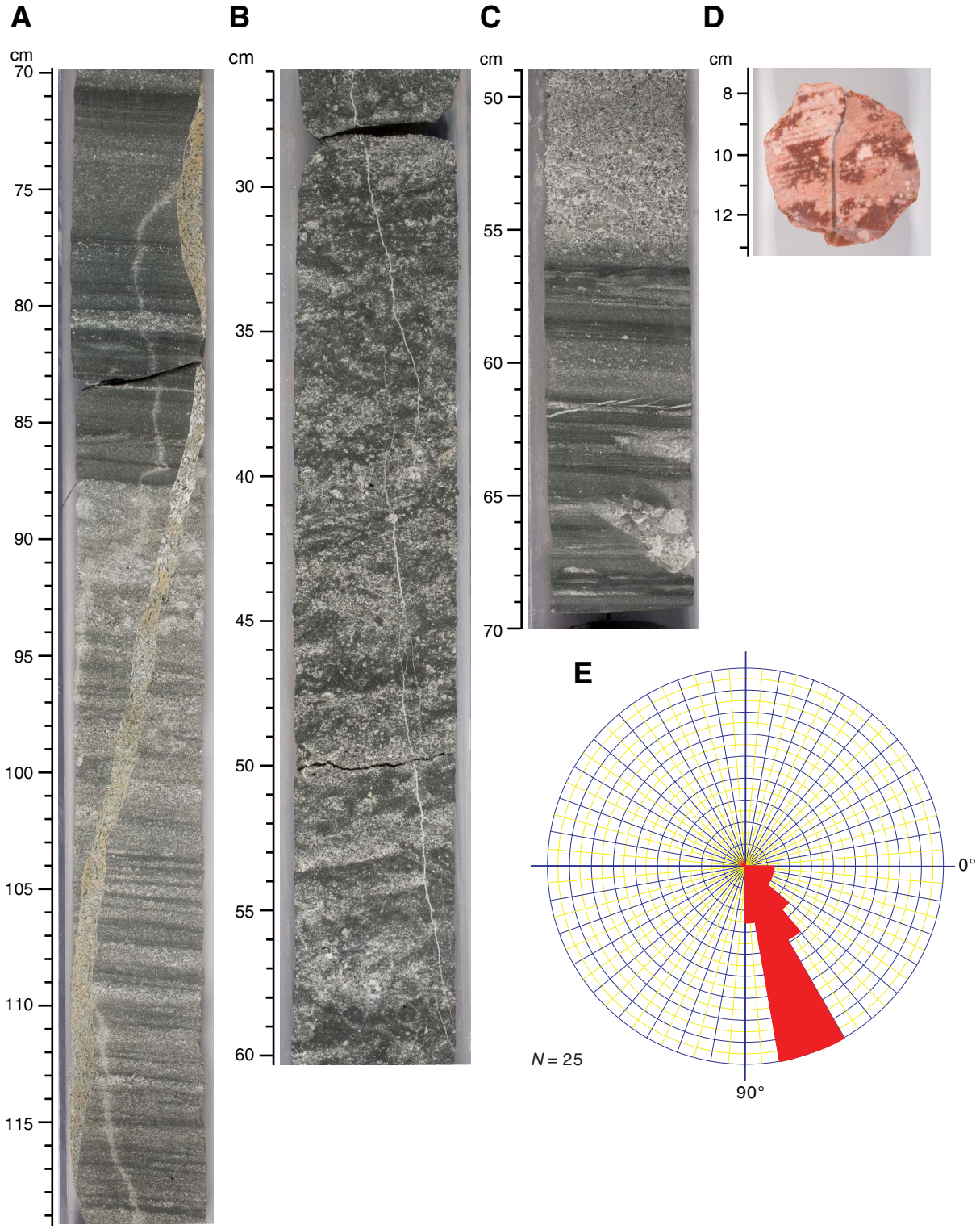

**Figure F49.** Plot of total alkalis vs. silica with Le Maitre et al.'s (1989) classification of volcanic rock types, Hole U1348A. Heavy dashed line = division of data for tholeiitic and alkalic lavas of Hawaii (Macdonald and Katsura, 1964; Macdonald, 1968). Values normalized to 100 wt% totals. OJP = Ontong Java Plateau (data of Tejada et al., 1996, 2002; Fitton and Godard, 2004), EPR = East Pacific Rise (data of Sinton et al., 1991; Bach et al., 1994; Mahoney et al., 1994), Nazca-ESC = Nazca Ridge and Easter Seamount Chain (data of Ray et al., submitted).

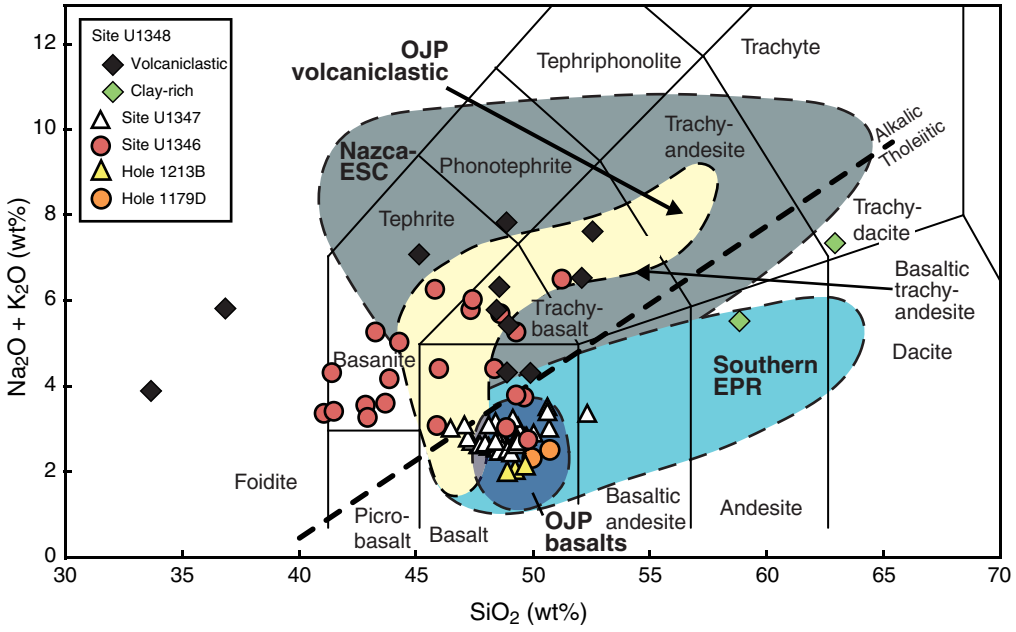

**Figure F50.** Plot of $TiO_2$ vs. (**A**) LOI, (**B**) $Fe_2O_3^T$ (total iron calculated as $Fe_2O_3$), (**C**) $P_2O_5$, and (**D**) Zr, Hole U1348A. OJP = Ontong Java Plateau (data of Tejada et al., 1996, 2002; Fitton and Godard, 2004), EPR = East Pacific Rise (data of Sinton et al., 1991; Bach et al., 1994; Mahoney et al., 1994), Nazca-ESC = Nazca Ridge and Easter Seamount Chain (data of Ray et al., submitted). The two low-$TiO_2$ Site U1346 data points are for samples of carbonate-rich veins (see **"Geochemistry"** in the "Site U1346" chapter).

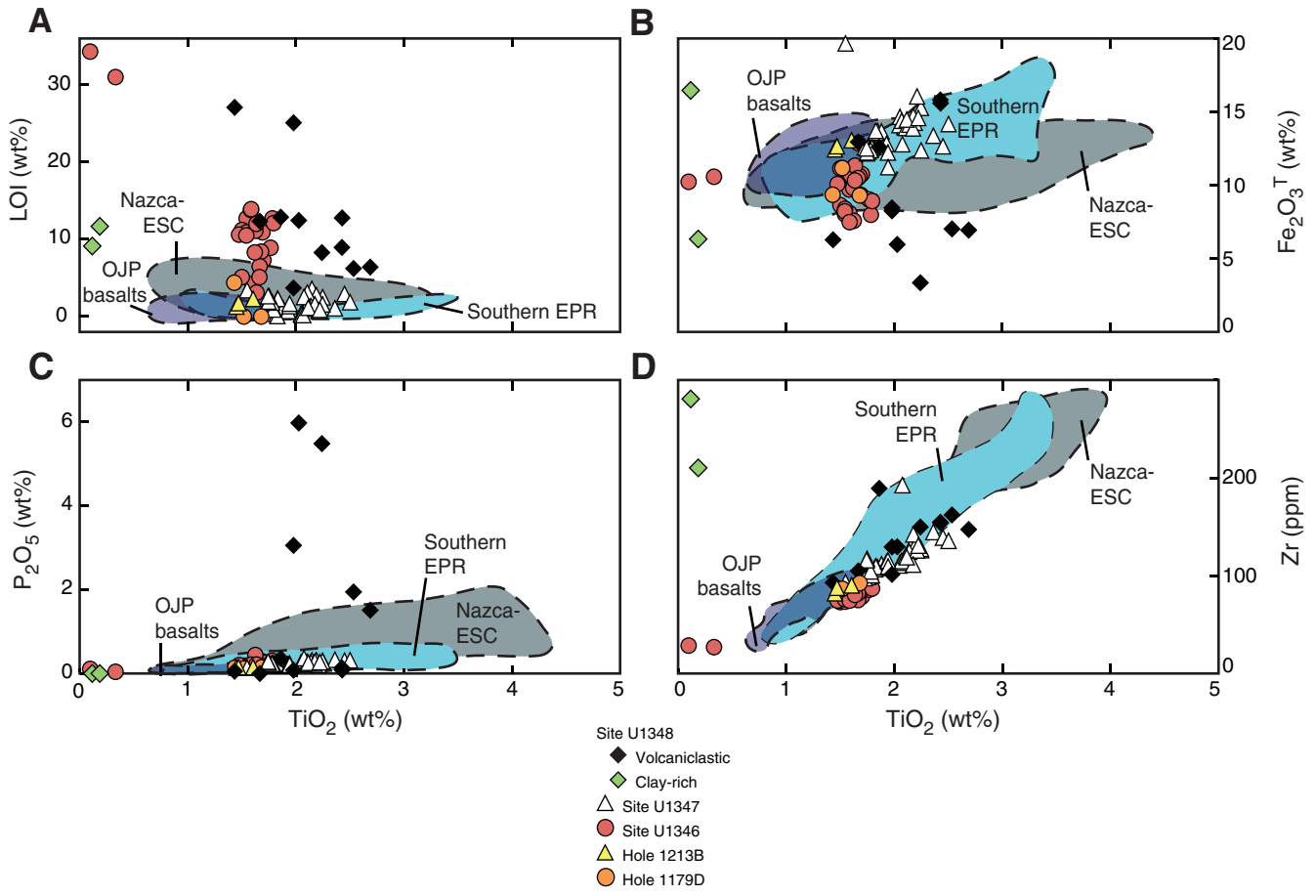

**Figure F51.** Plots of $P_2O_5$ vs. (**A**) Y and (**B**) Sr for Site U1348 volcaniclastic samples.

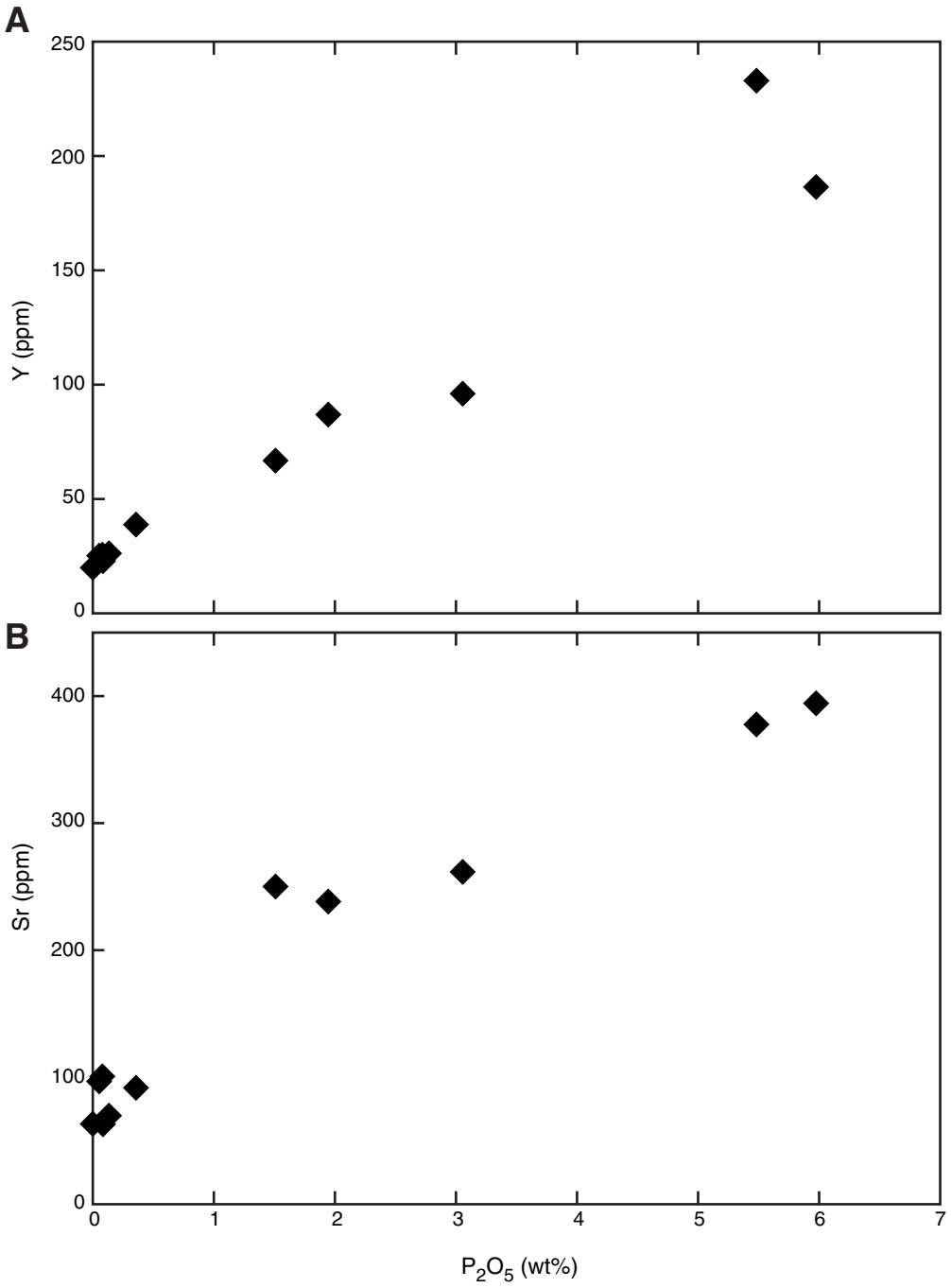

**Figure F52.** Whole-round physical property data summary, Hole U1348A. Shaded regions correspond to lithology (green = volcaniclastic, yellow = sandstone, blue = volcaniclastic breccia). For a full lithologic description of the units, see **"Sedimentology."** For more details about data filtering, see **"Physical properties"** in the "Methods" chapter. MS = magnetic susceptibility, GRA = gamma ray attenuation, NGR = natural gamma radiation.

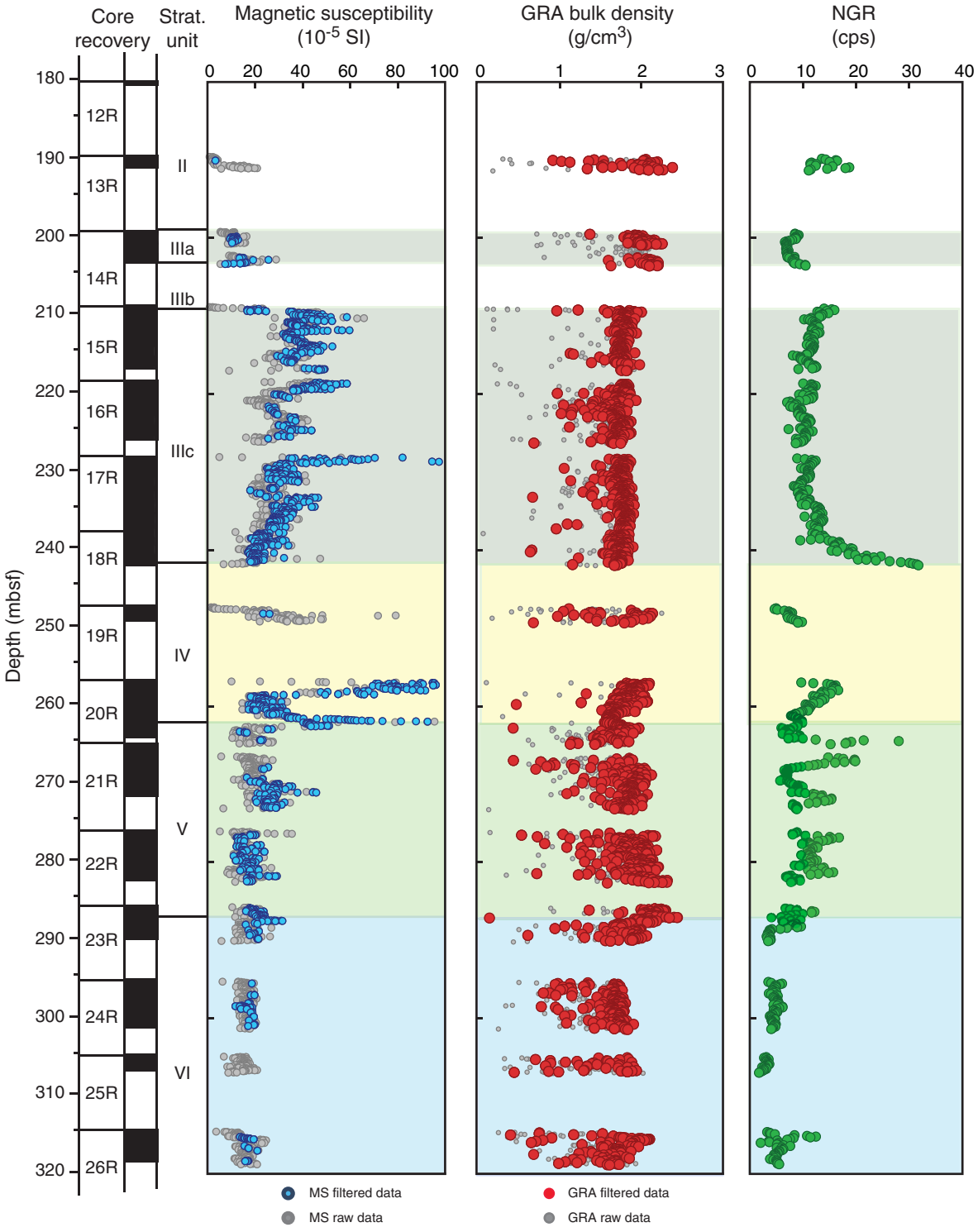

**Figure F53.** Selected discrete sample measurements, Hole U1348A.

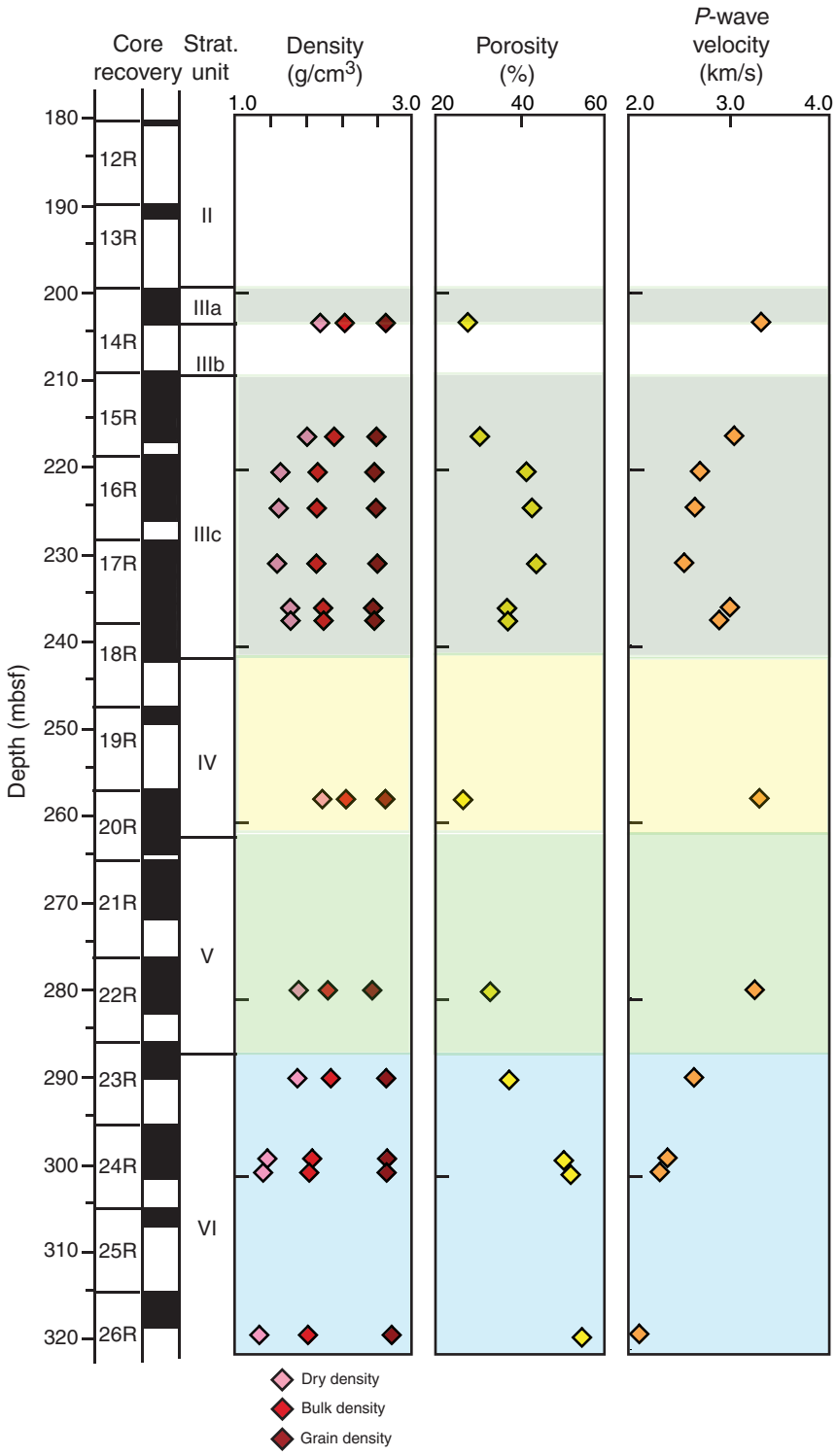

**Figure F54.** Plots of *P*-wave velocity vs. (**A**) bulk density and (**B**) porosity, Hole U1348A.

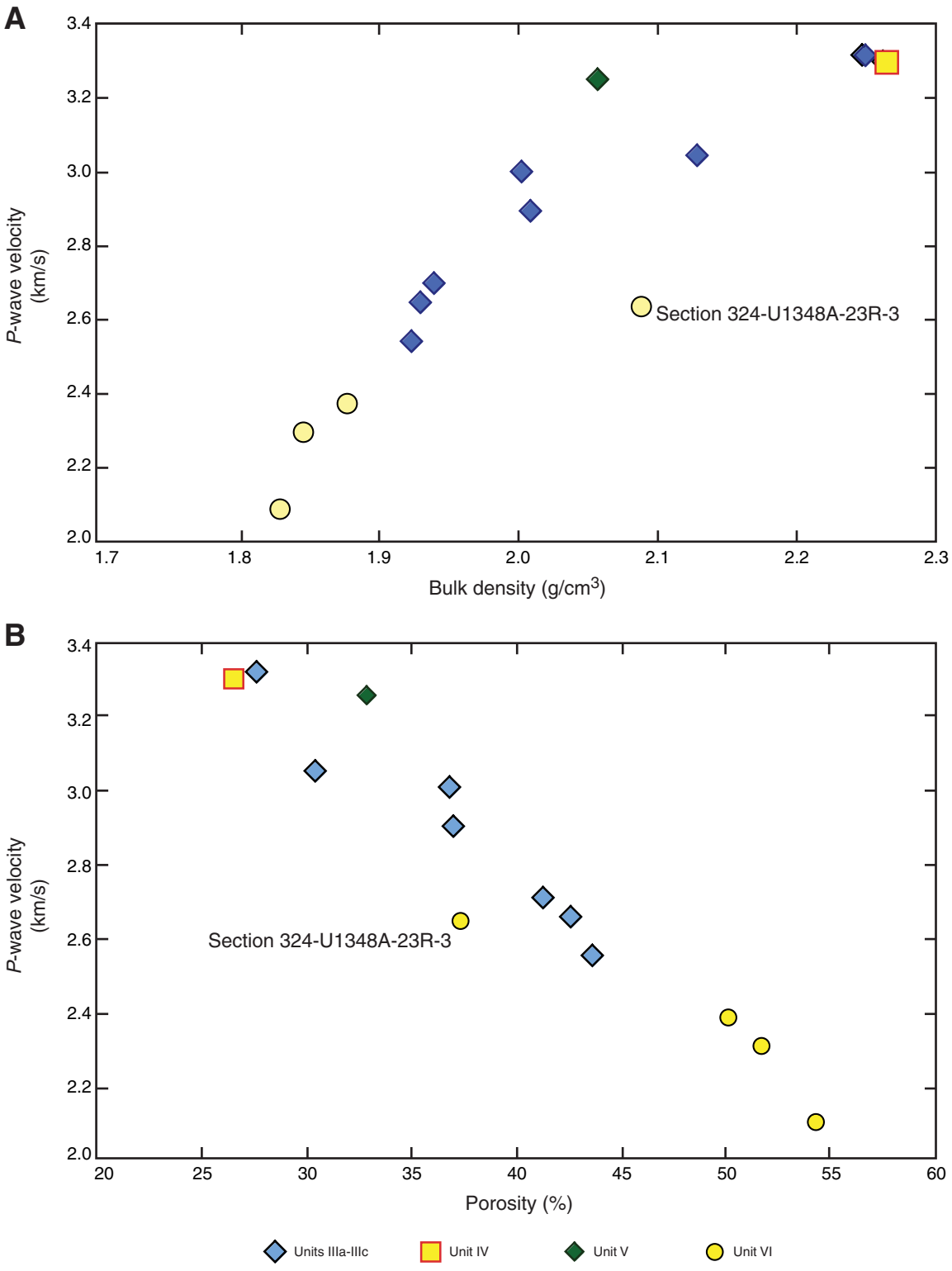

**Figure F55.** Example of a demagnetization spectrum, Hole U1348A (Sample 324-U1348A-17R-7, 3–5 cm).

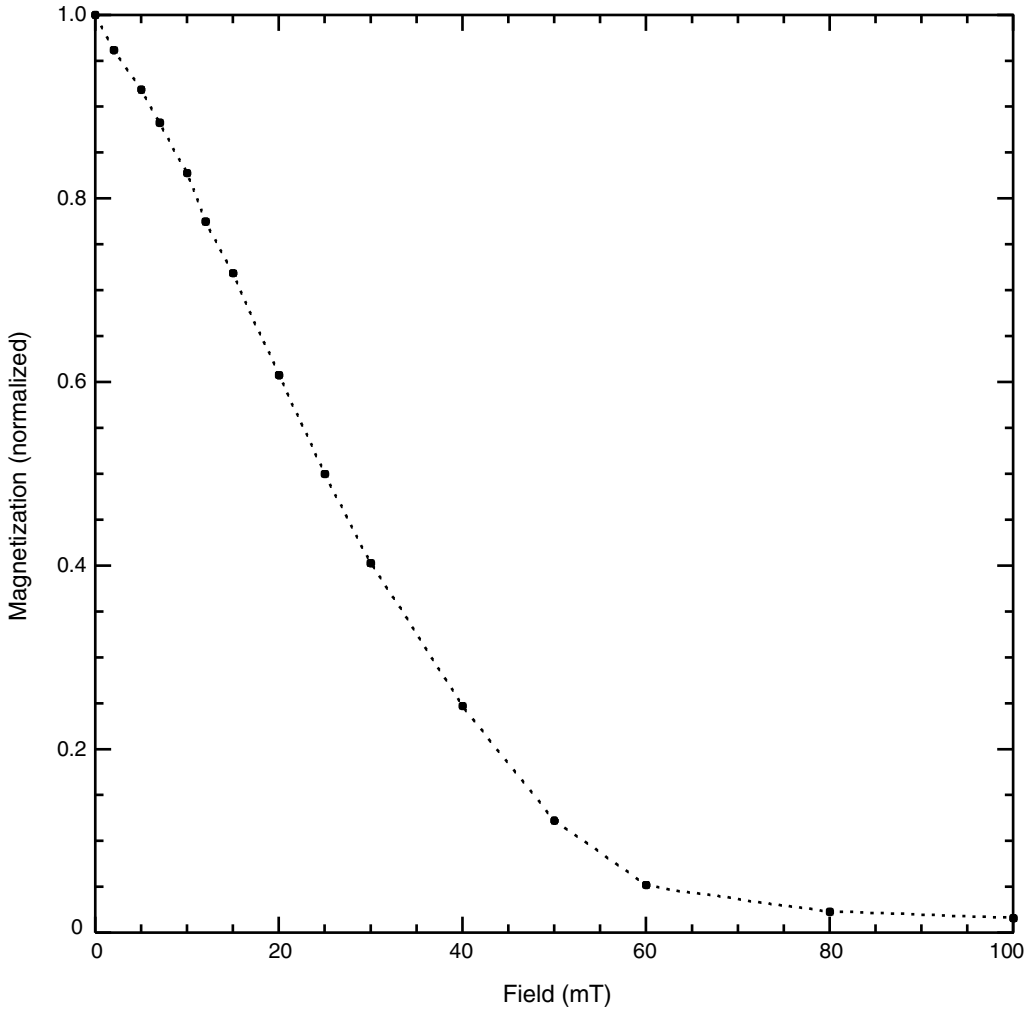

**Figure F56.** Downhole hole deviation, magnetic inclination, total magnetic field moment, and magnetic intensity, Hole U1348A. $F_x$, $F_y$, $F_z$ = *x*-, *y*-, and *z*-axis measurements. DEVI = hole deviation, FINC = magnetic field inclination, FNOR = magnetic field total moment.

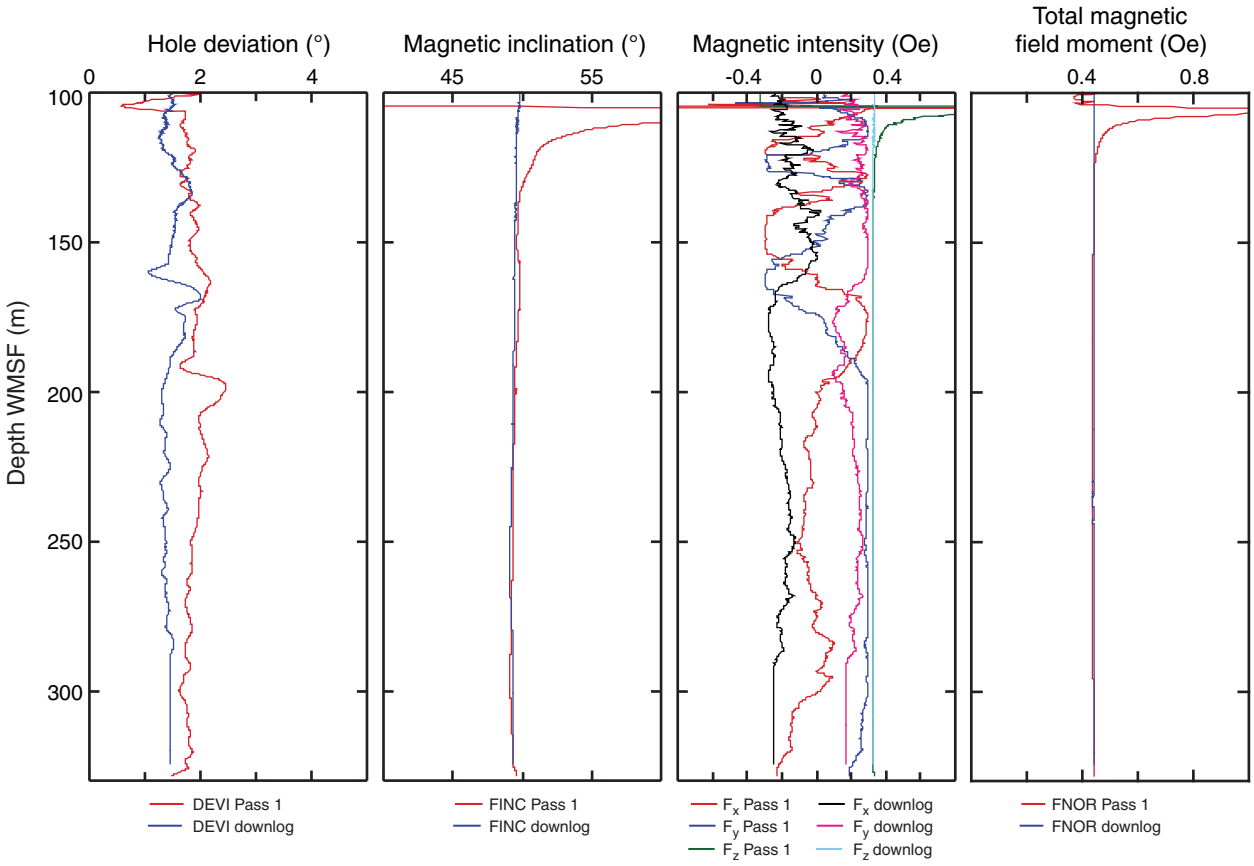

**Figure F57.** Formation MicroScanner images of (**A**) subhorizontal layering, (**B**) vesicular or brecciated textures, and (**C**) dipping beds in Hole U1348A.

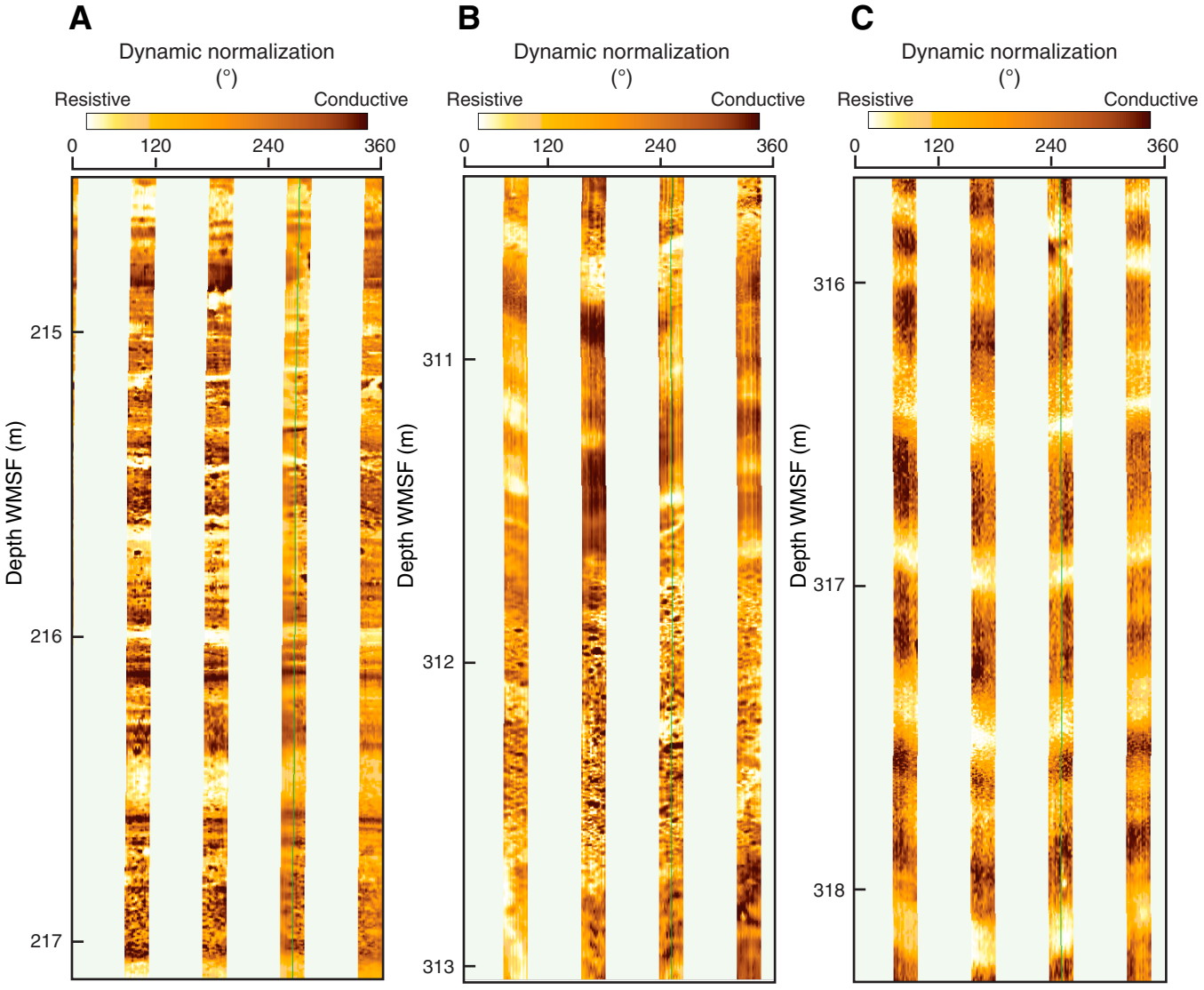

**Figure F58.** Formation MicroScanner image of dipping beds in the lower section of Hole U1348A. Preliminary structural analysis of this interval shows contacts striking northeast to southwest with southeast-oriented dips from 25° to 30°. A comparison of Section 324-U1348A-23R-1 shows similar structures in the core. Color levels on the core photograph were adjusted in order to accentuate the layering and contact.

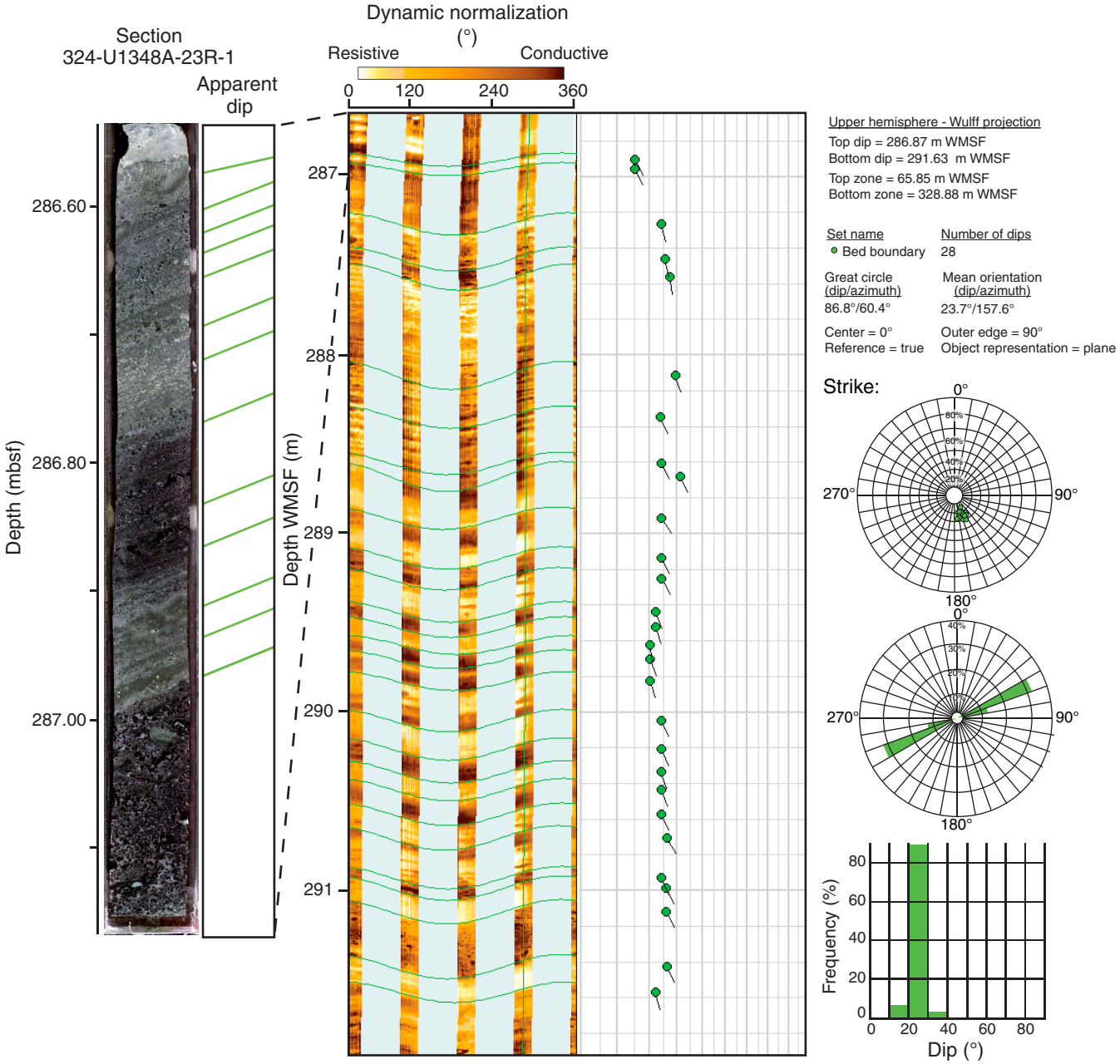

**Table T1.** Coring summary, Site U1348. (See table notes.)

**Site U1348**
Time on site (h): 113.5 (1245 h, 3 October–0845 h, 7 October 2009)
**Hole U1348A**
Latitude: 34°24.940′N
Longitude: 159°22.907′E
Time on hole (h): 113.5 (1245 h, 3 October–0845 h, 7 October 2009)
Seafloor (drill pipe measured below rig floor, m DRF): 3275.0
Distance between rig floor and sea level (m): 11
Water depth (drill pipe measured from sea level, mbsl): 3264
Total depth (drill pipe measured from rig floor, m DRF): 3599.1
Total penetration (drilling depth below seafloor, m DSF): 324.1
Total length of cored section (m): 239.9
Total core recovered (m): 80.91
Core recovery (%): 33.7
Total number of cores: 26

| Core | Depth DSF (m) Top of cored interval | Depth DSF (m) Bottom of cored interval | Interval advanced (m) | Length of core recovered (m) | Recovery (%) |
|---|---|---|---|---|---|
| 324-U1348A- | | | | | |
| 1W | 0.0 | 84.2 | 84.2 | 0.10 | 0 |
| 2R | 84.2 | 93.8 | 9.6 | 1.38 | 14 |
| 3R | 93.8 | 103.4 | 9.6 | 0.05 | 1 |
| 4R | 103.4 | 113.0 | 9.6 | 0.03 | 0 |
| 5R | 113.0 | 122.6 | 9.6 | 0.13 | 1 |
| 6R | 122.6 | 132.2 | 9.6 | 0.08 | 1 |
| 7R | 132.2 | 141.9 | 9.7 | 0.21 | 2 |
| 8R | 141.9 | 151.5 | 9.6 | 0.25 | 3 |
| 9R | 151.5 | 161.1 | 9.6 | 0.20 | 2 |
| 10R | 161.1 | 170.7 | 9.6 | 0.68 | 7 |
| 11R | 170.7 | 180.3 | 9.6 | 0.09 | 1 |
| 12R | 180.3 | 189.9 | 9.6 | 0.61 | 6 |
| 13R | 189.9 | 199.5 | 9.6 | 1.67 | 17 |
| 14R | 199.5 | 209.1 | 9.6 | 4.35 | 45 |
| 15R | 209.1 | 218.7 | 9.6 | 8.15 | 85 |
| 16R | 218.7 | 228.3 | 9.6 | 7.88 | 82 |
| 17R | 228.3 | 237.9 | 9.6 | 9.43 | 98 |
| 18R | 237.9 | 247.5 | 9.6 | 4.40 | 46 |
| 19R | 247.5 | 257.0 | 9.5 | 2.07 | 22 |
| 20R | 257.0 | 266.6 | 9.6 | 8.23 | 86 |
| 21R | 266.6 | 276.2 | 9.6 | 6.94 | 72 |
| 22R | 276.2 | 285.9 | 9.7 | 6.65 | 69 |
| 23R | 285.9 | 295.4 | 9.5 | 4.48 | 47 |
| 24R | 295.4 | 305.0 | 9.6 | 6.27 | 65 |
| 25R | 305.0 | 314.6 | 9.6 | 2.26 | 24 |
| 26R | 314.6 | 324.1 | 9.5 | 4.42 | 47 |
| | | Totals: | 324.1 | 81.01 | 25 |
| | Totals without wash barrel: | | 239.9 | 80.91 | 33.7 |

Notes: DRF = drilling depth below rig floor, DSF = drilling depth below seafloor. Local time = UTC + 10 h.

**Table T2.** Calcareous nannofossil age assignments for Unit I, Site U1348. (See table notes.)

| Core, section, interval (cm) | Age-diagnostic species (Abundance) | Stratigraphic range (Zone) | Age (Ma) |
|---|---|---|---|
| 324-U1348A- | | | |
| 1W-1, 0–6 | *Discoaster broweri* (F) | Miocene–Pleistocene (NN8–NN19) | 16.4–14.7 (?) |
| | *Discoaster challengeri* (C) | Miocene (NN8–NN16/CN12b) | |
| | *Discoaster deflandrei* (F) | Eocene–Miocene (NN5–NN10) | |
| | *Discoaster druggii* (?) (F) | Miocene (NN2–NN6) | |
| | *Reticulofenestra pseudoumbilicus* (C) | Miocene–Pliocene (CN4/NN4–NN15) | |
| | *Uniplanarius gothicus* (R) | Campanian–Maastrichtian (CC17–CC24) | |
| 2R-1, 1* | *Amaurolithus delicatus* (R) | Miocene–Pliocene (NN/NP11–NN/NP14) | 14–11.19 |
| | *Calcidiscus macintyrei* (C) | Miocene–Pleistocene (NN4–NN19) | |
| | *Discoaster challengeri* (C) | Miocene (NN8–NN16/CN12b) | |
| | *Discoaster broweri* (F) | Miocene–Pleistocene (NN8–NN19) | |
| 2R-1, 2 | *Calcidiscus macintyrei* (C) | Miocene–Pleistocene (NN4–NN19) | 16.4 (?)–9.82 |
| | *Discoaster challengeri* (C) | Miocene–Pliocene (NN8–NN16/CN12b) | |
| | *Discoaster broweri* (F) | Miocene–Pleistocene (NN8–NN19) | |
| | *Discoaster druggii (?)* (F) | Miocene (NN2–NN6) | |
| 2R-1, 6* | *Discoaster pentaradiatus* (R) | Miocene–Pliocene (NN9/CN7–NN18) | 15.1–8.58 |
| | *Discoaster challengeri* (F) | Miocene (NN8–NN16/CN12b) | |
| | *Discoaster broweri* (C) | Miocene–Pleistocene (NN8–NN19) | |
| | *Calcidiscus macintyrei* (C) | Miocene–Pleistocene (NN4–NN19) | |
| 2R-1, 6† | *Uniplanarius gothicus* (R) | Campanian–Maastrichtian (CC17–CC24) | 89.3–87.2 |
| | *Arkhangelskiella cybiformis* (R) | Santonian–Campanian (UC13) | |
| | *Cretarhabdus striatus* (R) | Aptian–Cenomanian (?–UC4) | |
| 2R-1, 60 | *Uniplanarius gothicus* (R) | Campanian–Maastrichtian (CC17–CC24) | 84–69.6 |
| | *Reinhardites levis* (R) | late Campanian–Maastrichtian (?–CC25/UC19) | |
| 2R-1, 91 | *Micula decussata* (R) | Coniacian–Maastrichtian (CC14–CC27) | 87.2–69.2 |
| | *Lithraphidites decoratus* (R) | Albian–Maastrichtian (CC9–CC25) | |
| 2R-1, 94.5 | *Micula decussata* (R) | Coniacian–Maasstrichtian (CC14–CC27) | 77–69.6 |
| | *Uniplanarius sissinghii* (R) | Campanian–Maastrichtian (CC21–CC24) | |
| 2R-1, 95 | *Uniplanarius gothicus* (R) | Campanian–Maastrichtian (CC17–CC24) | 77–69.6 |
| | *Micula decussata* (R) | Coniacian–Maasstrichtian (CC14–CC27) | |
| | *Uniplanarius sissinghii* (R) | Campanian–Maastrichtian (CC21–CC24) | |
| 2R-CC, 12–15 | *Micula staurophora* (R) | Coniacian–Maastrichtian (UC10–NP1) | 85.5–75.5 |
| | *Lithrastrinus grillii* (R) | Santonian–Campanian (UC11–CC22b) | |
| | *Microrhabdulus decoratus* (R) | Cenomanian–Maastrichtian (CC10/UC3–top CC26) | |
| 4R-1, 0–1 | *Micula decussata* (R) | Coniacian–Maastrichtian (CC14–CC27) | 84.8–83.4 |
| | *Zeugrhabdotus bicrescenticus* (F) | Albian–Maastrichtian (?) | |
| | *Eprolithus floralis* (C) | Aptian–Santonian (NC7a–CC16) | |
| | *Uniplanarius gothicus* (R) | Campanian–Maastrichtian (CC17–CC24) | |
| 7R-1, 6–7 | *Eprolithus floralis* (C) | Aptian–Santonian (NC7a–CC16) | 119.5–84 |
| 9R-1, 19–20 | *Rhagodiscus robustus* (R) | Barremian–Albian (NC5–NC10a) | 121.1–99.1 |
| | *Cretarhabdus striatus* (R) | Aptian–Cenomanian (?–UC4) | |
| 9R-1, 57–60 | *Eprolithus floralis* (C) | Aptian–Santonian (NC7a–CC16) | 119.5–84 |
| 10R-1, 1 | *Eprolithus floralis* (R) | Aptian–Santonian (NC7a–CC16) | 119.5–84 |
| 10R-1, 17 | *Eprolithus floralis* (R) | Aptian–Santonian (NC7a–CC16) | 119.5–84 |
| 10R-1, 20–21 | *Eprolithus floralis* (R) | Aptian–Santonian (NC7a–CC16) | 119.5–84 |

Notes: * = gray sediment, † = white sediment. Abundance: C = common, F = frequent, R = rare. Zone ranges are only given for properly defined taxa.

**Table T3.** Planktonic foraminifer preservation, abundance, and age assignments for Unit I, Site U1348. (See table notes.)

| Core, section, interval (cm) | Depth (mbsf) | Size fraction (µm) | Preservation | *Contusotruncana fornicata* | *Dicarinella asymetrica* | *Globigerinelloides ultramicrus* | *Globotruncana arca* | *Globotruncana linneiana* | *Globotruncanita elevata* | *Globotruncanita stuartiformis* | *Hedbergella delrioensis* | *Hedbergella holmdelensis* | *Helvetoglobotruncana helvetica* | *Heterohelix globulosa* | *Heterohelix punctulata* | *Marginotruncana pseudolinneiana* | *Marginotruncana renzi* | *Marginotruncana sinuosa* | *Pseudotextularia nuttalli* | *Sigalia deflaensis* | *Whiteinella aprica* | *Whiteinella archaeocretacea* | *Whiteinella baltica* | Zone | Age |
|---|---|---|---|---|---|---|---|---|---|---|---|---|---|---|---|---|---|---|---|---|---|---|---|---|---|
| 324-U1348A- | | | | | | | | | | | | | | | | | | | | | | | | | |
| 2R-1, 9–10 | 84.30 | >150 | G | F | | | R | R | | F | | R | | F | | | | | | | | | | (*G. elevata*) | Campanian |
| 2R-CC, 12–15 | 85.41 | >150 | G | A | A | T | | | T | | | | | A | | A | F | A | T | C | | | | *D. asymetrica* | Santonian |
| 3R-1, 3–4 | 93.84 | >150 | M | | | | | | | | | | | F | | F | F | C | | | T | T | | (*M. sigali*) | Turonian |
| 4R-1, 0–1 | 103.41 | >150 | G | | | | | | | | A | | R | A | T | | | | | | A | F | R | *H. helvetica* | Turonian |

| Core, section, interval (cm) | Depth (mbsf) | Size fraction (µm) | Preservation | *Globigerinelloides aptiensis* | *Globigerinelloides maridalensis* | *Globigerinelloides paragottisi* | *Hedbergella delrioensis* | *Hedbergella implicata* | *Hedbergella rischi* | *Hedbergella wondersi* | *Praehedbergella aptiana* | *Praehedbergella gorbachikae* | *Praehedbergella roblesae* | *Pseudoschackoina saundersi* | *Ticinella madecassiana* | *Ticinella primula* | *Ticinella raynaudi* | *Ticinella roberti* | Zone | Age |
|---|---|---|---|---|---|---|---|---|---|---|---|---|---|---|---|---|---|---|---|---|
| 324-U1348A- | | | | | | | | | | | | | | | | | | | | |
| 5R-1, 0–1 | 113.01 | >150 | G | | | | T | | | R | | | | | | T | | | (*R. ticinensis*) | late Albian |
| 6R-1, 0–1 | 122.61 | >150 | G | | | | | C | | | | | | | C | A | T | C | *T. primula* (late) | middle Albian |
| 7R-1-, 6–7 | 132.27 | >150 | M | | | | | | A | | | | | | | F | | | *T. primula* (early) | middle Albian |
| 8R-1, 7–9 | 141.98 | >125 | P | | | | | | | | | | | | | | | | NA | NA |
| 9R-1, 19–20 | 151.70 | >125 | P | | | | | | | | | | | | | | | | NA | NA |
| 10R-1, 1–2 | 161.12 | >125 | G | | | | | | | | A | R | | | | | | | (*L. cabri*) | early Aptian |
| 10R-1, 20–21 | 161.31 | >125 | G | C | T | C | | | | | | | F | R | | | | | (*L. cabri*) | early Aptian |

Notes: Preservation: G = good, M = moderate, P = poor. Abundance: A = abundant, C = common, F = few, R = rare, T = trace. See "Paleontology" in the "Methods" chapter for preservation and abundance descriptions. Parentheses indicate zone is indirectly defined by secondary marker or assemblage (see text). NA = not available.

**Table T4.** Benthic foraminifer preservation and abundance for Unit I, Site U1348. (See table notes.)

| Core, section, interval (cm) | Depth (mbsf) | Size fraction (µm) | Preservation | Agglutinated | | | | Calcareous | | | | | | | | | | | | | | | |
|---|---|---|---|---|---|---|---|---|---|---|---|---|---|---|---|---|---|---|---|---|---|---|---|
| | | | | *Ammosphaeroidina* | *Dorothia* | *Gaudryina* | *Marssonella* | *Aragonia* | *Conorotalites* | *Gavelinella* | *Globorotalites* | *Globurina* | *Gyroidinoides* | *Laevidenalina* | *Lenticulina* | *Nodosaria* | *Oolina* | *Osangularia* | *Pleurostomella* | *Ramulina* | *Remesella* | *Reussoolina* | *Saracenaria* | *Sliteria* |
| 324-U1348A- | | | | | | | | | | | | | | | | | | | | | | | |
| 2R-1, 9–10 | 84.30 | >150 | G | | | | | C | | | | | | | | | | T | | | | | | R |
| 2R-CC, 12–15 | 85.41 | >150 | G | | | T | | | | | | T | T | | | T | | | | T | | | | T |
| 3R-1, 0–1 | 93.84 | >150 | M | | | | | | | | | | T | | | | | | | | | | | |
| 4R-1, 0–1 | 103.41 | >150 | G | | | | | | | | T | | T | | | | | | T | | | | | |
| 5R-1, 0–1 | 113.01 | >150 | G | | | | | | | T | | | T | | | | | T | | | | | | |
| 6R-1, 0–1 | 122.61 | >150 | G | | | F | | | | | | | C | | | | | C | | | T | | | |
| 7R-1-, 6–7 | 132.27 | >150 | M | | | | | | | | | | T | | | | | | | | | | | |
| 8R-1, 7–9 | 141.98 | >125 | P | | | | | | | T | | | | | | | | T | | | | | | |
| 9R-1, 19–20 | 151.70 | >125 | P | T | T | F | | | | T | | | R | | R | | T | C | T | T | | | | |
| 10R-1, 1–2 | 161.12 | >125 | G | | C | C | | | T | C | | | R | | | | | A | | | | | T | |
| 10R-1, 20–21 | 161.31 | >125 | G | | | A | T | | | A | | | A | C | R | | | | | R | | T | T | |

Notes: Preservation: G = good, M = moderate, P = poor. Abundance: A = abundant, C = common, F = few, R = rare, T = trace. See "Paleontology" in the "Methods" chapter for preservation and abundance descriptions.

**Table T5.** Secondary mineralogy of volcaniclastic rocks from XRD analyses, Hole U1348A. (See table note.)

| Core, section, interval (cm) | Depth (mbsf) | | Calcite | Phillipsite | Palygorskite | Celadonite | Montmorillonite | Nontronite | Sepiolite | Harmotome | Merlinoite | Fraipontite | Bentonite |
|---|---|---|---|---|---|---|---|---|---|---|---|---|---|
| | Top | Bottom | | | | | | | | | | | |
| 324-U1348A- | | | | | | | | | | | | | |
| 12R-1, 17–18 | 180.47 | 180.48 | | 1 | 1 | | | | | 1 | 1 | | |
| 12R-CC, 6–8 | 180.77 | 180.79 | | | | 1 | | | | | | | |
| 14R-1, 18–20 | 199.68 | 199.70 | 1 | | | | 1 | | | | | 1 | 1 |
| 14R-3, 53–55 | 203.04 | 203.06 | 1 | | | | 1 | 1 | 1 | | | 1 | 1 |
| 15R-1, 40–42 | 209.50 | 209.52 | 1 | 1 | | | | | | | | | |
| 15R-1, 95–96 | 210.05 | 210.06 | | 1 | | | 1 | 1 | | | | | |
| 16R-4, 138–140 | 224.42 | 224.44 | 1 | 1 | | | | 1 | | | 1 | | |
| 17R-2, 117–119 | 230.74 | 230.76 | 1 | 1 | | | 1 | | 1 | | 1 | | |
| 17R-5, 74–76 | 234.02 | 234.04 | 1 | 1 | | | 1 | | | 1 | 1 | | |
| 18R-3, 49–51 | 240.76 | 240.78 | 1 | 1 | | | | 1 | | | 1 | | |
| 19R-1, 113–117 | 248.63 | 248.67 | | | | | | | | | | | |
| 20R-2, 36–39 | 258.79 | 258.82 | 1 | 1 | 1 | | 1 | 1 | | | | | |
| 20R-4, 77–81 | 262.10 | 262.14 | 1 | | | | | 1 | 1 | 1 | | | 1 |
| 21R-1, 55–58 | 267.15 | 267.18 | 1 | 1 | 1 | | | | 1 | | | | |
| 21R-1, 103–105 | 267.63 | 267.65 | 1 | | | | 1 | 1 | | | | 1 | 1 |
| 21R-4, 13–16 | 271.22 | 271.25 | 1 | 1 | 1 | | | 1 | 1 | | | | |
| 22R-4, 86–88 | 281.29 | 281.31 | 1 | 1 | 1 | | 1 | | 1 | | | | 1 |
| 23R-3, 90–92 | 289.53 | 289.55 | 1 | | | | 1 | 1 | 1 | | | 1 | |

Note: 1 = mineral presence.

**Table T6.** Whole-rock major and trace element compositions, Hole U1348A. (See table notes.)

| | 324-U1348A- | | | | | | | | | | | | |
|---|---|---|---|---|---|---|---|---|---|---|---|---|---|
| Stratigraphic unit: | II | | III | | | | | | | | | V | VI |
| Core: | 12R* | 12R* | 14R‡ | 14R† | 15R‡ | 17R† | 17R† | 17R† | 17R† | 17R‡ | 18R‡ | 20R‡ | 26R‡ |
| Section: | 1 | CC | 1 | 3 | 1 | 1 | 1 | 3 | 3 | 5 | 3 | 4 | 2 |
| Piece: | 9 | 5 | 3 | 1 | 1 | 6 | 15 | 5 | 3 | 4 | 8 | 4A | 7 |
| Interval (cm): | 17–18 | 6–8 | 18–20 | 56–57 | 56–57 | 27–28 | 58–59 | 52–54 | 92–94 | 76–77 | 49–50 | 78–80 | 104–106 |
| Top depth (mbsf): | 180.47 | 180.77 | 199.68 | 203.07 | 209.66 | 228.57 | 228.88 | 231.46 | 231.86 | 234.04 | 240.76 | 262.11 | 317.06 |
| Major element oxide (wt%): | | | | | | | | | | | | | |
| $SiO_2$ | 62.79 | 58.15 | 34.32 | 49.41 | 48.89 | 53.05 | 53.30 | 50.24 | 46.60 | 47.93 | 38.36 | 48.96 | 49.10 |
| $TiO_2$ | 0.19 | 0.12 | 1.46 | 2.00 | 2.42 | 2.59 | 2.73 | 2.31 | 2.10 | 2.40 | 2.06 | 1.88 | 1.64 |
| $Al_2O_3$ | 19.43 | 14.01 | 11.81 | 16.70 | 14.09 | 17.64 | 18.98 | 17.50 | 15.08 | 13.86 | 12.80 | 14.47 | 14.81 |
| $Fe_2O_3^T$ | 6.32 | 16.29 | 6.41 | 8.56 | 15.80 | 7.17 | 7.04 | 3.45 | 6.17 | 15.43 | 8.60 | 12.71 | 12.76 |
| MnO | BD | 0.01 | 0.17 | 0.03 | 0.11 | 0.04 | 0.05 | 0.04 | 0.08 | 0.11 | 0.20 | 0.11 | 0.14 |
| MgO | 3.79 | 4.90 | 4.06 | 7.58 | 10.19 | 4.90 | 2.27 | 2.45 | 4.15 | 9.91 | 4.80 | 9.56 | 12.95 |
| CaO | BD | BD | 39.76 | 9.46 | 2.83 | 8.01 | 7.85 | 13.17 | 15.69 | 3.47 | 31.19 | 6.45 | 2.91 |
| $Na_2O$ | 4.01 | 2.72 | 2.00 | 3.23 | 3.43 | 3.25 | 3.59 | 3.58 | 3.68 | 3.51 | 3.08 | 3.79 | 3.20 |
| $K_2O$ | 3.34 | 2.78 | 1.98 | 1.15 | 2.02 | 3.45 | 4.18 | 4.52 | 3.70 | 2.25 | 3.03 | 2.63 | 1.07 |
| $P_2O_5$ | BD | BD | 0.05 | 3.09 | 0.13 | 1.99 | 1.53 | 5.64 | 6.18 | 0.08 | 0.08 | 0.36 | BD |
| Total: | 99.88 | 98.97 | 102.05 | 101.21 | 99.92 | 102.08 | 101.51 | 102.89 | 103.42 | 98.95 | 104.22 | 100.91 | 98.57 |
| LOI | 11.68 | 9.12 | 27.08 | 3.69 | 8.94 | 6.22 | 6.40 | 8.28 | 12.44 | 12.77 | 25.09 | 12.86 | 12.34 |
| Major element oxide (wt%) normalized to 100 wt%: | | | | | | | | | | | | | |
| $SiO_2$ | 62.87 | 58.75 | 33.63 | 48.82 | 48.93 | 51.97 | 52.51 | 48.83 | 45.06 | 48.44 | 36.81 | 48.52 | 49.81 |
| $TiO_2$ | 0.19 | 0.12 | 1.43 | 1.98 | 2.43 | 2.53 | 2.69 | 2.24 | 2.03 | 2.43 | 1.98 | 1.86 | 1.67 |
| $Al_2O_3$ | 19.45 | 14.16 | 11.58 | 16.50 | 14.10 | 17.28 | 18.70 | 17.00 | 14.58 | 14.00 | 12.29 | 14.33 | 15.02 |
| $Fe_2O_3^T$ | 6.33 | 16.46 | 6.28 | 8.45 | 15.81 | 7.02 | 6.94 | 3.35 | 5.96 | 15.59 | 8.25 | 12.59 | 12.94 |
| MnO | BD | 0.01 | 0.17 | 0.03 | 0.11 | 0.04 | 0.05 | 0.04 | 0.08 | 0.11 | 0.20 | 0.11 | 0.14 |
| MgO | 3.80 | 4.95 | 3.98 | 7.49 | 10.20 | 4.80 | 2.23 | 2.38 | 4.02 | 10.02 | 4.61 | 9.47 | 13.14 |
| CaO | BD | BD | 38.97 | 9.35 | 2.83 | 7.85 | 7.74 | 12.80 | 15.18 | 3.50 | 29.93 | 6.39 | 2.95 |
| $Na_2O$ | 4.02 | 2.75 | 1.96 | 3.19 | 3.43 | 3.18 | 3.53 | 3.48 | 3.55 | 3.55 | 2.96 | 3.75 | 3.25 |
| $K_2O$ | 3.34 | 2.81 | 1.94 | 1.13 | 2.02 | 3.38 | 4.12 | 4.40 | 3.57 | 2.27 | 2.91 | 2.61 | 1.08 |
| $P_2O_5$ | BD | BD | 0.05 | 3.06 | 0.13 | 1.95 | 1.51 | 5.48 | 5.98 | 0.08 | 0.08 | 0.36 | BD |
| Total: | 100.00 | 100.00 | 100.00 | 100.00 | 100.00 | 100.00 | 100.00 | 100.00 | 100.00 | 100.00 | 100.00 | 100.00 | 100.00 |
| Mg# | 58.3 | 41.2 | 59.6 | 67.3 | 60.0 | 61.4 | 42.8 | 62.3 | 61.0 | 59.9 | 56.5 | 63.6 | 70.3 |
| Trace element (ppm): | | | | | | | | | | | | | |
| Ba | 35 | 13 | 31 | 30 | 83 | 35 | 51 | 67 | 108 | 104 | 98 | 94 | 64 |
| Sr | 65 | 53 | 97 | 262 | 70 | 238 | 250 | 378 | 394 | 63 | 101 | 92 | 63 |
| Zr | 210 | 281 | 93 | 101 | 155 | 162 | 147 | 150 | 130 | 154 | 129 | 189 | 105 |
| Y | 24 | 17 | 25 | 96 | 26 | 87 | 67 | 233 | 186 | 23 | 26 | 39 | 20 |
| V | 26 | 14 | 202 | 264 | 342 | 324 | 415 | 207 | 261 | 332 | 316 | 249 | 281 |
| Sc | 5 | 4 | 27 | 32 | 35 | 24 | 20 | 20 | 22 | 33 | 31 | 30 | 35 |
| Cu | 9 | BD | 94 | 121 | 74 | 118 | 132 | 112 | 99 | 69 | 84 | 79 | 110 |
| Zn | 95 | 224 | 74 | 291 | 119 | 80 | 184 | 10 | 108 | 123 | 99 | 102 | 119 |
| Co | 10 | 11 | 35 | 135 | 62 | 43 | 47 | 30 | 35 | 54 | 48 | 53 | 49 |
| Cr | 6 | 103 | 148 | 219 | 284 | 212 | 231 | 199 | 158 | 252 | 163 | 151 | 244 |
| Ni | 50 | 62 | 109 | 310 | 151 | 99 | 101 | 74 | 97 | 136 | 131 | 113 | 128 |

Notes: * = clay-rich layers, † = handpicked chips of clasts separated from the bulk rock, ‡ = bulk volcaniclastic material. All analyses were conducted on samples ignited to 975°C. $Fe_2O_3^T$ = total iron expressed as $Fe_2O_3$. LOI = weight loss on ignition. Mg# = 100 × ($Mg^{2+}$/[$Mg^{2+}$ + $Fe^{2+}$]), assuming that $Fe_2O_3$/FeO = 0.15. BD = below detection.

**Table T7.** Moisture and density measurements, Site U1348. (See table note.)

| Core, section, interval (cm) | Top depth (mbsf) | Density (g/cm$^3$) | | | Void ratio | Water content (%) | Porosity (%) |
|---|---|---|---|---|---|---|---|
| | | Bulk | Dry | Grain | | | |
| 324-U1348A- | | | | | | | |
| 14R-3, 89–91 | 203.40 | 2.249 | 1.967 | 2.717 | 0.382 | 12.573 | 27.619 |
| 15R-7, 3–5 | 216.30 | 2.129 | 1.817 | 2.611 | 0.437 | 14.627 | 30.407 |
| 16R-2, 20–22 | 220.32 | 1.940 | 1.517 | 2.584 | 0.703 | 21.788 | 41.277 |
| 16R-4, 139–141 | 224.43 | 1.930 | 1.494 | 2.603 | 0.742 | 22.596 | 42.594 |
| 17R-2, 117–119 | 230.74 | 1.924 | 1.477 | 2.620 | 0.774 | 23.228 | 43.636 |
| 17R-7, 3–5 | 235.78 | 2.003 | 1.626 | 2.573 | 0.583 | 18.823 | 36.813 |
| 17R-8, 46–48 | 237.22 | 2.009 | 1.630 | 2.588 | 0.587 | 18.854 | 36.992 |
| 20R-1, 46–48 | 257.46 | 2.264 | 1.993 | 2.712 | 0.361 | 11.985 | 26.502 |
| 22R-3, 9–11 | 279.20 | 2.057 | 1.721 | 2.563 | 0.490 | 16.358 | 32.864 |
| 23R-3, 56–58 | 289.19 | 2.088 | 1.706 | 2.721 | 0.595 | 18.290 | 37.296 |
| 24R-2, 143–145 | 298.30 | 1.877 | 1.364 | 2.732 | 1.003 | 27.315 | 50.070 |
| 24R-4, 10–12 | 299.90 | 1.846 | 1.317 | 2.723 | 1.068 | 28.651 | 51.643 |
| 26R-3, 85–87 | 318.32 | 1.829 | 1.274 | 2.784 | 1.186 | 30.373 | 54.253 |

Note: Water content is relative to wet mass.

**Table T8.** Compressional wave velocity measurements, Site U1348. (See table note.)

| Core, section, interval (cm) | Top depth (mbsf) | Velocity (km/s) | | |
|---|---|---|---|---|
| | | *x*-direction | *y*-direction | *z*-direction |
| 324-U1348A- | | | | |
| 14R-3, 89–91 | 203.40 | 3.495 | 3.490 | 3.315 |
| 15R-7, 3–5 | 216.30 | 3.097 | 3.026 | 3.045 |
| 16R-2, 20–22 | 220.32 | 2.740 | 2.739 | 2.699 |
| 16R-4, 139–141 | 224.43 | 2.659 | 2.626 | 2.647 |
| 17R-2, 117–119 | 230.74 | 2.537 | 2.569 | 2.542 |
| 17R-7, 3–5 | 235.79 | 2.999 | 3.010 | 3.000 |
| 17R-8, 46–48 | 237.22 | 2.950 | 3.014 | 2.894 |
| 20R-1, 46–48 | 257.46 | 3.449 | 3.365 | 3.297 |
| 22R-3, 9–11 | 279.20 | 3.277 | 3.291 | 3.250 |
| 23R-3, 56–58 | 289.19 | 2.602 | 2.678 | 2.638 |
| 24R-2, 143–145 | 298.29 | 2.412 | 2.407 | 2.375 |
| 24R-4, 10–12 | 299.89 | 2.295 | 2.296 | 2.297 |
| 26R-3, 85–87 | 318.30 | 2.135 | 2.119 | 2.090 |

Note: Values are accurate to ±20 m/s.

**Table T9.** Demagnetization results, Site U1348. (See table notes.)

| Core, section, interval (cm) | Depth (mbsf) | | Fit (mT) | *N* | Inclination (°) | Declination (°) | MAD (°) | NRM$\chi$ (SI) | MDF (mT) |
|---|---|---|---|---|---|---|---|---|---|
| | Top | Bottom | | | | | | | |
| 324-U1348A- | | | | | | | | | |
| 14R-3, 89–91 | 203.40 | 203.42 | 15–80 | 8 | 7.30 | –140.00 | 6.1 | 3.29E–02 | 22.3 |
| 15R-7, 3–5 | 216.30 | 216.32 | 25–80 | 6 | 23.30 | 33.40 | 12.2 | 6.26E–04 | 9.2 |
| 16R-2, 20–22 | 220.32 | 220.34 | 10–30 | 6 | 12.90 | –102.90 | 2.9 | 5.94E–04 | 18.2 |
| 16R-4, 139–141 | 224.43 | 224.45 | 12–30 | 5 | 19.90 | –128.70 | 3.1 | 6.00E–04 | 13.4 |
| 17R-2, 117–119 | 230.74 | 230.76 | 10–80 | 10 | –9.10 | –59.40 | 4.1 | 5.10E–04 | 25.0 |
| 17R-7, 3–5 | 235.78 | 235.80 | 15–80 | 8 | 21.30 | 120.90 | 2.7 | 4.83E–04 | 17.5 |
| 17R-8, 46–48 | 237.22 | 237.24 | 10–80 | 9 | 3.50 | 94.40 | 10.9 | 5.96E–04 | 18.8 |
| 22R-3, 9–11 | 279.20 | 279.22 | 15–80 | 8 | 9.70 | 88.20 | 8.9 | 2.12E–03 | 17.5 |

Notes: For all samples, principal component analysis (PCA) is anchored to origin. *N* = number of points used for PCA, MAD = maximum angular deviation (Kirshvink, 1980), NRM$\chi$ = bulk susceptibility of natural remanent magnetization (NRM), MDF = median destructive field.

**Table T10.** Logging operations, Hole U1348A. (See table notes.)

| Tool string | Direction | Interval logged WMSF (m) Top | Interval logged WMSF (m) Bottom | Pipe depth DRF (m) | Depth shift (m) | Logging speed (m/h) |
|---|---|---|---|---|---|---|
| HNGS-HLDS-GPIT-DITE | Downlog | 0 | 320 | 3368.5 | –3267 | 550 |
| | Uplog | | | | | |
| | Pass 1 | 100 | 314 | 3368.5 | –3267 | 275 |
| | Pass 2 | 0 | 320 | 3368.5 | –3267 | 550 |
| HNGS-DSI-FMS | Downlog | 0 | 320 | 3368.5 | –3267 | 550 |
| | Uplog | | | | | |
| | Pass 1 | 115.5 | 328 | 3368.5 | –3267 | 550 |
| | Pass 2 | NA | NA | NA | NA | NA |

Notes: Seafloor depth = 3275 m DRF, 3267 m WRF. HNGS = Hostile Environment Natural Gamma Ray Sonde, HLDS = Hostile Environment Litho-Density Sonde, GPIT = General Purpose Inclinometry Tool, DITE = Dual Induction Tool model E, DSI = Dipole Sonic Imager, FMS = Formation MicroScanner. NA = not available.